INVESTIGATION OF THIN FILM MATERIALS FOR NEXT GENERATION LITHIUM ION BATTERIES

A Dissertation

by

CLEMENT JACOB

Submitted to the Office of Graduate and Professional Studies of
Texas A&M University
in partial fulfillment of the requirements for the degree of

DOCTOR OF PHILOSOPHY

Chair of Committee,	Haiyan Wang
Committee Members,	Arum Han
	Rusty Harris
	Xinghang Zhang
Head of Department,	Miroslav M. Begovic

May 2016

Major Subject: Electrical Engineering

ABSTRACT

Lithium ion battery is the dominant secondary storage technology for portable electronics, electric vehicles, medical devices and grid storage. While it has gained widespread acceptance, current generation battery materials are limited by the expensive and often toxic components, and safety concerns, and, still cannot meet projected storage requirements for future applications. A majority of studies rely on traditional synthesis techniques similar to those used for large scale manufacturing for development and investigation of new materials. Our work takes an alternate approach of harnessing thin film technology that has been extensively developed for semiconductor-related research. The thesis focuses on the investigation of the next generation environmentally friendly and low cost battery material using thin film- based studies. A better understanding and optimization using thin film techniques aids the development of traditional processes for bulk batteries and also paves a way for future all thin film-based battery for portable electronics. The work focuses on Mn-based materials because of its low cost and non-toxic nature.

A unique one step deposition processes have been developed and demonstrated using the growth and analysis of epitaxial and highly textured $Li(Ni_xMn_yCo_{1-x-y})O_2$ (NMC) thin film on stainless steel with a thin gold buffer layer. The NMC thin film cathodes gave a high capacity of 167 $mAh.g^{-1}$ and 125 $mAh.g^{-1}$ at 0.1 C and 0.5 C respectively. Another promising next generation material Li_2MnO_3 has also been investigated. An unique process to extract Li_2O during synthesis has been developed to activate this material directly during deposition. Li_2MnO_3 cathodes with capacity of 225 $mAh.g^{-1}$ were synthesized by tuning growth

conditions appropriately. Another Mn based chemistry, commonly referred to as Li-rich oxide, has been investigated. Nano-domain and composite model structures have been developed to investigate unresolved questions about the microstructure of the films. It has been demonstrated that a nano-domain model best matches with the characteristic electrochemical properties of Li-rich cathodes with a demonstrated capacity of 293 mAh g^{-1} at 0.05 C. Further study has been carried out to explore optimum composition and structure for Li-rich based thin film cathodes.Composition variation experiments indicate that the 50:50 deposition schemes gave the highest capacity. Moreover, the results indicate a strong correlation between Li_2MnO_3 domain size on the capacity of the Li rich electrode. A study to investigate correlation between oxygen stoichiometry and microstructure on behavior of Li_2MnO_3 showed strong inter-correlation. It shows that Li rich cathodes performed the best when deposited at low oxygen partial pressure while Li_2MnO_3 required a moderate partial pressure for optimum capacity.

Finally Li_3PO_4 and LiPON electrolytes have been investigated for all solid state battery development. An electrolyte coating on top of a NMC cathode film resulted in significant improvement to the observed capacity. Li_3PO_4 coated cathodes demonstrated a high capacity of ~ 80 µAh/µm.cm^2 at 0.75 µA.cm^{-2}, compared to 65 µAh/µm.cm^2 that was observed in bare NMC. This work contributes to the implementation of all solid state batteries using thin film approaches with great potentials for various applications such as integrated circuits, portable medical devices and space applications.

DEDICATION

This work is dedicated to my mom's sacrifices, dad's patience and hard work, and brother's inspiration; invaluable lessons, love and support without which I wouldn't be here today.

ACKNOWLEDGEMENTS

I would like to thank my research advisor Dr.Haiyan Wang for all her insights, discussion and guidance through the course of my doctoral research. I am especially grateful for the independence, trust and latitude she gave me to explore new ideas. Dr.Wang's systematic approach, attention to detail and drive for results has lent strongly to both my professional and personal development.

I would also like to thank my committee members, Dr. Arum Han, Dr. Rusty Harris and Dr. Xinghang Zhang for their time, advice and suggestions. I would also like to thank the faculty at Texas A&M University whose courses have been extremely informative. I am grateful to Dr. Xinghang Zhang and Dr. Haiyan Wang for introducing me to many of the fundamentals of Materials Science which has been extremely helpful through my research. I would also like to thank to Dr. Xing Cheng and Dr.Andreas Holzenburg for the many interesting discussions in their classes.

I would also like to acknowledge my current and former colleagues. I would like to thank Tommy Lynch, Travis Neely, Alyaman Amer and Mitchell Underwood for their help with various projects through the years. I would also like to thank Dr. Michelle Myers,Jie Jian and Han Wang for their help with TEM imaging. I am also grateful for all the help and suggestions of my current and former colleagues, Dr.Sungmee Cho, Dr. Joon-Hwan Lee, Dr. Chen-Fong Tsai, Dr. Yuanyuan Zhu, Dr. Aiping Chen, Dr. Qing Su, Dr. Fauzia Khatkhatay, Dr.Liang Jiao, Wenrui Zhang, Leigang Li, Meng Fan and Jijie Huang. A special thanks to the Aggie Fab staff, Robert, Dennie and Jim for fixing broken equipments and setting up new ones

without which this research would not have been possible. Last but not the least, a big thanks to the electrical engineering staff especially, Tammy, Jeannie, Melissa, Anni and Henry.

Finally, thanks to my parents and brother for their constant encouragement, patience and love all these years. Without their support, I would have not ventured into this time consuming but rewarding venture.

NOMENCLATURE

PLD	Pulsed Laser Deposition
PVD	Physical Vapor Deposition
TEM	Transmission Electron Microscopy
XRD	X-ray Diffraction
FWHM	Full Width at Half Maximum
SAED	Selected Area Electron Diffraction
FFT	Fast Fourier Transformation
SEM	Scanning Electron Microscopy
STEM	Scanning Transmission Electron Microscopy
HAADF	High Angle Annular Dark Field Imaging
WDS	Wavelength Dispersive Spectroscopy
SIMS	Secondary Ion Mass Spectroscopy

TABLE OF CONTENTS

Page

LIST OF FIGURES

Page

LIST OF TABLES

Page

CHAPTER I

INTRODUCTION AND LITERATURE REVIEW

Lithium ion batteries are by far the most popular energy storage technology employed in portable electronics such as laptops, cell phones, power tools, etc., today. While the Li ion battery is significantly superior to other battery technologies it also suffers drawbacks like cost, safety and technology stagnation[1, 2]. The mainstream research work as well as all commercial development in Li ion batteries focuses on thick film batteries[3-6]. The work concentrates on material development via solid state [7-9]or solution based synthesis [10-13] technique or process development for battery assembly. Yet another section of researchers concentrate on battery modeling towards material and related process development [14-16]. A small group of researchers work on thin film batteries [17-20], but from commercial point of view, cost, film volume and electrolyte limitations has restricted work in this field [21, 22]. In this work we concentrate on intersection of modeling and thin film work to address shortcomings of the mainstream thick film research. Specifically, we propose the use of thin film batteries to study properties of promising materials by designing electrodes with predetermined chemical composition and microstructure. In addition, we report deposition schemes that harness various thin film techniques like defects, nano-domain and multilayers to optimize the material for all solid state batteries. We specifically focus on Mn based materials to minimize cost and environmental impact.

1.1 Fundamentals of Electrochemistry

Italian physicist Galvani attached zinc and copper rods to a dead frog and found that whenever the rods were connected externally, the frog twitched[23]. Galvani initially attributed the electricity to the frog, however, another physicist, Volta, inspired by this experiment developed the 'Voltaic Pile'. It consisted of alternate copper and zinc discs separated by brine soaked cloth. The native potential difference between the two metals allows it to store electricity[24]. The voltaic pile is an example of a primary battery, i.e. a non-rechargeable battery.

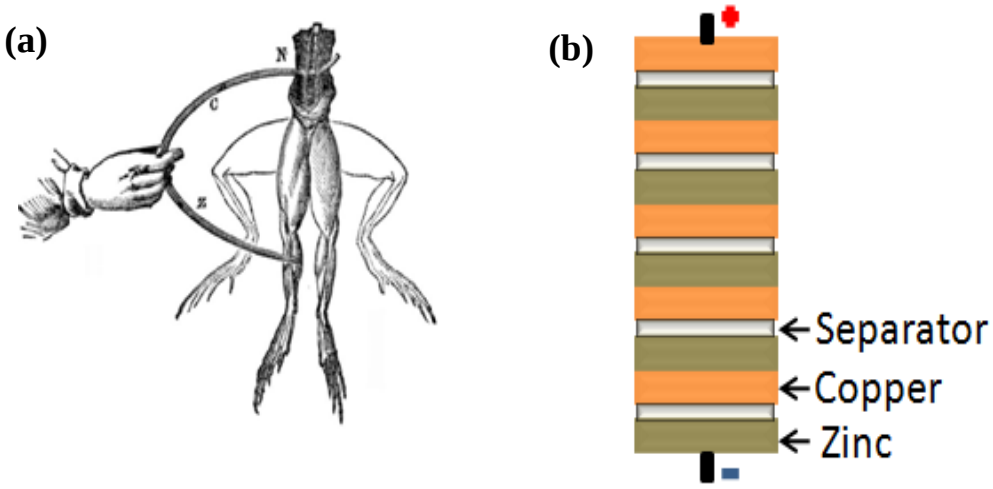

Figure1.1. (a) Illustration of Galvani's "animal current" experiment, (b) Volta's voltaic pile.

The electrodes in a battery undergo spontaneous reaction under appropriate conditions that leads to transfer of ions. Hence they are also called electrochemical or galvanic cells. Galvanic reactions are thermodynamically favorable and will occur

spontaneously when the reactants are brought together. The material with lower standard reduction potential undergoes an oxidation reaction, providing electrons. These electrons are transferred via an external path to neutralize the second material that undergoes reduction reaction. The electrode that provides the electron is called the negative electrode or anode. The electrode that accepts the electron is called the positive electrode or cathode. In case of rechargeable batteries this reaction is reversible, but the same "discharge convention" is used. The potential energy that drives the ion transfer is utilized to do external work using the flow of electrons in the external path. This potential energy is essentially the difference in the Gibbs free energy or in terms of voltage it is the difference between the equilibrium potentials of the two electrodes. Thus,

$$E_{cell} = E_c^e - E_a^e$$

Where, E_c^e and E_a^e are equilibrium potentials or the standard potentials of the cathode and anode respectively. Traditionally, the reduction potential of a material measured in its standard state (unit activity) with respect to a standard electrode (often a standard hydrogen electrode).Now, at equilibrium no significant net charge transfer and electron flow will occur. Hence to drive the reaction a higher potential or over potential needs to be applied[25]. Also voltage drops across the electrolyte and separator or membrane also need to be accounted for. Thus in practice to drive the electrochemical reaction the voltage required E_{cell} is given as,

$$E_{cell} = E_{cell}^e - |\eta_c| - |\eta_a| - |IR_{sol}| - |IR_{mem}|$$

Where, η_c and η_a are cathodic and anodic over potentials and R_{sol} and R_{mem} represent the electrolyte and separator resistance. The equilibrium cell potential E^e_{cell} can be directly measured between the cathode and the anode using a voltmeter as shown by the E_{cell} equation above or calculated from the Nerst equation,

$$E^e_{cell} = E^o_e + \frac{2.3RT}{nF} log \frac{c_o}{c_R}$$

Where, E^o_e is the formal potential for the redox reaction, R is the gas constant, T is the reaction temperature, n is the number of electron, F is the Faraday constant[26]. Note that at equilibrium, when no electron is flowing, the concentration of reductant and oxidant is equal and hence the cell potential is equal to the formal potential. Now having determined the origin of the potential difference, the next obvious question is how this converts to electron flow or electricity. Two critical factors that can potentially limit this reaction are the rate constant of the reaction k, and the concentration of the reactant, c. Hence the rate of these reactions can be obtained simply by taking the product of these two factors. Note that both k and c have different values at the cathode and the anode. Next, these ionic reactions can be converted to electron or current density; we can multiply this by nF. The rate k is given empirically as,

$$k = k^0 exp \frac{\alpha_a nFE}{RT}$$

Using these, we can compute the total current density as the sum of the anodic and cathodic current density. This gives us the Butler-Volmer equation for current density.

$$j = j_0(exp\frac{\alpha_a\, nF\eta}{RT} - \ exp - \frac{\alpha_c\, nF\eta}{RT})$$

Where, α_a and α_c are transfer coefficients and j_0 is the exchange current density[27].Having determined the basic mechanisms driving the electro-chemical potential and current in a battery, these need to be connected to practical problems[28].

1.1.2. Cell Resistance

The equation for cell potential discussed earlier had a solution resistance and membrane component. Amongst these, solution resistance is sensitive to concentration of ions, distance, temperature, current etc. For instance during cyclic voltammetry measurements, changing current will change the IR drop. Since the change in current is a complex, non-linear process, it can distort the measurements. At low currents, two electrode measurements are acceptable, however at higher currents a three electrode measurement setup is recommended.

1.1.3. Double Layer Capacitance

During battery operation the surface has a surface charge because of the applied potential. This attracts ions of the opposite charge which is separated by a thin insulating space, often in the order of Angstroms. This forms a double layer and even a conducting electrode will exhibit some capacitance[29]. Due to this a change in potential will lead to a charging current component. Thus now, the total current has an additional double layer

component. This is not a problem for steady state measurements, but for dynamic measurements like cyclic voltammetery, this can distort the response. This becomes a significant problem at higher sweep rates in such measurements. The double layer capacitance formation is illustrated in the figure 1.2 below.

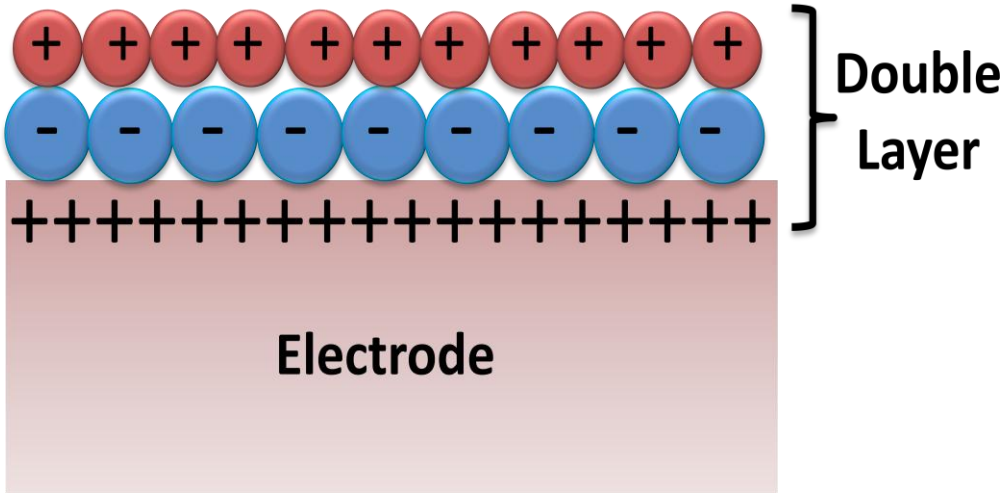

Figure 1.2. Illustration of a double layer capacitor formed at battery electrodes.

1.1.4. Polarization

Polarization occurs when the competing charge mechanisms in the system push the potential of the system away from the open circuit voltage[30]. This results when the two reactions are not in equilibrium. For instance, if one of the reactions is diffusion limited and the other is not a net potential build up occurs. This effectively causes a voltage drop (discharging) or over voltage (charging) can be modeled as a resistance, aptly called

polarization resistance. Polarization is often measured in terms of overpotential (η) and is given by difference between the equilibrium potential (E_e) and actual potential (E). Thus,

$$\eta = E - E_q$$

The overall observed polarization includes the ohmic polarization, activation polarization and concentration polarization as shown in figure 1.3.The ohmic polarization occurs due to electrolyte resistance and becomes a significant factor in solid state batteries. The activation polarization is dependent on the electrode material while concentration polarization is attributable to charge concentration gradient in the battery. All of these contribute to lowering of cell voltage from open circuit voltage at equilibrium to an effective operating voltage which reduces with increasing current.

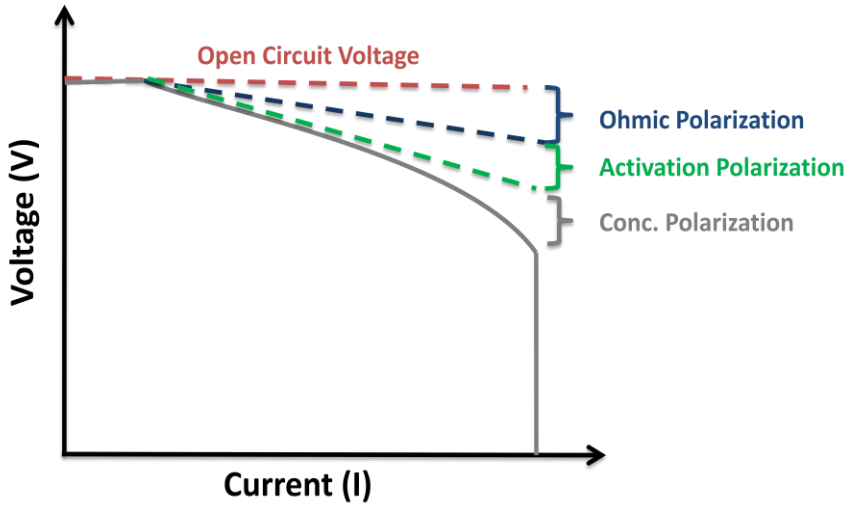

Figure1.3. Effect of polarization on the operating voltage of a battery.

1.1.5. Electrical Noise

Electrical noise can originate either from instrumentation or device. While bulk batteries are relatively immune to this due to improved instrumentation, thin film batteries might be susceptible to instrument noise due to the ultra low currents involved. High resistance components in a cell, poor contacts, air bubble in cell, unshielded wires can all cause noise. Proper precautions during assembly, good wiring, faradays cage etc. can be used to minimize such noise.

1.2 Primary and Secondary Batteries

Most commercial primary batteries in the market are either based on the Zn-C or Zn-MnO_2 chemistry (Figure 1.4) [31-33]. The Zn-C cells consist of a Zn casing that also serves as the anode. The cathode consists of MnO_2 mixed with Carbon for improving conductivity. This mixture is soaked in a Zinc chloride or Ammonium Chloride Electrolyte. A carbon rod inserted at the center of this mixture serves as the current collector. A paper based separator is used between the Zn anode case and the cathode. At the anode Zn is oxidized via the following half reaction.

$$Zn(s) \rightarrow Zn^{2+}(aq) + 2\ e^{-}\ [E° = -0.7626\ V]$$

At the cathode Mn is reduced from +4 to +3 according to the following half reaction.

$$2MnO_2(s) + 2\ e^{-} + 2NH_4Cl(aq) \rightarrow Mn_2O_3(s) + 2NH_3(aq) + H_2O(l) + 2\ Cl^{-}\ [E° \approx +0.5\ V]$$

The Cl ions then react with the Zn ions formed at the anode. The overall reaction is given as

$$Zn(s) + 2MnO_2(s) + 2NH_4Cl(aq) \rightarrow Mn_2O_3(s) + Zn(NH_3)_2Cl_2\ (aq) + H_2O(l)$$

These cells give a capacity of around 40 mAh/g.

The alkaline battery uses the same cathode and anode material but uses an alkaline electrolyte, potassium hydroxide rather than an acidic electrolyte[34]. The higher conductivity of the electrolyte means lower internal resistance. Also instead of using a zinc can as anode a mixture of Zn/Hg mixed with the electrolyte with a brass (Cu/Zn) current collector inserted at the center. The Electrolytic Manganese Oxide (EMD) forms the cathode surrounding the anode core. Thus the Alkaline battery is effectively inside out compared to the Zn-C battery. The electrochemical reactions governing energy storage are as follows,

$$Zn_{(s)} + 2OH^-_{(aq)} \rightarrow ZnO_{(s)} + H_2O_{(l)} + 2e^- \; [e° = 1.28 \text{ V}]$$

$$2MnO_{2(s)} + H_2O_{(l)} + 2e^- \rightarrow Mn_2O_{3(s)} + 2OH^-_{(aq)} \; [e° = +0.15 \text{ V}]$$

Overall reaction:

$$Zn_{(s)} + 2MnO_{2(s)} \rightleftharpoons ZnO_{(s)} + Mn_2O_{3(s)} \; [e° = 1.43 \text{ V}]$$

Due to higher conductivity of alkaline electrolyte, use of Zn/Hg powder instead of Zn Can as anode which gives more surface area and use of EMD [35]with higher capacity than natural MnO_2, the alkaline cells give around 25% higher capacity than Zn-C battery, around 65 mAh/g.

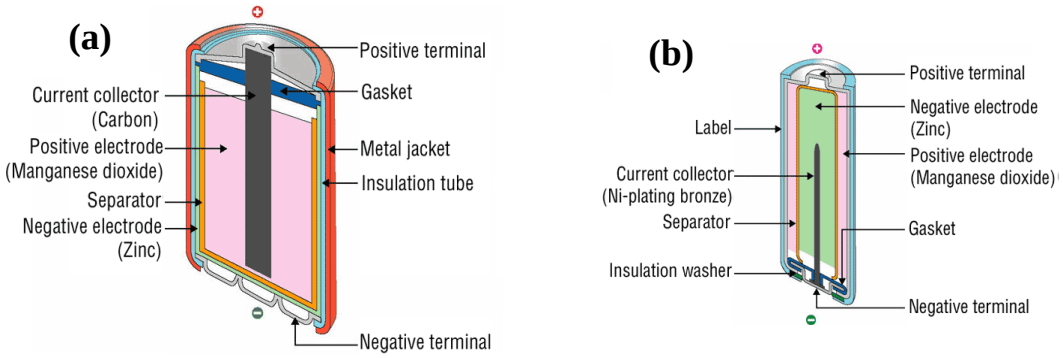

Figure1.4. (a) Commercial Zn-C battery and, (b) alkaline battery schematic [36].

Li is a logical and popular choice for a battery anode as it is the lightest metal (0.54 g/cm^3) and highest standard potential (3.05 V).Several popular Li based primary cell have been commercialized including those based on MnO_2, FeS_2, V_2O_5, SO_2, $SOCl_2$ (thionyl chloride) [37]. It is not at al l surprising that many of these seem similar to many of today's secondary Li ion battery materials. In fact early work in Mn based oxides lead to clues for development of Mn based Li-rich cathodes, a potential next generation cathode. MnO_2 is popular primary battery chemistry commercially[38]. These cell use Li anode, heat treated MnO_2 cathode and propylene carbonate/1,2-dimethoxyethane electrolyte with Li salt.Due to intercalation of Li,Mn transforms from trivalent to tetravalent state forming Li_xMnO_2. The cell gives a typical capacity of 75mAh/g at a nominal 3.3 V. The electrochemical reaction governing it is given below.

$xLi + MnO_2 \rightarrow Li_xMnO_2$

Partly thanks to its potential being closer to conventional primary batteries at 1.5 V Li/FeS_2 is gaining prominence. The redox reaction for this can be given as

$4Li + FeS_2 \rightarrow Fe + Li_2S$

The Li/FeS_2 chemistry gives a nominal capacity of 175mAh/g with a flatter discharge curve than alkaline batteries especially at higher discharge rate. A typical Li primary coin cell is shown in figure 1.5.

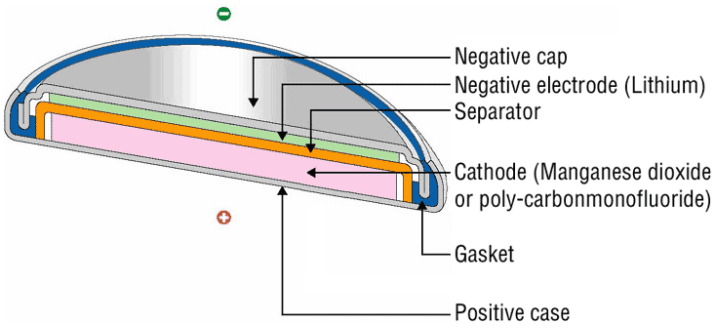

Figure1.5. Primary Li ion battery in coin cell format [36].

In general primary batteries are characterized by a non-reversible redox reaction, i.e. if an opposite charge is applied; the original electrodes are not reformed. Other competing reactions like hydrogen generation, electrolyte decomposition etc., are more favorable. In addition mechanical damage due to volume expansion of metal could lead to delamination, in turn, increasing cell impedance. Another limiting mechanism is dendrite formation, which could lead to a short between the electrodes. Batteries that can be recharged require a combination of appropriate reversible chemistry and cell design to overcome these

limitations. German physicist Johann Wilhelm Ritter first discovered in 1803 that a pile of layered copper discs and cardboard soaked in brine solution can store small secondary charges. This was able to only hold a transient charge and it took about half a century for the first true battery, the lead acid cell was developed.

1.2.1. Lead Acid Batteries

French physicist Raymond Plante invented the first commercial rechargeable cell, a lead acid battery in 1859. The cell consisted of two lead sheets separated by a coarse cloth or leather rolled spirally and immersed in 10% sulfuric acid. When the plates were charged for 24 hours, oxygen evolved at the positive electrode, forming PbO_2 while H_2 evolved the negative electrode leaves pure porous Pb. The PbO_2 and Porus Pb formation increased with subsequent cycling. The resultant cell had low resistance, high capacity and almost no polarization. Also the 'formed' PbO_2deposits back on the same electrode and are insoluble in the dilute acid. Modern lead acid batteries use electrodes made by applying a paste of Pb (anode) or PbO_2 (cathode), carbon and other additives on lead grids. The electrolyteis either used in the form of glass fiber mat soaked in acid (AGM) or silica gelling agent mixed with electrolyte[39]. The electrochemical equations governing these cells is given as,

Negative plate reaction:

$$Pb(s) + HSO_4^-(aq) \rightarrow PbSO_4(s) + H^+(aq) + 2e^-$$

Positive plate reaction:

$$PbO_2(s) + HSO_4^-(aq) + 3H^+(aq) + 2e^- \rightarrow PbSO_4(s) + 2H_2O(l)$$

The total reaction can be written as

$Pb(s) + PbO_2(s) + 2H_2SO_4(aq) \rightarrow 2PbSO_4(s) + 2H_2O(l)$

These batteries give a capacity of 170Wh/kg at a nominal voltage of 2.1 V. While the lead acid remains popular today, it has severe limitations like short life due to electrode corrosion due to high temperature (>21 °C), storage at discharged state, irreversible sulfation of anode plate which reduces conductivity, volume expansion (Pb to $PbSO_4$ transformation leads to 37% volume increase) causing grid damage[40-42]. Figure 1.6 shows a lead acid battery.

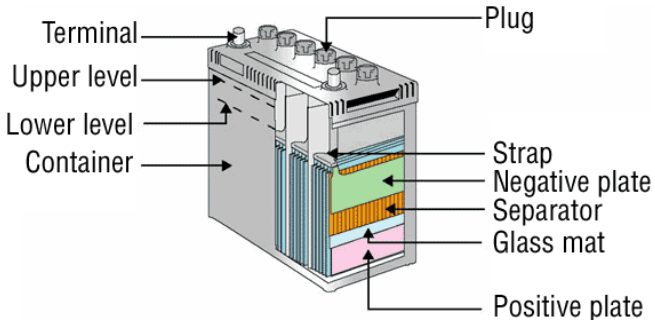

Figure1.6. Schematic of a lead acid battery[36].

1.2.2. Nickel-Cadmium Battery

Swedish inventor Ernst Waldemar Jungner invented the Ni-Cd battery in 1899. The cell uses a nickel hydroxide-graphite cathode and a cadmium hydroxide or cadium oxide mixed with iron or iron oxide with KOH electrolyte (Figure 1.7a). The reaction at the anode is

$Cd(s) + 2OH^-(aq) \rightarrow Cd(OH)_2(s) + 2e^-$

The reaction at the cathode is

$2NiO(OH)(s) + 2H_2O(1) + 2e^- \rightarrow 2Ni(OH)_2(s) + 2OH\text{-}(aq)$

The total reaction can be written as

$Cd(s) + 2NiO(OH)(s) + 2H_2O(1) \rightarrow Cd(OH)_2(s) + 2Ni(OH)_2(s)$

Ni-Cd has a specific capacity of 50 mAh/gat a nominal voltage of 1.2V. These batteries have longer shelf life at any state of charge and can be charged rapidly, however it suffers memory effect, which means that it has to be discharged completely before charging or it will suffer capacity loss. Also use of toxic Cadmium means that it is an environmental hazard[42, 43].

1.2.3 Nickel Metal Hydride Batteries

The metal hybrid battery is similar to the Ni/Cd battery but it uses hydrogen (absorbed on a metal alloy) instead of Cd (Figure 1.7b). This can be either an AB_5 class alloy like $LaNi_5$ or AB_2 class of alloy like$TiZr_2$, both are commonly partially substituted partially to improve corrosion resistance, hydrogen storage, increase cycle life etc. , Nickel oxyhydride as the positive electrode and aqueous KOH electrolyte. During the charge process water is dissociated by electrolytic reaction into H^+ and OH^- ions. H^+ ion is absorbed by the metal electrode and OH^-reacts with the $Ni(OH_2)$ electrode[43-46].

The negative electrode reaction occurring in the NiMH cell is:

$H_2O + M + e^- \rightleftharpoons OH^- + MH$

On the positive electrode, nickel oxyhydroxide, NiO(OH), is formed:

$Ni(OH)_2 + OH^- \rightleftharpoons NiO(OH) + H_2O + e^-$

The overall reaction is then given as,

$Ni(OH)_2 + M \rightleftharpoons NiO(OH) + MH$

A cylindrical cell is constructed by making a spiral roll of the positve and negative electrode seperated by an insulater soaked in KOH. The positive electrode uses a Ni foam impregnated with Ni compounds which is then converted to active material by electrodeposition. The negative electrode consists of a Ni grid on which hydrogen storage alloy is coated. The Ni-MH battery gives a capacity of 60-70 mAh/g at 1.2V, but it is not as robust as Ni-Cd, and has poor shelf life and cycling capability[42]. It also suffers memory effect like Ni-Cd cells. Just the same, this remained one of the most advanced secondary battery till the development of commercial Li ion batteries.

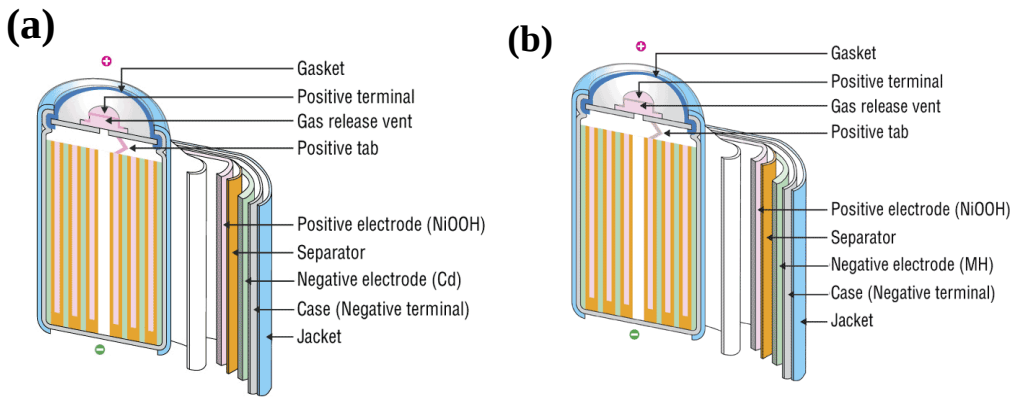

Figure1.7 .Schematic of (a) Ni-Cd, (b) Ni-MH cylindrical cell [36].

1.2.4 Lithium Ion Batteries

Li ion batteries were first commercialized in 1991 by Sony. These batteries had higher power than all previously know battery materials and had overcome significant challenges. The theory and engineering of Li ion batteries is covered in the following section.

1.3 Lithium Ion Batteries

As mentioned earlier Li is a natural choice for energy storage due to its low density and electrode potential (-3.01 V wrt Standard Hydrogen Electrode).M.S. Whittingham, then at Exxon developed Li ion batteries with $LiTiS_2$ cathode and metallic Li anode[1]. However, these batteries when overcharged burst into flames, due the reactive nature of Li. This problem was also limited $LiMoS_2$ (Moli Energy, Canada) and $Li_{0.3}MnO_2$ (Taridan,Israel) cathode based batteries developed around 1980's. Meantime, around 1970's, J. O. Besenhard at TU Munich demonstrated reversible intercalation in graphite and also intercalation in oxide based cathodes. In 1979, John Goodenough and Koichi Mizushima demonstrated reversible intercalation in $LiCoO_2$, at Oxford University. Eventually, in 1991 Sony released the first commercial Li ion battery with $LiCoO_2$ cathode and graphite anode[47].

The lithium ion battery uses Li ions that shuttle between the source cathode and sink anode to charge and discharge the battery. This is shown in figure 1.8 potential or open circuit voltage of the cell (Voc), with the Gibbs Energy given as

$\Delta G = -EF$

$eV_{oc} = \mu_A - \mu_C \leq E_g$

Where, μ_A and μ_C are the anode and cathode potentials or their Fermi energies. The electrolyte should be chosen such that it does not react with the electrolytes. To ensure this the anode's μ_A should be below the electrolytes LUMO (lowest unoccupied molecular

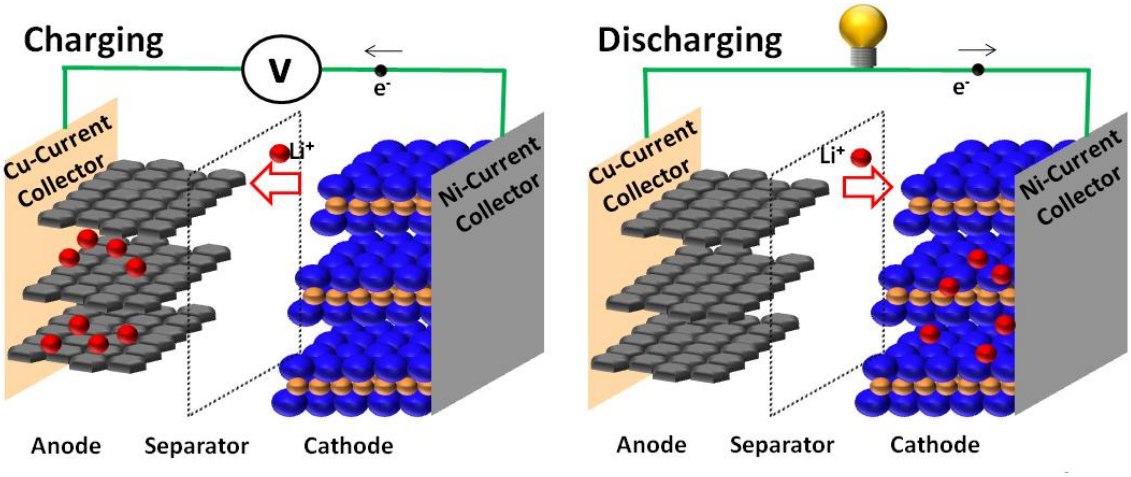

Figure1.8.Schematic showing charging and discharging process of a Li ion battery.

The potential difference between the Li ions in the anode and cathode, determines the cell orbital) and the cathodes μ_C, should be above the electrolytes HOMO (highest occupied molecular orbital(Figure 1.9) . Since aqueous electrolytes ($E_g \approx 1.3$ eV) restrict the potential, non aqueous electrolytes are used.

All solid state thin film batteries have been of interest since the early 50's as it offers several advantages over thick film batteries with liquid electrolyte. Solid state batteries use solid electrolytes instead of traditional liquid electrolytes. This makes the construction robust and it can with stand larger mechanical shock and acceleration. Since the solid electrolyte

also serves as separator and is conformal to the electrodes. This structure is more resistant to mechanical damage. This is useful for aerospace application. The absence of liquid electrolyte reduces the evaporation problem at high temperature and freezing problem at low temperature. This means that solid state battery have wider operating temperature range. This is again important for operation in hostile environments. Commercial lithium ion batteries rely on flammable organic electrolyte. This couple with exothermic reactions at the electrode leads to fire hazard. Another recurring problem with commercial batteries is dendrite formation on Li metal anodes. While pure Li metal counter electrode will obviously give the highest capacity, it suffers from asymmetric Li growth during cycling. This can potentially puncture the polymer separator causing a short. Solid state battery is inherently resistant to this due to suppression of SEI layer. Yet another important advantage comes from the inherent packaging ease. Only half the cost of a battery comes from associated materials. Housing, temperature monitoring and related battery control software, wiring etc. can cost up

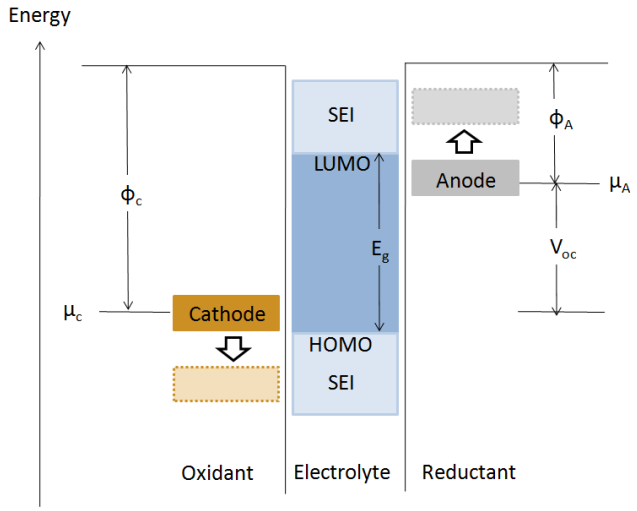

Figure 1.9. Energy band diagram of a lithium ion battery of a Li ion battery.

to 20% of the total cost[48]. Likewise, battery capacity is traditionally normalized with respect to weight (specific capacity in mAh/g) or volume (volumetric mAh/cm^3). Again the hermetically sealed packaging along with pressure safety caps adds to both weight and volume. Solid state battery simplifies packaging since there is no liquid electrolyte. Also, it is obvious that the higher density of solid electrolyte will allow for a higher overall volumetric density for the cell [17, 49, 50].

A solid state battery requires sequential deposition of thin film cathode, electrolyte and anode. This work concentrates predominantly on cathodes and reports some preliminary work on solid electrolytes. A variety of thin film techniques have been developed for the semiconductor films both in academic and industrial research labs. This work can be classified based on chemistry, deposition techniques, or architecture. Chemistry based classification would involve either the cation involved like Fe, Mn Co etc. or broader class

like layered, spinel, and olivine. This type of classification overlaps strongly with bulk material research which has been thoroughly reviewed in several excellent articles [51-53].Traditionally thin film battery researchers have employed RF sputter due to its relative simplicity and popularity in semiconductor industry. More recently, CVD and ALD techniques as well as solution based synthesis techniques are being explored. While all these technique come with its advantages and disadvantages, these methods become important as material development approach closer to commercialization.

1.4 Anode

As mentioned earlier the anode undergoes spontaneous oxidation during discharge. Thus this electrode donates electrons that flow through the external circuit while simultaneously transferring Li ions into the electrolyte. Anode materials should have low potential vs. a standard electrode to provide high open circuit voltage. It should react reversibly with lithium without structural damage. Other requirements that are common with all electrodes include high ionic conductivity and large volumetric and specific capacity.

1.4.1 Li Metal

Li metal provides for a pure anode without other candidates that provide framework for Li ions. Moreover, with an atomic weight of 6.94 and density of 0.534 g/cm^3 it gives high specific and volumetric capacity. It has a theoretical capacity at 3860 mAh/g. However, its high reactivity makes handling it very difficult. While Li is the best choice for anode,

practical limitations limit its use. The μ_A for Li is above most known electrolytes. While the SEI layer allows for some protection, eventually this layer develops local cracks, which then leads to dendrite formation. This can in turn cause internal short. Excellent reviews are available for readers interested specifically in anodes [54-56]. The anodes being used or developed can be classified as carbonaceous compounds, metal alloys and Li based transition metal oxides.

1.4.2 Carbon Based Anodes

Carbon occurs in a variety of form from coke to diamond. A lithium atom reacts with 6 carbon atoms. Graphite, amorphous carbon, grapheme and carbon fiber have been explored as anodes. The potential of carbon anodes vary between 0 and 0.25 V. The theoretical capacity depends on the density of the structure; graphite has a theoretical capacity of 372mAh/g. These are low cost and provide good electronic conductivity. The reversible intercalation reaction of Li in carbon is given as,

$Li + 6C \rightleftharpoons LiC_6$

Since the reduction potential of C is higher than Li, electrolyte decomposition results in formation of passive SEI layer. which stabilizes the anode[57]. However, this leads to an irreversible capacity loss. Attempts are ongoing to develop additives that will enable formation of compact SEI layer before electrolyte decomposition.

1.4.3 Metal Alloy Anodes

As mentioned earlier, Li metal anodes have not been commercialized due to safety concerns. As an alternate metals that form alloys with Li which take the form Li_yM(M = Al, Sn, Pb,Si etc.)have been explored. Unlike intercalation structures, these anodes alloy with Li metal at specific voltages during charging and de-alloy during discharge. The reaction is given as follows,

$xLi + M \rightleftharpoons Li_xM$

These can potentially deliver very high capacity. For instance, Si based anodes can give a capacity as high as 4000 mAh/g[58]. However, some limitations exist. These materials generally have higher reduction potential and will lead to lower cell voltage. Another problem occurs due to the large volume expansion during cycling which causes the anodes to crack during cycling. Recently, LiSi has become popular due to implementation of nano-structured Si has proven successful in controlling volume change. Si based anodes can give very high capacity (1000 mAh/g)[58]. Other strategies include use of multi-metal alloys like SnMn, SnFe etc.

1.4.4 Transition Metal Oxide

Transition metal oxide anodes can be broadly categorized as either Li reactive or intercalation types. The reactive ones typically react with lithium, while the latter jut allows lithium to intercalate the structure. Typical materials belonging to the reactive type include CoO, NiO and TiO_2. The intercalation types operate similar to $LiCoO_2$. Transition metal

oxides like $Li_4Ti_5O_{12}$ allow for intercalation with very little volume change. This greatly reduces structural deterioration. The redox reaction governing the reaction is given by,

$Li_4Ti_5O_{12} + 3Li \rightleftharpoons Li_7Ti_5O_{12}$

Other metal oxide anodes include MnO_2, Mn_2O_3, TiO_2, SnO_2 etc. These materials have been covered in details in several available reviews [59, 60] .The different anode materials are compared in the table below [61-64].

Table 1.1Anode materials for Li ion battery

Anode	**Theoretical Capacity (mAh/g)**	**Nominal Capacity (mAh/g)**	**Potential vs Li/Li+ (V)**
Li Metal	3800	Not Commercialized	0
Graphite	372	360	0.1
Silicon	4200	1000	0.15
$Li_4Ti_5O_{12}$	175	135	1.55

1.5 Cathode

The cathode undergoes spontaneous reduction during discharge by accepting electrons. The two major classes of materials that meet these criteria are anion close packed transition metal layered oxides like $LiCoO_2$ which are very compact structures which give high energy storage per unit volume. The second category consists of more open structures like spinel $LiMn_2O_4$ or olivine $LiFePO_4$ which can be potentially much cheaper and in the latter case more stable due presence of PO_4^- ions.

1.5.1 Layered Oxides

All cathode materials of this type take the form $LiMO_2$ (M = No, Co, Mn, Fe…….). The structure consists of oxygen atoms in a closed pack structure. This structure has four tetrahedral or two octahedral interstitial sites. Geometrically the tetrahedral sites can accept ions with ionic radius ratio of $0.225 \leq r/R \leq 0.414$, while the octahedral sites can accept ions with ionic radius ratio of $0.414 \leq r/R \leq 0.732$. Most of the transition metals of mentioned above fall in the latter range, and hence occupy the octahedral sites. Thus the structure

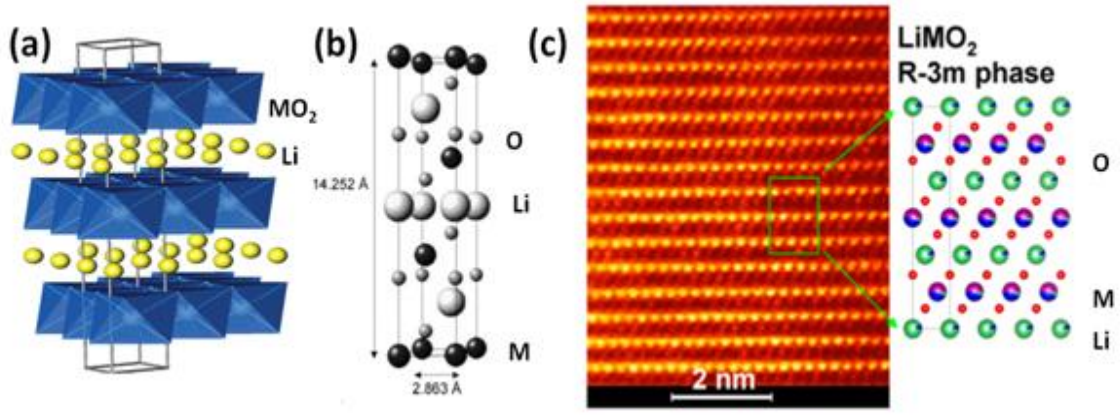

Figure1.10. (a) Schematic of layered $LiMO_2$ crystal structure[65], (b) $LiMO_2$ unit cell [66], (c) STEM image with element map[67] and atomic model projection of marked green area.

consists of alternative slabs of MO and LiO, were the cation occupy the respective octahedral site[68].Figure 1.10 shows the schematic as well as high resolution STEM image of a typical $LiMO_2$ material. The Li ions move along the two dimensional layered planes during intercalation/de-intercalation leading to higher ionic conductivity. When lithium is removed

from the structure during charging, the repulsion between the oxygen atoms in the adjacent MO_2 layer expands the lattice. When Li is completely removed the lattice contracts rapidly into a more stable structure. For instance, $LiCoO_2$ changes from and O3 to a P3 type structure. Thus for stable operation $LiCoO_2$is generally de-lithiated only up to 50%[68]. A possible solution to this limitation is multi cation layered oxide[69]. For instance $LiNiCoO_2$is stable for Li extraction up to x=0.7. However, only Ni undergoes redox reaction and Co doesn't. This limits the theoretical capacity to 230 mAh/g and a practical capacity of 163 mAh/g[70, 71]. $LiNi_{0.33}Mn_{0.33}Co_{0.33}O_2$along with other ratio permutations are fast becoming a popular cathode material [72, 73]. Similar to other materials in this class the lattice parameter c increases with Li extraction and eventually the c lattice parameter contracts. However the lattice constant 'a' increases and the net volume change is minimized. Unlike $LiCoO_2$ which takes a P1 form at x=1, it takes an O1 form. It can be stably operated in the range, $0 \leq x \leq 0.8$ and depending on the ratio of the cations give up to 180 mAh/g capacity. Wei G. et al., explored RF sputtered $LiCoO_2$ for electro chromic applications as early as 1989 [74, 75]. Bates and co-worker reported all solid state batteries with V_2O_5 cathodes with Li metal counter electrode[76]. Dahn's group investigated effect of laser ablated growth of $LiCoO_2$ under varying temperature and partial pressure. As temperature was varied from 250 °C to 450 °C to 680°C they reported rock-salt, spinel and hexagonal structure respectively. Changing pressure was shown to effect stoichiometry and to an extent the phase as well [77]. Bates et al., reported that strain energy densities for the 101 plane is lower than those for the 003 and 104 planes and hence film thicker than 1 um oriented along the 101 direction

when annealed at 675 °C to minimize volume strain energy[78]. Compared to $LiCoO_2$, $LiMn_2O_4$ is a potentially challenging candidate for thin film deposition. Stoichiometric variations of Mn, Li and O leads to formation of impurity phases like Li_2O, MnO_2, $Li_4Mn_5O_{12}$, Li_2MnO_3 etc. Never the less several groups have reported stoichiometric films [79-81]. Interest in multi cation film is primarily driven by expected structural stability and electrochemical performance. Thin film work on other cathodes like $LiNi_{0.5}Mn_{1.5}O_4$ [82], $LiNi_{0.33}Mn_{0.33}Co_{0.33}O_2$[83, 84] etc., mostly using sputter have been reported. A majority of the work mentioned above rely on a common approach, room temperature deposition followed by annealing. This approach, while great for simple cathodes can have potential limitations when applied to engineered and next generation designed architecture cathodes. A post deposition anneal based recipe can potentially cause delamination in case of a multi component system such as solid state battery due to different materials with different adhesion and thermal properties. Traditional techniques like strained layer, epitaxial growth, etc. need high temperature deposition. Furthermore, repeated heating and cooling, even if feasible would be a time consuming and expensive process. However, several limitations need to be overcome to develop high temperature deposition recipes. For instance physical vapor deposition techniques are prone to Li loss related stoichiometry problems. Larger grains or perfect epitaxial films can reduce Li diffusion coefficient. Even in case of simpler systems like $LiCoO_2$, deposition can lead to impurity phase formation. We successfully demonstrated such a high temperature one step deposition recipe using pulsed laser deposition for the first time using pulsed laser deposition [84]. Not only was the film

impurity free, it also gave comparable or better results to most other bulk and thin film works reported. Another popular approach, parallel to thick film work is coating of thin film cathodes with a passive material like Al_2O_3[79, 85], ZnO[79], Mn_2O_3[86] etc. which rely on very thin barrier coating to suppress surface reaction. Another approach to tune material properties are by introducing strained layers, or selective doping at interface or surface area [87, 88].Sauvage et al., reported that films thicker than 150 nm showed an increase in capacity upon cycling and attributed it to larger defect density on the surface of thicker films due to reduced substrate strain effect with increased film thickness [89]. It is possible that upon cycling the diffusion depth increases perhaps aided by defect driven diffusion. This is supported by observations by Xie et al., who reported higher diffusion co-efficient for thicker film [90]. Another substrate effect that has been exploited is the orientation and texture of the film based on substrate selection [90].Several researchers have attempted to improve conductivity by doping the film. Attempts have been made to deposit films with carbon additives by using a carbon source like an organic binder in the target. While the carbon incorporation is a fraction of those in thick film battery it has been reported to improve capacity[91].Electrodes have also been developed with certain physical forms that might optimize performance like 3D structures. The 3D architecture can be implemented as simply as using 3D current collector, complex photolithography schemes or creative self-assembly recipes. Ugo and co-workers used electrostatic spray pyrolysis to deposit $LiNi_{0.5}Mn_{1.5}O_4$ film on patterned silicon substrate[92].Yim and co-workers used a similar technique and sputter deposited $LiSn_{0.0125}Mn_{1.975}O_4$ thin film cathode on a polystyrene bead based templates [93].

While most 3D works concentrate on physical optimization of structure to optimize battery performance, a more sophisticated approach would entail chemical-structural architecture optimization.

1.5.2 Spinel

This class of cathode has a cubic close packed structure of the form LiM_2O_4(M = Ti, V, Mn…….). The best know material in this class is $LiMn_2O_4$ where the Mn can be present in either the tetrahedral or the octahedral sites and its oxidation state can vary between +2 to +4[94, 95].It has a lattice constant of a = 8.245 Å. Figure 1.11 shows the crystal lattice representation and high resolution STEM image of $LiMn_2O_4$.Depending on its valence Mn exhibits redox reaction at 3 V and 4 V. In $Li_{1-x}Mn_2O_4$, for $0 \leq x \leq 2$ it maintains its cubic structure and displays a plateau at 4 V. For $1 \leq 1+x \leq 2$, $Li_{1-x}Mn_2O_4$, transforms into tetragonal $Li_2Mn_2O_4$ and the Mn redox reaction occurs at 3 V. However it is operated primarily around 4 V to prevent irreversible capacity loss and hence limited to a practical capacity of around 120 mAh/g. Another major problem is the dissolution of Mn. At the surface Mn^{3+} ions dissociate into Mn^{2+} and Mn^{4+} ions as follows,

$2Mn^{3+} \rightarrow Mn^{2+} + Mn^{4+}$

The Mn^{2+} dissolves in the electrolyte. These ions deposit on the anode further reducing the capacity[98]. Several different strategies have been explored to limit Jahn-Teller distortion.

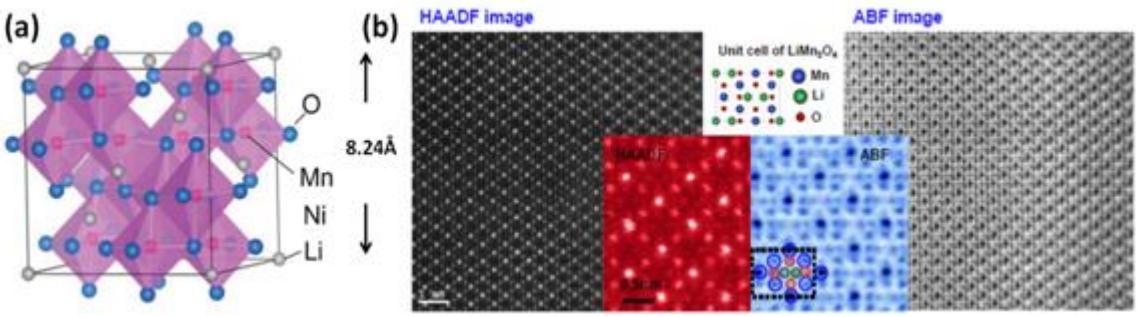

Figure1.11. (a) Crystal lattice[96], (b) high angle annular dark Field(HAADF) for identifying heavier Mn atoms and Annular Bright Field(ABF) image for identifying the lighter Li and O atoms, of $LiMn_2O_4$ with a projected unit cell schematic of spinel $LiMn_2O_4$[97].

Partial substitution of Mn with Co, Ni etc. has lead to improved stability. Yet another approach is to substitute some oxygen with fluorine. Yet others attempted to use coating to suppress reaction with electrolyte[99]. Stabilized $LiMn_2O_4$ is popular for high power applications like hybrid vehicles and subject of continued research interest. A slightly different approach is to dope with native cation i.e. an intrinsic doping with the major cation in the film. One such work was reported by Bates et al., co-deposited $LiMn_2O_4$ with Mn from a pure Mn source. This was shown to suppress an observed redox peak 4.6 V[100]. Another, Mn based materials that recently generated a lot of interest is Li_2MnO_3. While traditionally inactive, it has been shown to become electrochemically active by acid etching. We proposed and successfully demonstrated an alternate way of activating thin film Li_2MnO_3 film. A PLD based technique that can vary stoichiometry in-situ and generate defects in the film during deposition. The resultant film showed good electrochemical property and capacity[101]. This work is described in more details in later sections.

1.5.3 Olivine

Fe is a cheap and widely occurring element and attempts were made to develop Fe based layered oxide. However, it was found to extremely unstable and difficult to synthesize. Padhi and co-workers first reported $LiFePO_4$ in 1999[102]. It's a distorted hexagonal close packed structure. 1/8 of the tetrahedral interstitial vacancies are occupied by P and ½ of the octrahedral sites is occupied by Li and Fe. This three dimensional structure belongs to the *Pnma* space group and is shown in figure 1.12. $LiFePO_4$ has an operating voltage of around 3.5 V and gives a capacity of 170 mAh/g[51]. Unlike the metal oxide cathodes that become unstable upon removal of more than 50 % of the Li. However, the strong bonding of the PO_4^- radical stabilizes the structure allowing 100% Li removal. During deintercalation, $FePO_4$ is formed and co-exists with $LiFePO_4$. At the end of the Li extraction all the $LiFePO_4$ is converted to $FePO_4$. The $FePO_4$ structure is similar to $LiFePO_4$,and hence these cathodes are extremely stable. These materials have poor conductivity compared to other cathode materials and generally require conductive coating or additives to compensate. The diffusion rate of Li is also relatively low. When Fe is partially or completely substituted by other ions like Mn, Co etc. operating voltage can be tuned to higher voltages[105].Olivine thin films of $LiFePO_4$ have been demonstrated despite its low intrinsic conductivity. While the conductivity problem will occur in most thin films, this is very apparent in $LiFePO_4$ as demonstrated by Song and co-workers by recording normalized capacity variation with

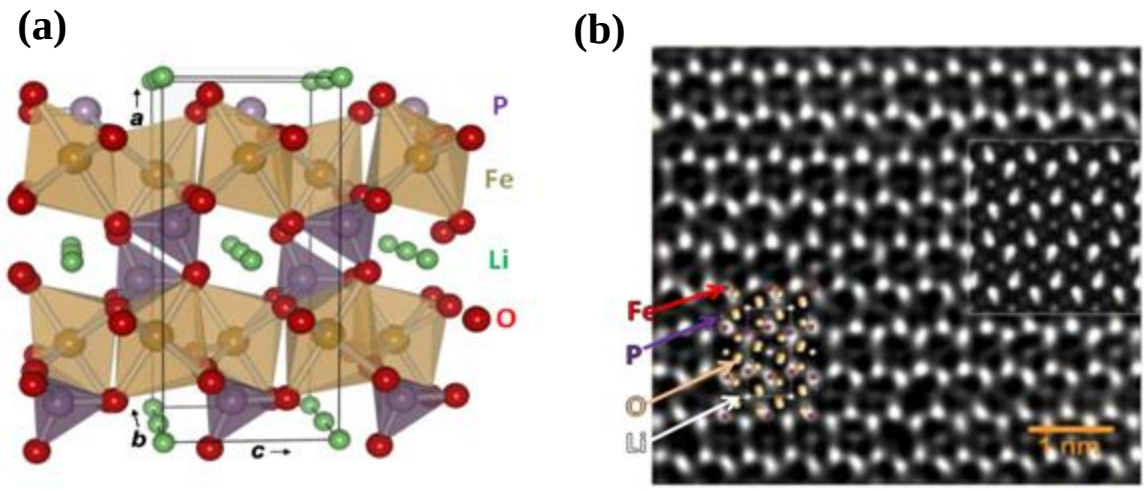

Figure1.12. (a) Crystal model [103] and, (b) HAADF STEM image showing some partial substitution of Li sites by Fe, $LiFePO_4$[104].

thickness[106]. Similar to doping work in layered materials, Xie et al., attempted doping $LiFePO_4$with Ag up to 10% by weight and reported improved capacity [86]. Similar work has been reported with 1 % Cu doping as well [107].

1.5.4 Li-Rich Cathodes

Several different strategies have been explored to stabilize layered metal of the $LiMO_2$ class. This includes doping with multiple transition metal ions as discussed earlier. Hunter and co-workers had shown earlier that acid etching of $LiMn_2O_4$ lead to a stable composite material consisting of λ-MnO_2 with a spinel Mn_2O_4 framework[108]. Thackrey and co-workers demonstrated that chemically etching Li_2MnO_3 a similar structure x Li_2MnO_3.(1-x)$LiMnO_2$ can be obtained[109]. This can be thought of as an alternate to cation substation, i.e. by substituting metal oxide sub units like MnO_2 instead of metal ions to

stabilize the structure. While several different schemes were attempted and Li_2MO_3 (M= Mn, Ti, Zr) was found to yield the best results. Both Layered-layered integrated structures (Li_2MO_3 –$LiMO_2$) and Layered-Spinel (Li_2MO_3-LiM_2O_4) were investigated. The former was found to have superior capacity, close to 300 mAh/g and has been of great interest as a potential next generation cathode material. The compatibility stems from similarities in the crystal structure of the two phases even though $LiMO_2$ is trigonal with $R\bar{3}$m space group and Li_2MO_3 is monoclinic with $C2/m$ space group. Li_2MO_3 can be represented in layered form (like $LiMO_2$) as $Li[Li_{1/3}Mn_{2/3}]O_2$. Thus 1/3 of the Mn ions in the layered $LiMO_2$ structure are replaced by Li ions to obtain the Li_2MnO_3 structure. In fact the interlayer spacing for both $LiMO_2$ and Li_2MnO_3 is around 4.7 Å. While the two phase nomenclature simplifies analysis and understanding, traditionally the material is synthesized in a single process similar to traditional $LiMO_2$ powder. However, the precursors are proportioned for excess Li and Mn enabling the Li-rich synthesis. Thus the actual form of Li-rich mentioned earlier as $xLi_2MnO_3 \cdot (1-x)LiMO_2$ (M = Mn, Ni, Co, Fe, Cr, etc.) is in fact written as $Li_{1+(x/(2+x))}M'_{1-(x/(2+x))}O_2$. Since it has been established that the stabilized structure leads to better electrochemical stability, understanding the structure becomes critical. The similarity between the monoclinic and trigonal structures and one step synthesis has lead to two different interpretation of the structure. Some researchers believe it to be a homogeneous solid solution while others feel it contains two distinct phases, namely Li_2MnO_3 and $LiMO_2$. Similarity in crystal structure makes this difficult to differentiate using imaging and diffraction studies. This can be seen clearly in figure below.

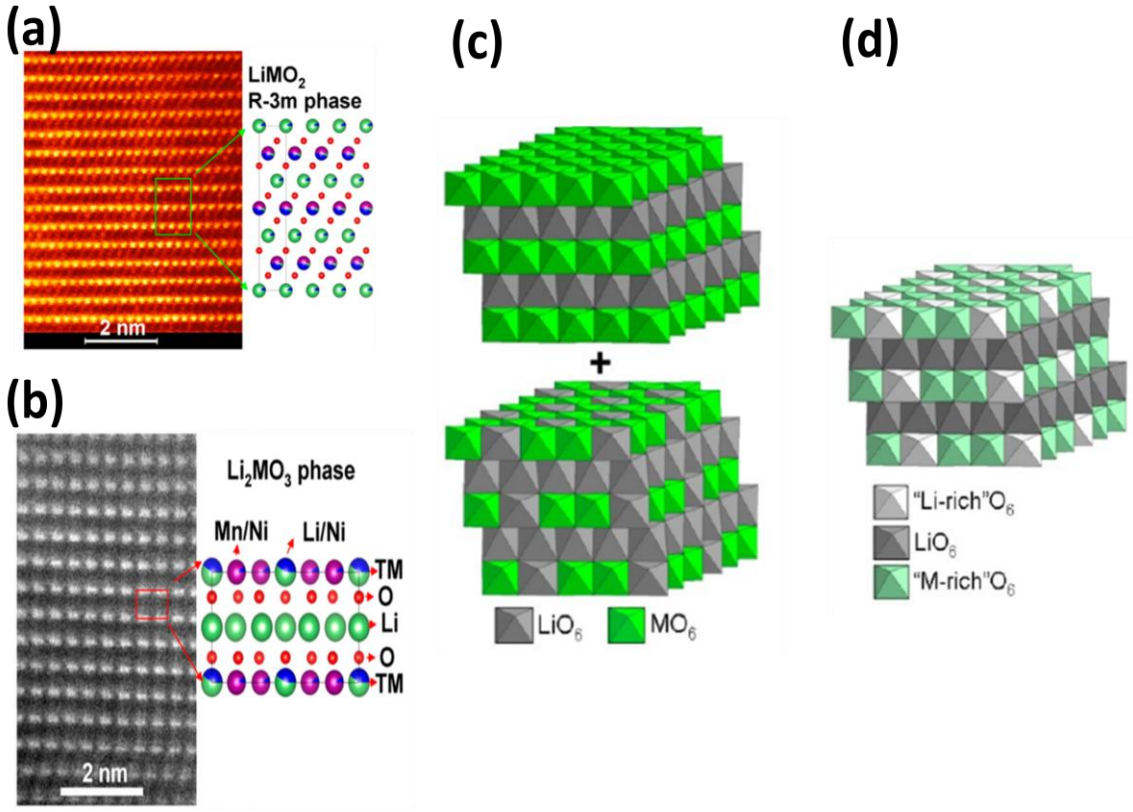

Figure 1.13 STEM image of a) $LiMO_2$ layered structure, b) Li_2MnO_3 crystal structure, c) crystal model of the layered and monoclinic phases as separate phase and, d) a single phase Monoclinic like model of Li-rich cathode[67, 110].

Researchers have proposed a solid solution with either $R\bar{3}$m structure or C2m[110]. It has been observed that as the composition (x) changes the lattice parameter changes linearly which seems to follow Vegard's law [111, 112]. On the other hand, several researchers have found local Li_2MnO_3 regions inside the Li-rich regions. High resolution imaging has shown dumbbell like structure formed by the double Mn atom [113, 114]. The two representative imaging work supporting the two theories is shown in figure 1.14.

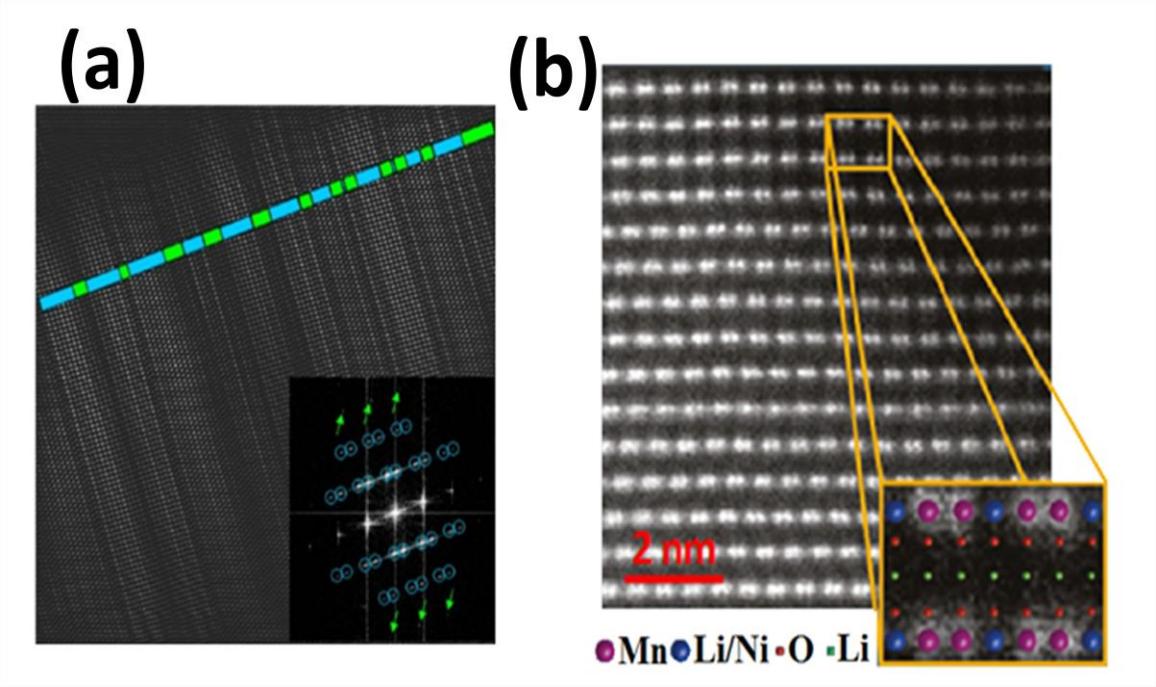

Figure 1.14.High resolution STEM image showing Li rich electrode to be, (a) two phase and (b) single phase.

In our work we have proposed a thin film model based approach to investigate this further. Briefly, models designed with nano-domains of Li_2MnO_3 in a layered metal oxide $LiMO_2$ gave electrochemical performance characteristic of Li-rich material. While the electrochemical operation for Li-rich cathodes is not well understood, the following mechanism has been observed during cycling. During initial cycling of the Li-rich cathode between 2.0-4.4 V vs. Li/Li^+, the Li_2MnO_3 component is not electrochemically active. Only the $LiMO_2$ component provides the Li for the redox reactions and resulting capacity at this stage. When the cycling voltage exceeds 4.4 V vs. Li/Li+, the Li_2MnO_3 component becomes electrochemical active and lithium ions are extracted from Li_2MnO_3 along with a

simultaneous release of oxygen. This can be thought of as Li_2O extraction and leads to spinel phase transformation of the Li_2MnO_3component. The excess Li in the structure serves to compensate the overall structure when delithiation exceeds the limit of the $LiMO_2$ component. Excess Li has the additional benefit of reducing transition metal ion substitution in the Li layer. During battery cycling Li extracted from the tetrahedral sites is replaced by Li from the octahedral sites in Li_2MnO_3, stabilizing the structure.

While the monoclinic and layered phase are separated for nomenclature and explanation, almost all thin and thick film work for Li-rich cathodes use the unified synthesis approach. Baggetto and co-workers deposited Li rich cathodes directly from pre-synthesized material using RF sputter [115]. Surface reactions were investigated in this work to understand capacity degradation. However, no structural optimization was attempted. Some precedence for composite films exists in other material system. For instance, an interesting approach to modifying cathode properties is to fabricate inorganic-organic composite cathode. Kuwabata et al. reported a composite polypyrrole-MnO_2 film. Polypyrrole acts as both an active redox material as well as conductive framework for MnO_2[116]. Similar work has been reported for polyaniline-V_2O_5 composite [117]. We have shown that by using optimized schemes of $Li_2MnO_3$and $LiNi_{0.5}Mn_{0.3}Co_{0.2}O_2$ can give the characteristic high capacity of Li-rich cathodes[118]. Detailed investigation into effect of structure and composition will be covered in this work. A brief comparison of some of the common cathode materials is given in the table below [61, 119-122].

Table 1.2 Comparison of cathode materials

Cathode Material	Theoretical Capacity (mAh/g)	Nominal Capacity (mAh/g)	Potential (V)
$LiCoO_2$	274	150	3.9
$LiNi_{0.5}Mn_{0.3}Co_{0.2}O_2$	278	170	3.9
$LiMn_2O_4$	148	130	4.0
$LiNi_{0.5}Mn_{1.5}O_4$	147	140	4.4
$LiFePO_4$	170	160	3.4
Li-Rich	360	300	4.4

1.6 Electrolyte

Electrolytes can be liquid or solid medium, which provides high ionic conductivity and low electronic conductivity. In addition to conductivity requirements potential electrolytes should not react with electrodes over the entire voltage and temperature range as well as be relatively inexpensive. Liquid electrolytes can be aqueous or organic. Lithium ion batteries operate at high voltage and mostly use organic liquid electrolytes since they don't decompose at voltages as high as 4.8 V. Solid electrolytes are either inorganic compounds or polymers.

1.6.1 Liquid Electrolytes

Liquid electrolytes are designed to meet several criteria for good performance in li ion battery[123]. A high dielectric constant, nominally over 20 is recommended for solvents. The

dielectric constant of the solvent is proportional to it ionic dissociation strength, and since Li based salts are difficult to dissociate a high dielectric constant (ε) is recommended. Also from stokes law we know that ionic mobility in inversely proportional to viscosity, and generally a viscosity of less than 1 cP is preferred. In general solvents with high dielectric constant have high viscosity and polarity. Hence often a mixture of solvents is used in practice. Finally from a safety point of view solvents with higher boiling point and vapor point are preferred. The properties of several electrolyte solvents are listed in table 1.3. [124-127] Li based salt s that are easier to dissociate are preferred. As a general rule salts with large anions are easier to dissociate. Some common Li salts used include $LiClO_4$, $LiBF_4$, $LiPF_6$. Due to stability issues during charging $LiClO_4$ is used mostly in primary batteries. Fluorinated salts have good solubility and stability. $LiPF_6$ has high ionic conductivity but poor thermal stability. Commercial batteries frequently employ additives to enhance stability of the electrolyte using appropriate SEI formation additives (eg. Vinylene carbonate (VC)). In addition electrolyte additives are also used as overcharge inhibitors, ionic conductivity enhancers and flame retardants[128].

Table 1.3 Comparison of organic solvents for Li ion battery

Solvent	**Ionic Conductivity (s/cm)**	**ε**	**Viscosity (cP)**	**T_m (^oC)**	**T_b (^oC)**
Ethylene Carbonate (EC)	7.2 e^{-3}	89.6	1.86	39	248
Propylene Carbonate (PC)	5.8 e^{-3}	64.4	2.53	-49.2	241
Dimethyl Carbonate (DMC)	7.1 e^{-3}	3.11	0.59	0.5	90
Ethylmethyl Carbonate (EMC)	4.6 e^{-3}	2.96	0.65	-55	85
Diethyl Carbonate (DEC)	3.1 e^{-3}	2.81	0.75	-43	126

1.6.2 Solid Electrolytes

Solid electrolytes offer several advantages over liquid electrolytes. Solid electrolytes can be classified as polymer electrolytes and solid state electrolytes like LiPON.

1.6.2.1 Polymer Electrolytes

The different types of polymer electrolyte include solid polymer electrolyte, gel polymer electrolyte and polyelectrolyte[129, 130]. Solid polymer electrolyte consists of polymers and Li salt. The motion of polymer chains drives ionic conductivity in solid polymer electrolytes. The ease of packaging, elimination of leakage problems, and elimination of a dedicated separator make this a popular choice. Some well researched solid polymer electrolytes include, poly(ethylene oxide) (PEO), poly(propylene oxide) (PPO), polyphosphazene, and polysiloxane. Gel polymer electrolytes use liquid electrolytes in polymer gels along with lithium salts. The liquid electrolyte controls the ionic conductivity

while the gel provides the mechanical strength. The liquid electrolyte component provides high ionic conductivity (~ 10^{-3} S/cm). This gives performance comparable to liquid electrolyte while giving most of the advantages of solid polymer electrolytes. Some common polymers used for gel polymer electrolytes include polyacrylonitrile, poly(vinylidene fluoride) (PVdF), poly(methyl methacrylate) (PMMA), and PEO.Polyelectrolyte's use polymers that directly dissociate into cations and anions. The cations and anions move independently of each other and hence they are also called single ion conductors. In lithium ion batteries the Li cation can move freely through the electrodes but anions accumulate at the surface. Hence, these are designed such that the anions must be fixed to the polymers. These generally have ionic conductivity of around 10^{-6} S/cm [130-133].

1.6.2.2 Solid State Electrolyte

The gel electrolyte above is the most popular solid electrolyte commercially. However, despite the packaging advantages, they still suffer from the same limitation as other liquid electrolytes. Solid state electrolytes on the other hand are true solid electrolytes and are based on inorganic compounds. While the ionic conductivity for these electrolytes can be orders of magnitude higher than liquid electrolyte, they can be made significantly thinner to compensate to an extent. They also benefit from the compatibility with conventional thin film tools allowing for greater integration. Other advantages include improved safety due to lack of flammable electrolytes, leakage proof, potentially higher operating voltage and temperature and significantly better shock and stress proof

construction. While a wide range of solid electrolytes are currently under investigation, a majority of these can be classified as crystalline and amorphous electrolytes[130].

1.6.2.3 Crystalline Electrolytes

These include pervoskite, NASICON,LISICON and Garnet type electrolytes[134]. The pervoskite (ABO3) type Lithium Lanthanum Titanate (LLTO) is a typical material of this class. This crystalline electrolyte can have conductivity a high as 10^{-3} S/cm. A combination of vacancy sites and excess Li allows for the high ionic conductivity. However LLTO reacts strongly with Li metal and cannot be used directly with Li anode. LISICON electrolytes have a γ-Li_3PO_4 like orthorhombic structure. $Li_{14}ZnGe_4O_{16}$ is a typical electrolyte in this class. In it s native form it has a relatively poor conductivity (10^{-6} S/cm) and react with Li just like the pervoskite LLTO. Kanno et al. introduced sulfide groups in the structure and observed significant improvement in the conductivity. For example $Li_{4-x}Ge(Si,P)_{1-y}M_yS_4$ (M = Tri or tetra valent cation) has been shown to have conductivity as high as 10^{-4} S/cm. These are generally called thio-LISICON electrolytes. Some of the promising materials investigated in this class include $Li_{3.25}Ge_{0.25}P_{0.75}S_4$, $Li_{3.4}Si_{0.4}P_{0.6}S_4$ etc. These materials are unstable in its bulk form, making handling it difficult. Garnet type electrolytes of the form $Li_5La_3M_2O_{12}$ (M=Ta, Nb) was first reported by Weppner and Thangadurai. These are highly stable and can operate up to 6 V vs Li/Li^+. These have been shown to have ionic conductivity of around 4 x 10^{-5} S/cm and efforts are ongoing to further improve this[130].

1.6.2.4 Amorphous Electrolytes

It was found that mechanical ball milling tends to improve ionic conductivity of relatively poor conductors. For example $LiNbO_3$ or $LiTaO_3$ show a conductivity of 3×10^{-6} S/cm. Closer investigation reveals high defect concentration, with highly disordered structure not unlike amorphous structure. Another popular electrolyte in this class, first reported by Bates et al., is LiPON. LiPON is obtained by partial substitution of nitrogen in the Li_3PO_4 structure. These are orthorhombic structures and occur in low temperature form as β-Li_3PO_4 ($Pmn2_1$) and high temperature form γ-Li_3PO_4 (Pnmb). In its crystalline form all Li ion sites are occupied and the lack of Li ion movement leads to poor ionic conductivity (10^{-18} S/cm). Defects and disordered structure can be used to increase both mobile Li ions and conducing paths. Another, more successful strategy has been nitrogen doping. In the resulting oxynitride structure oxygen in the PO_4 group is thought to be substituted with di-coordinated (-N+) or tri-coordinated (-N<) nitrogen. The increase in cross linking due the tri-coordinated Nitrogen, as well as the reduced electrostatic energy due to introduction of the more covalent P-N bond instead of the P-O bond have been attributed with the increase in ionic mobility. Yet another consideration is the larger size of N^{3-} (1.32 Å) as compared to O^{2-} (1.24 Å) leads to distortion and larger ion conducting channels. The glassy nature of the electrolyte makes structural study difficult. As an alternate crystalline LiPON was investigated[130]. However crystalline forms had conductivity in the range of 10^{-13} S/cm. A comparison of different solid state electrolyte is shown in the table 1.4 [130, 133, 134].

Table 1.4 Comparison of solid electrolyte for Li ion battery

Class	Example	Structure	Ionic Conductivity (S/cm)
Pervoskite	$Li_{3x}La_{2/3-x}TiO_3$	Crystalline	10^{-3}
NASICON	$Li_{1.3}Al_{0.3}Ti_{1.7}(PO_4)_3$	Crystalline	3×10^{-3}
LISICON	$Li_{14}ZnGe_4O_{16}$	Crystalline	10^{-6}
Thio-LISICON	$Li_{3.4}Si_{0.4}P_{0.6}S_4$	Crystalline	6.4×10^{-4}
Garnet	$Li_6La_2BaTa_2O_{12}$	Crystalline	3×10^{-3}
Li_3PO_4	Li_3PO_4	Amorphous	10^{-18}
LiPON	$Li_{2.88}PO_{3.73}N_{0.14}$	Amorphous	3.3×10^{-6}

1.7 Motivation for this Work

Lithium ion battery is a popular storage solution but, despite extensive research, only a handful of chemistries have been successfully commercialized. In this work we implement a unique thin film approach to investigate next generation cathode materials.

As mentioned earlier, thin film batteries have been a topic of research for a long time. However, interest in this field has been primarily to develop solid state battery for well-established chemistries developed by bulk battery researchers. Until recently, the biggest hurdle to this has been the inability of solid state electrolytes to provide ionic acceptable ionic conductivity, if not comparable to liquid electrolyte. Now, the first generation solid electrolytes have developed a small commercial market and several fast conducting next generation electrolytes are being explored[132, 135]. Now, there is a need to develop next

generation electrodes for batteries in general and solid state batteries in particular. This work proposes the use of various thin film deposition tools and techniques to evaluate existing materials as well as to develop new materials. Furthermore, we aim to utilize the work of other researchers as well as our experience in first generation, simple single phase electrodes to engineer electrodes with enhanced properties as well as develop new architectures. This can be implemented in various ways, some of which are listed below,

1) Since thin films allow for materials to be synthesized and manipulated at the atomic level, it is possible to recreate most battery materials in a precise manner. This can be used to investigate various structure related effects on electrochemical properties of materials.
2) Mathematical modeling and simulation of different electrochemical phenomenon in complicated composition and phase is always a challenge. Thin film electrodes can be designed to systematically carry out experimental and correlating simulation to study these materials.
3) Most electrode materials today are often synthesized via the chemical processing route using either solid state or solution based methods. While this works for simple structures like $LiCoO_2$, $LiFePO_4$ etc., in case of more complex materials like Li_2MnO_3-$LiMO_2$ it raises questions about crystal structure, phase as well as its transformation and degradation mechanisms. Thin film techniques can be used to make model cathodes to isolate and test hypothesis about the microstructure, phase, transformation and degradation.

4) Compositional variation of electrode materials i.e. stoichiometric variations or doping, can be performed by minor modification to the deposition process. This allows for faster screening of potential candidates.
5) Thin film electrodes and electrolytes can be engineered using various approaches as strain engineering, 3D architectures, microstructure optimization, doping etc. to develop materials specifically for next generation solid state batteries.

In this work we try to develop some techniques to investigate materials of interest. We develop thin film processes compatible with various thin film optimization techniques for future development. We explore advanced film engineering to optimize cathode films for both thin film batteries and to guide general battery research. New approach to advanced architectures for batteries is developed and demonstrated for next generation cathode materials. Finally, work on solid state electrolytes is explored to enable transferring the electrode research to full fledge solid state batteries.

1.7.1 Material Selection

As stated above, one of the objectives of this work is to develop and enhance next generation materials for Li ion battery. Material selection is hence critical to direct research efforts in a sustainable and productive direction. The electrodes should meet some general requirements to be suitable for Li ion batteries. These include,

1) It should contain an ion that can readily reduce/oxidize like a transition metal.
2) The structure should not change upon addition/removal of Li ion.

3) It should have high electronic and ionic conductivity.

These criteria has been met in most of the commercially available electrode materials like $LiCoO_2$, $LiNiMnCoO_2$, $LiMn_2O_4$, $LiFePO_4$ cathodes and Carbon based anodes like carbon black and graphite.

In addition to the basic chemical requirements listed above, the next generation cathodes should meet the following criteria in addition to the above requirements,

1) It should have high free energy of reaction i.e. give one or more Li ions per formula and have high reaction potential while still not reacting with the electrolyte.
2) It should be low cost.
3) It should be nontoxic and environmentally friendly.

Traditional cathode materials like $LiCoO_2$ have one Li ion per formula, however only half the Li can be reversibly removed without changing the structure. If one Li can be removed per unit formula, then the theoretical capacity of 300 mAh/g can be achieved, but instead it can only give a practical capacity of around 150 mAh/g. This is the case for most oxygen closed pack transition metal oxides of the $LiMO_2$ (M = Co,Ni,Mn….) class. The use of toxic metals like Co or Ni makes it environmentally hazardous as well. $LiFePO_4$, olivine structure is more stable because of the PO_4^- radical which allows for removal of almost 1 Li ion per formula. However, the chemical potential for this reaction is low (3.4 V). This leads to a low energy density.

In order to enable more Li ion extraction, materials with multiple Li ions per unit formula is preferred. Li based materials like Li_2MnO_3, Li_2FeSiO_4, $Li_3V_2(PO_4)_3$ etc.

To ensure high specific capacity the molar ratio of Li with respect to molecular weight of the material should be high. Also to ensure low cost, relatively expensive metals like Co, Ni etc should be reduced in favor of cheaper and more abundant elements. Finally, toxic components like Co, V etc should be avoided or minimized as much as possible.

Based on these criteria, Mn based cathode materials with high Li content was selected to demonstrate implementation of thin film techniques to study cathode materials for Li ion batteries. As such the techniques developed here can be implemented equally effectively for other cathode, anode and electrolyte materials with properly designed experiments.

Table 1.5 Cost of different cathode materials.

Cathode Chemistry	**Cost (US $/Kg)**
$LiCoO_2$	35-60
$LiNi_{0.8}Co_{0.15}Al_{0.05}O_2$	33-37
$Li_{1.05}(Ni_{0.8}Co_{0.15}Mn_{0.05})_{0.95}O_2$	30-39
$Li_{1.05}(Ni_{0.44}Co_{0.0.44}Mn_{0.111})_{0.95}O_2$	26-29
$Li_{1.05}Mn_{1.94-x}M_xO_4$	10

Table 1.6 Toxicity of different cathode materials.

Cathode Chemistry	Eco-Toxic Potential (PAF m^3 day/KWh)*	Human Toxicity Potential (Cases /KWh)**
$LiNiMnCoO_2$	$2.03e^{+00}$	$6.69e^{-10}$
$LiMnO_2$	$1.54e^{-02}$	$2.66e^{-10}$
$LiFePO_4$	$6.64e^{-01}$	$1.01e^{-09}$

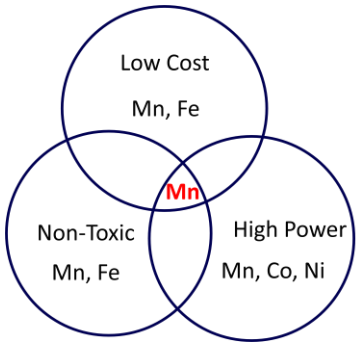

Figure 1.15. Pictograph showing cation selection for cathode oxide.

1.8 Research Outline

While extensive work can be found in literature on RF sputter based cathodes, relatively little work has been done on PLD based cathodes. We will first develop a process suitable for our future research efforts. Conventional thin film electrodes are deposited at room temperature on substrates like Silicon followed by annealing. To enable precise control on stoichiometry, development of model structures, doped materials etc., and the deposition process should meet the following criteria,

1) It should be a one step process, preferentially providing high energy to the film constituents during formation.
2) It should use metal substrates similar to those used for conventional thick film cathodes.

These techniques have been developed and applied for different studies. These include material property investigation of $LiNiMnCoO_2$ films, engineered film studies of Li_2MO_3 films and designed architecture films such as Composite, Nano-domain and Multilayer films. Furtherwork towards solid state batteries requires a solid electrolyte. Towards this with Li_3PO_4 and LiPON electrolyte were investigated. The different works are briefly outlined below.

1.8.1 $LiNiMnCoO_2$

In order to develop this process, $LiNiMnCoO_2$ is chosen as the candidate material. While this does not meet all the criteria listed earlier it does meet it to some extent. It significantly reduces toxic Co content by partial substitution with Ni and Mn. Moreover, both Mn and Ni are potentially cheaper than Co. Also it is possible to stabilize the structure with Ni and Mn to enable extraction of more than 0.5 Li per formula which is the case for $LiCoO_2$. Lastly, since it is a relatively well known material, it sets up a good baseline to compare thin film results of our process with thick film work reported by other groups.

A one step process was developed to deposit $LiNiMnCoO_2$ film on a gold buffered stainless steel substrate. The Au buffer layer provided better template for the oxide film as

opposed to bare stainless steel (SS) substrate or TiNbuffered stainless steel substrate. Au tends to grow in a highly textured manner along the 111 direction and this provided a good template for the $LiNiMnCoO_2$ film. The oxide film itself was deposited at a high temperature (750 °C) under relatively low oxygen partial pressure (mTorr). The film showed good crystallinity and no discernable impurity phase as determined by x-ray diffraction (XRD) and transmission electron microscopy (TEM). Electrochemical evaluation showed that higher capacity was achieved compared to the traditional "deposit then anneal" approach implemented using RF sputter. The cyclic voltammetry results showed that the thin films compared well with the control thick film batteries made in house. The differences noted between the two are considered to be the result of absence of conductive carbon black and polarization in the thin film cathode. This effort met all the criteria for the required process and is used and optimized in the following work.

1.8.2 Li_2MnO_3

As mentioned earlier active materials with more than one Li is attractive because of potentially high specific capacity. However, Mn in Li_2MnO_3 has a +4 valence which means it cannot participate in a redox reaction. Hence by itself it is inactive. Attempts have been made at "activating" it, mostly by acid etching or electrochemical removal of Li partially at high voltage. While this works, the exact reason for this is unclear. Moreover, the resultant material is not stable and hence not commercially viable. A PLD based diagnostic approach can again be used to study this material. One of the theories behind activation is the partial

conversion of Mn^{+4} to Mn^{+3} which is achieved by acid etching. The reduction is achieved by oxygen removal. The conventional approach of acid etching is uncontrolled and cannot be finely controlled. Structural modifications due to the process have proven to be difficult to study. Moreover since studies with Li rich cathodes showed that the performance depends on nano domains of Li_2MnO_3 in NMC, understanding and optimizing Li_2MnO_3 might further help improving the Li rich chemistry. We propose the use of PLD to activate this material in a more controlled manner. This can be theoretical achieved by tuning oxygen content of the film during cathode deposition. If oxygen removal is indeed the sole mechanism behind activation, rather than secondary effects of acid etching (like proton exchange or other byproduct formation) than, we should be able to reproduce these conditions. Also this should enable studies of any accompanying structural transformation. We have been able to demonstrate charge storage in Li_2MnO_3 thin film cathode developed via PLD.One of the parallel mechanism thought to be responsible for electrochemical performance of these cathodes are stacking defects in the film. Investigations into the correlation between defects, oxygen vacancies and electrochemical performance are being carried out using PLD based studies.

1.8.3 Nano-Domain Li Rich Films

A promising class of cathode material generically referred to as Li-rich has been introduced recently. These materials consist of two components a electrochemically inactive component like Li_2MO_3 and an active component like $LiMO_2$ (M = Mn,Co,Ni,Ti…). The

idea is to use the excess Li in the inactive component to stabilize the cathode structure and enable higher Li extraction. This can, under controlled conditions give almost twice the capacity of conventional closed pack transition metal oxide. However, these materials show poor cyclability and rate capabilities. Also potentially higher capacity should be available from these materials, but is not achieved. Part of the reason why it has been challenging to address these issues, is the lack of clarity about its microstructure and phase. One of the questions is whether the Li-rich cathode is composed of two different phases (i.e. its two components) or a new single phase. XRD and TEM analysis of the conventionally synthesized Li rich powder has resulted in contrasting results. The reason for this is that the two components have similar d-spacing leading to difficulty in discerning them. Moreover, the synthesis process is similar to that of $LiMO_2$ class of material with only the molar ratio of the precursor changed to match required stoichiometry. This means that theoretically there is an opportunity for the formation of either two separate phases or a single new phase.

To determine the actual phase and microstructure of these cathodes, traditionally the material is first synthesized and then characterized. Instead, we first fabricate model structures for different possible material configuration using PLD. This is followed by material characterization using techniques like XRD, TEM etc. to verify if desired models were obtained and note any deviations. Finally, these model cathodes are evaluated for their electrochemical properties using discharge capacity, cyclic voltammetry etc. This result is then compared with results obtained for bulk processes for Li-rich cathodes. The model structure that best matches the characteristics of the Li-rich family is the most likely

configuration. In this case we found that nano domains of Li_2MnO_3 in NMC matches best with the characteristics of Li rich cathodes.

1.8.4 Anomalous Behavior of Li_2MnO_3 Films in Free Standing and NMC Matrix

Li_2MnO_3 has been determined to contribute to the electrochemical performance of cathodes both in pure single phase form as well as in a NMC matrix in the Li-rich form. Interestingly, it was found that when films were optimized for standalone single phase performance, the same recipe caused deterioration for the two phase Li-rich system. The reason for this is investigated in this work.

1.8.5 Multilayer Composition Study of Li-rich Film

This study was carried out for a fixed composition, 70 % NMC and 30 % Li_2MnO_3 and the microstructure was tuned to identify the ideal configuration. In the absence of this flexibility, the most common variation attempted in literature is the ratio of the two components. While the material optimization is linked to compositional variation, in light of our previous study, we suspect the microstructure plays an equally important role in device performance. A composition variation study is proposed to investigate the interrelation between composition and microstructure and to determine how it affects the battery performance.

1.8.6 Solid State Electrolytes Li_3PO_4 and LiPON

A wide range of solid electrolytes have been investigated including LiPON and Li_3PO_4. Only one attempt has been reported on depositing LiPON film with PLD during the early development of this film. This is possibly due to the desire to obtain these films in amorphous form which is thought to give good performance. The high energy PLD deposition system, even at room temperature might impart a degree of crystallinity to the film. However, it is well established that interfacial characteristics is critical for ionic conductivity. A highly non-equilibrium technique can possibly enable better interface kinetics with the electrodes. This is the subject of study for this work.

CHAPTER II

RESEARCH METHODOLOGY

The focus of this work is to utilize thin film techniques to investigate properties of next generation Li ion battery materials as well as optimize it for solid state batteries. The standard research methodology used for this work is outline in figure 2.1. An initial requirement for film morphology, stoichiometry and microstructure is determined based on a hypothesis. Recipes were then developed on a pulsed laser deposition system to synthesize

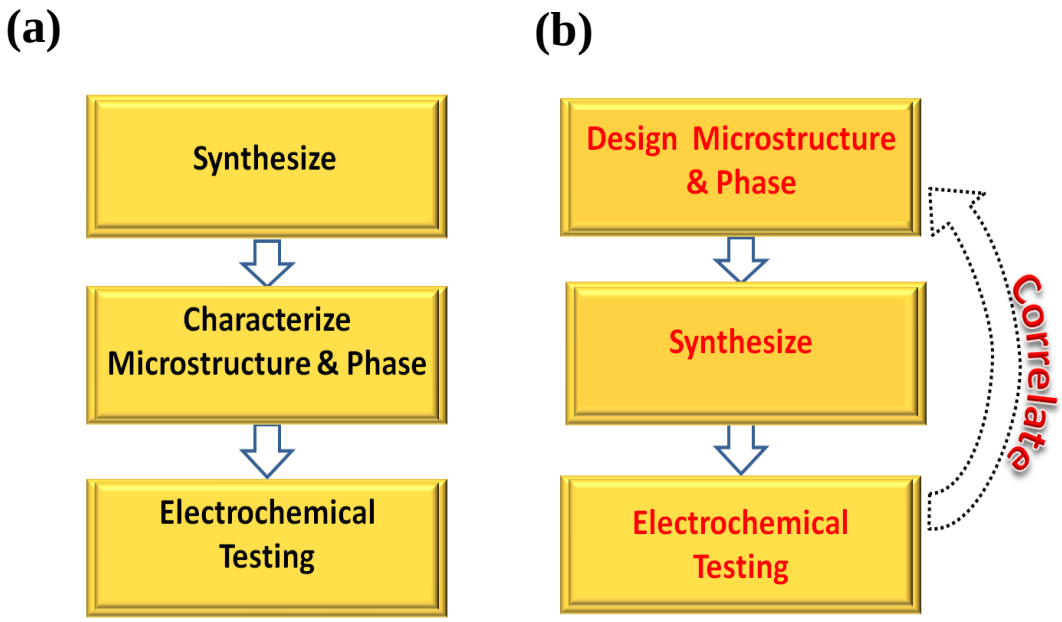

Figure 2.1. Research methodology a) traditional approach, b) this work.

the appropriate films. These were then characterized for phase using x-ray diffraction (XRD), composition using wavelength dispersive spectroscopy (WDS) and secondary ion mass spectroscopy (SIMS), surface morphology using scanning electron microscopy (SEM) and microstructure using transmission electron microscopy (TEM). Coin cells were fabricated for electrochemical testing in a glove box maintained at 0.1 ppm H_2O and 0.1 ppm O_2. These were then tested electrochemically using a dedicated battery tester, an Arbin BT2000 and a Gamry potentiostat.

2.1 Equipment Selection

Thanks to a long history of research and development as well as strong demand for semiconductor devices a plethora of tools and techniques are readily available today. In general these can be broadly classified as physical vapor deposition techniques (RF Sputter, Evaporation, Pulsed Laser Deposition etc.) and chemical vapor deposition (Low Pressure, Plasma Enhanced, Atomic Layer etc.). In addition to these standard methods other solution based techniques for making thin film cathodes are also being explored. RF Sputter is popular due to relatively simple process, well documented processes and ability to scale for industrial application. A variety of films have been demonstrated such as Co_3O_4[136], $LiNi_{0.5}Mn_{1.5}O_4$[82, 137], $LiCoO_2$[138] etc. have been demonstrated using RF sputter. Pulsed laser deposition has also been employed for thin film electrodes such as $LiFePO_4$[139], $LiCoO_2$[140], $LiMn_2O_4$[140]etc. Other techniques like , e-beam evaporation [21], ALD [141-143], Ion beam sputter [144]etc has been explored . Solution based techniques are explored

due to its potential for low cost and can prove to be effective substitute for lot of work done in the form of room temperature deposition followed by annealing. Researchers have reported a variety of techniques such as CuO deposited using spray-pyrolysis [145], $LiCoO_2$ using carbonate solutions [146], $LiMPO_4$ film using electrostatic spray deposition [147] have shown promising results. Despite such a wide variety of techniques, a majority of this work is focused on simple systems such as those cited above. Amongst these, the PLD system is the most versatile tool. In addition to deposition temperature, different gas ambient can be used to control film composition. Even amongst non-equilibrium techniques, PLD can provide higher kinetics to allow a variety of phase modifications. This technique is highly flexible and can be fine-tuned to grow films of desired structure and composition by modifying targets, using multiple targets, changing ambient gas and partial pressure, changing substrate temperature etc.

2.2 Pulsed Laser Deposition

Pulsed laser deposition (PLD) is a physical vapor deposition system which uses an ultraviolet (UV) laser to ablate the target. This creates a directed plasma plume containing ionic, atomic, molecular and even vaporized droplets of the target material. At low energy levels, the thermal evaporation of the target material depends on the vapor pressure of the constituent materials of the target. However, at high energy much larger energy than required for evaporation and this non-equilibrium process allows for stoichiometric transfer of the material from the target to the film[148]. Generally a background partial pressure is utilized

to react with the ions in the plume to form required phase, for instance oxygen ambient is used for oxide films. Also the partial pressure can be used to tune the kinetic energy of the plasma constituent. The substrate target distance can be adjusted to compensate for kinetic energy loss due to collision with gas molecules in the ambient. It should be noted that this might affect film quality due to deposition of droplets on the substrate. Often despite the non-equilibrium nature of the deposition the substrate is heated at high temperature to enable epitaxial film growth. While this works well for a majority of cation, those with low vapor pressure or sticking coefficient like Li, Na, Zn, Mg etc. need to be handled appropriately. This process is highly energetic even when compared to other non-equilibrium techniques like sputtering and evaporation. Hence, super-saturation occurs at the substrate during each pulse which can last for 10's of microseconds[149]. Depending on the deposition parameter the nucleation can occur as an island, layer by layer or a combination of the two at the substrate[150]. The different growth mechanisms are given in figure 2.2. The mechanism depends on the super saturation of the adatoms on the substrate, Kinetic energy of the species on the surface, stoichiometry, substrate defects, and bonding energy between the species and

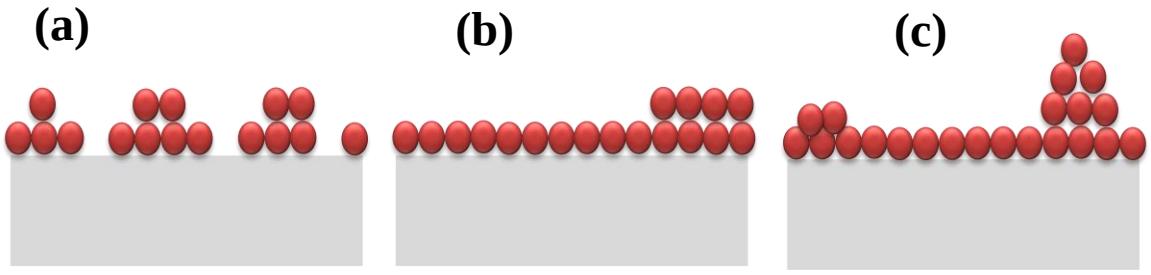

Figure 2.2. Schematic of different nucleation and growth mechanism, (a) island, (b) layer by layer, (c) mixed island and layer growth mechanisms.

substrate. A more in depth analysis of the capability of PLD systems can be found in literature [151]. A schematic of our pulsed laser deposition system is given in figure 2.3. It uses a KrF excimer laser (Lambda Physik Compex Pro 205, λ=248nm). The vacuum system consists of a dry scroll roughing pump and a turbo pump. A typical base pressure of 10^{-6} can be achieved and flow meters can be used to adjust partial pressure in the range 0 mTorr to 200mTorr. Laser fluence can be adjusted between 5 to 12 J/cm^2. A resistive substrate heater can be used to heat the samples up to 760 °C. The substrate target distance is adjustable in the range of 2.5 cm to 7 cm. Both commercial and custom built, in house targets can be used for the deposition, with the target holder supporting up to 6 rotating targets.

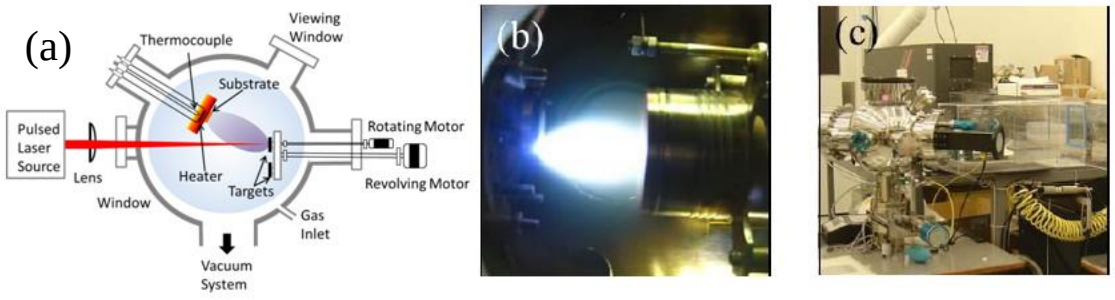

Figure 2.3. (a) Schematic of a PLD system, (b) a plume, (c) the PLD setup.

2.3 Sputter System

Sputter is by far the most popular PVD technique in the industry. Several schemes of this deposition system are employed such as, DC sputter, RF sputter, Reactive sputter, magnetron sputter etc. Of these magnetron system is always employed in all systems to improve ionization yield while reactive sputter involves introducing reactive gas during the deposition. Because of

this versatility a wide range of films like metals, oxides, nitrides, silicide etc. can be grown using this system[152]. A schematic of a sputter system is shown in figure 2.4 below. A high negative voltage is applied to the cathode. When an ambient gas is introduced in this high voltage region, electrons are stripped of its outer orbit. Argon is normally used for this due to its noble nature, ease of ionization, low stiction, and relatively low cost. The Ar^+ ion is attracted to the negatively biased target and triggers a cascade of collisions. The collision back sputters target material which is then deposited on the substrate. At the same time along with the target species, electrons are also ejected from the target. These electrons further ionize the argon gas. Most sputter systems utilize a magnetron setup. Permanent magnets placed behind the target to generate a magnetic field to exert force on the electrons to move along a helical path near the target. This greatly enhances the ionization and yield of the system[152].

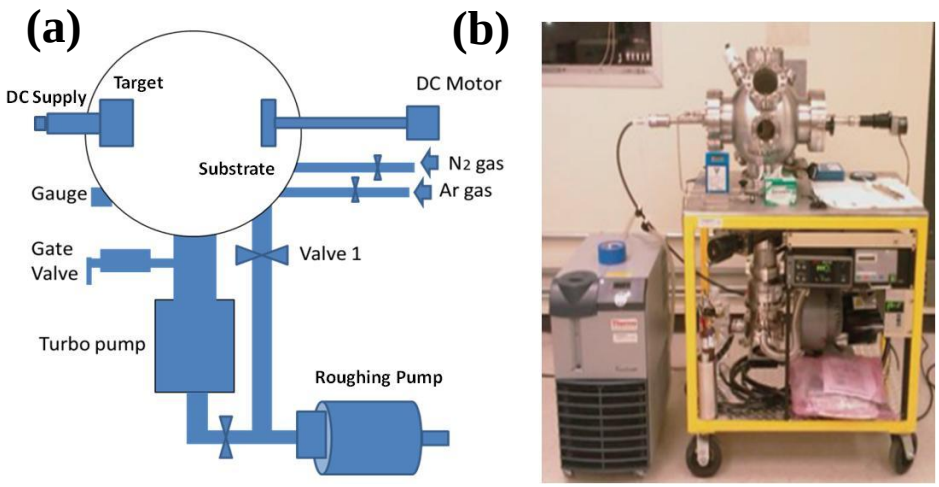

Figure 2.4.The sputter and vacuum pumping setup, (a) schematic and, (b) actual system used.

The DC sputter was used to deposit a gold buffer layer on the stainless steel substrate. Details of the recipe will be given in appropriate sections.

2.4 X-ray Diffraction (XRD)

X-ray diffraction is a popular technique to investigate the crystal structure of a material and is used to determine the primary phase, impurity phases, lattice parameter, texture, strain, grain size etc. of the sample. The material to be analyzed is irradiated by a X-ray generated using a cathode tube with a metal (usually copper) target. The crystal lattice of the sample acts like a diffraction grating, and the resultant pattern is measured by a detector of a known orientation. According to Braggs law,

$$n\lambda = 2dsin\theta$$

Where, n is an integer, λ is the characteristic wavelength of the X-ray, d is the d spacing between the x-rays and theta is the angle at which both the incident and diffracted beams are incident on the sample with respect to the normal. Because the incident and diffracted angles are the same, this setup is often referred to as the Bragg reflection[153].

This mechanism is shown in figure 2.5 below.

In this work x-ray diffraction was used primarily for phase identification and crystal lattice parameter (out of plane) measurement. The PANalytical Empyrean 2 system used for the measurements is equipped with independent drive shafts for the detector -source and a 3-axis chi phi z stage. This enables a wide range of thin film diffraction techniques including

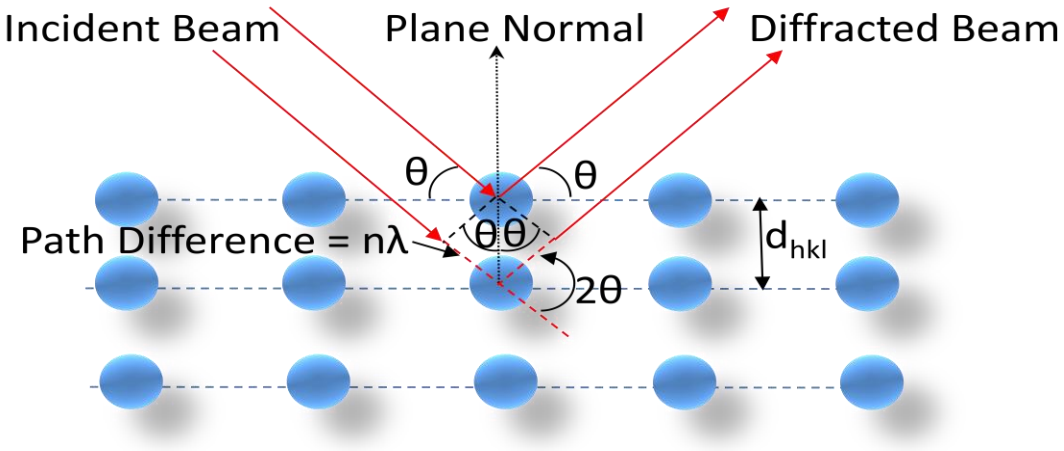

Figure 2.5. Illustration of a Bragg reflection occurring in a crystal lattice.

grazing incidence, pole figure, reciprocal space map, reflectivity etc. The X-ray diffraction setup is shown in figure 2.6 below. This work utilizes grazing incidence to better analyze the thin films. Grazing incidence uses a small offset for the source usually less than 3 degrees. This shallow angle allows for greater volume of interaction[154]. Simultaneously the theta arm scans the sample giving a more detailed diffraction pattern then the regular Bragg scan.

Figure 2.6.PANalytical Empyrean 2 diffraction system.

2.5 Wavelength Dispersive Spectroscopy (WDS)

WDS utilizes the characteristic X-ray generated by the sample when illuminated by a high intensity electron beam. Typically a 10 to 20 KV potential difference is applied between the gun and sample to bombard a spot with electrons and generate X-rays by individual elements which are then analyzed. These X-rays are directed towards an analytical crystal with specific lattice spacing. A WDS setup will often have multiple crystals to accommodate for all elements. However elements lighter than atomic number 5, cannot be measured by a WDS since the energy is too low. The sample and crystal are aligned so that the take-off angle is kept constant. Only X-rays that satisfy the Bragg's law is passed to the detector. Changing the position of crystal with respect to the sample changes

the d-spacing and hence the element identified. A typical WDS setup is illustrated in figure 2.6 below. The sample, crystal and detector must lie on the Rowland circle for all wavelengths of interest. Once the detector counts the X-ray intensity for each element, the

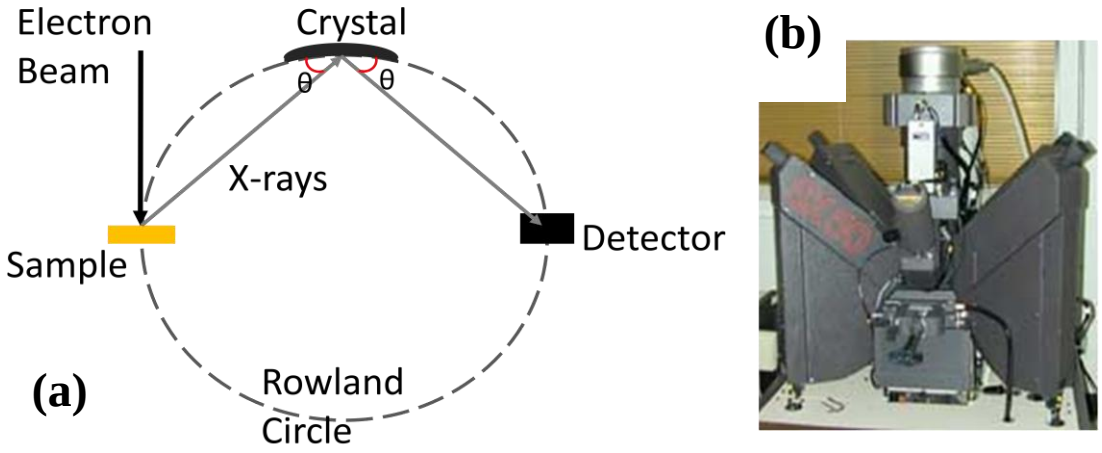

Figure 2.7. (a) Setup of a typical Johann geometry wavelength dispersive spectrometer showing the sample, crystal and detector, (b) system used for measurement.

data is compared to the counts obtained for standards containing known amount of those elements. This can be used to quantitatively measure the composition of the film. WDS is non destructive, can measure trace amount of elements and sue to the filtering action of the crystal can measure higher intensity without saturation. However, lighter elements like H, Li, Be , valence variation and isotopes of elements cannot be measured using a WDS[154].

2.6 Secondary Ion Mass Spectroscopy (SIMS)

A SIMS system uses a primary ion beam of oxygen (O2+ or O-), Cesium (Cs+) or Ar+ ions to bombard the sample. A duoplasmatron source is used to generate ions from gas source or dedicated high voltage setup is used to generate Cs from Cs chromate source. The primary beam is focused and directed using a combination of deflector plates, apertures and electronic lens. No specific sample preparation is required. The bombardment leads to secondary ion emission from the sample. A high voltage extraction or immersion lens is used to direct the secondary ions towards the ion energy analyzer. As the secondary ions pass through the energy analyzer the low energy ions are more strongly deflected. A movable energy slit is then used to select the segregated ions and pass it onto the mass analyzer. The mass analyzer utilizes a magnetic field that applies a perpendicular force on the ions. The mass analyzer can distinguish between ions with different energy and mass. In combination with the electrostatic ion analyzer, once segregated and analyzed by the mass spectrometer is passed through an electron multiplier and detector system to generate the final counts. A schematic describing the operation is shown in figure 2.8. A SIMS system can detect everything from light elements like Hydrogen to heavy ones like Uranium. The system has a high sensitivity (ppm to ppb) and can also detect isotopes. Rastering the secondary ions can be used to generate images as well. Some of the limitations of the systems include sputtering of molecules by the physical process which makes analysis difficult, high vacuum requirements and stringent standard requirements to attempt quantitative measurement[155, 156].

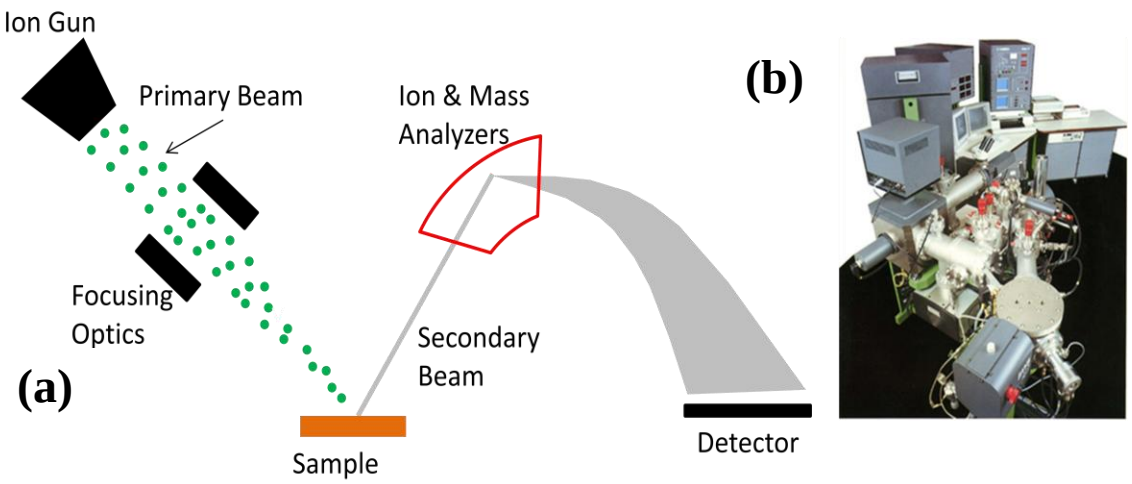

Figure 2.8. Schematic outlining components and operation of a secondary ion mass spectrometer.

2.7 Scanning Electron Microscopy (SEM)

The resolution ρ of optical microscopy is limited by the wavelength λ, index of refraction η and illumination of semi-angle α. The resolution is given by,

$$\rho = \frac{0.6\,\lambda}{\eta\,\sin(\alpha)}$$

Electrons based imaging offers significant improvement in resolution. Much smaller wavelength can be achieved due to the energy or voltage dependence of the electron beam. This relation can be shown using the following equation,

$$\lambda = \frac{h}{\sqrt{2m_o eV_o}}$$

Where, h is the Planck constant, m_o and e are the mass and charge of an electron and V is the applied voltage. The comparison between the various factors and its effect on resolution of the image in an optical and electron microscope is given in table below.

Table 2.1 Comparison of the critical parameters of optical and electron imaging

Parameter	**Light Microscope**	**Electron Microscope**
$\boldsymbol{\lambda}$	0.5 μm	0. 68 nm
$\boldsymbol{\eta}$	1.5 (Glass)	1 (Vacuum)
$\boldsymbol{\alpha}$	70^{o}	$\leq 1^{o}$
$\boldsymbol{\rho}$	0.21 μm	0.41 nm

A scanning electron microscope employs a focused electron beam to illuminate the sample surface. The electrons interact with the electric field of the nucleus-electron system in the sample leading to generation of secondary and backscattered electrons along with x-rays, auger electrons and cathode-luminescence. Secondary electrons are generated by the transfer of energy via inelastic collisions with electrons from the electron beam leading to ejection of electrons from the specimen atoms. The schematic of a typical SEM system is shown in figure 2.9 below. Many of the components and their purpose are similar to those in a TEM. These will be discussed in more details in the next section. SEM is used in this work primarily to investigate surface morphology (secondary electrons) and for rough estimation of phase distribution (back scattered electrons).

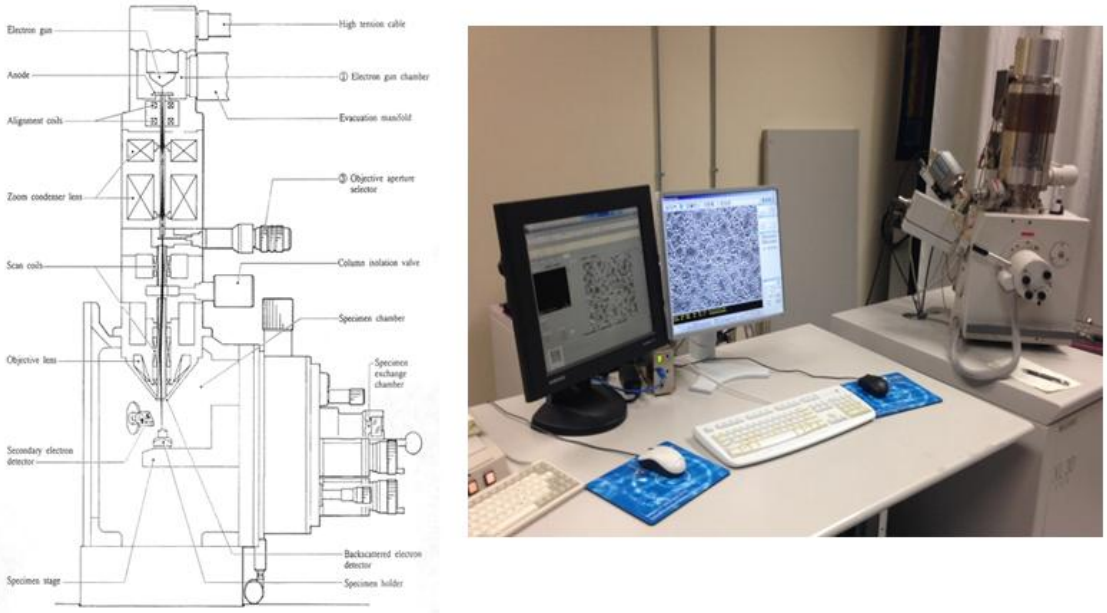

Figure 2.9. (a) Schematic of a SEM system, (b) a FEI QUANTA 600 FE-SEM.

2.8 Transmission Electron Microscopy (TEM)

Similar to an SEM, the TEM uses high energy electrons to obtain high resolution images of the specimen. TEM utilizes transmitted electrons as opposed to reflected electrons that are used in SEM. The transmitted electrons in a TEM can be classified as direct beam, coherent elastic and incoherent elastic and inelastic electrons. The particle nature defines elastic (no energy loss) and inelastic (energy loss) nature of the electron. The wave nature determines the coherency i.e. coherent (in phase) or non-coherent (out of phase) nature of the electron. Depending on the imaging method different or multiple components are used for the microscopy. A typical TEM setup is shown in figure 2.10 below.

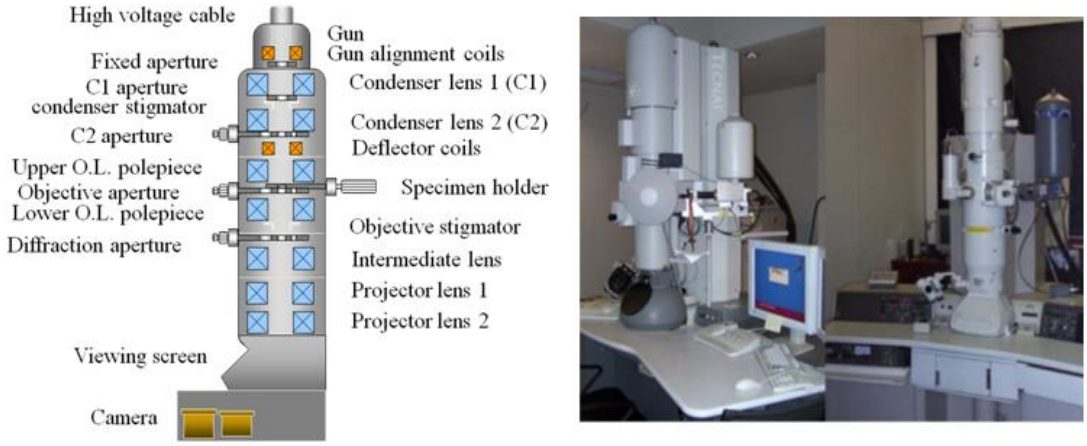

Figure 2.10. Schematic of a TEM Microscope showing major components of the system and the FEI Tecnai G2 F20 and JEOL JEM-2010 TEMs.

The electron source can be either thermionic guns where a filament is heated to high temperature tungsten (2600 K) or LaB_6 (1700 K) and controlled using a small bias voltage. A high accelerating voltage is then used to accelerate the electrons towards the first lens. Recently, TEM use cold field emission guns to generate highly focused and coherent beams. Typical energy spread and spot size of a FEG is 0.8 eV and 20 nm as opposed to W gun (3 eV, 60 μm) and LaB_6 (2 eV,5μm). The specimen holder can be top entry or side entry type. The latter is popular since it allows flexibility with sample rotation. Liquid nitrogen chilled cold blades are used to condense contaminants from the specimen. Condenser, objective and diffraction apertures are used to control beam size or select specific components of the beam. The lenses consist of a cylindrical core of easily magnetizable soft iron surrounded by coils. The magnetic field is generated by passing a current through this coil. The coil is normally

water cooled. The electrostatic and electromagnetic force on the electrons is given by the equations,

$$\overline{F_E} = q\bar{E}$$

$$\overline{F_B} = q[\bar{v}\ x\ \bar{B}]$$

Typically the condenser lens 1 is used to control beam size and condenser lens 2 is used to control brightness. The objective lens is used mainly to focus the image which is then magnified by the intermediate and projection lens. The intermediate lens is also used to select between imaging and diffraction mode. Lens defect or contamination causes astigmatism due to magnetic field asymmetry. Stigmator coils are used to correct this.

Phosphor screen and CCD cameras are used for observing and recording the images. For high resolution imaging (HRTEM) aberration corrected microscopes are used. Bright field imaging utilizes the central component of the transmitted electrons. For dark field imaging a particular diffraction spot is selected in diffraction mode and the beam is tilted to the spot. Dark field imaging mode is then used to get the corresponding image. These show higher contrast.

2.9 Thick Film Cathode Fabrication

The cathode slurry is prepared using the active material, binder, and conductive carbon. A wide range of active materials have been successfully used for thick film cathode fabrication in this work. The binder used was the Kureha 1100 pvdF and the conductive additive use was C45 and C65 carbon Black from Timcal. A Lindberg box furnace is used

for this. Depending on the desired ratio active material, binder and carbon black is weighed. Moisture is detrimental for battery performance as it reacts with fluorine in the salt to form hydrofluoric acid which erodes the electrodes. Hence the active powder and carbon black are preheated at 120 °C overnight in a furnace. NMP solvent is measured using a calibrated syringe and poured in the metal ball mill container. This is then heated at 90 °C at the PVDF is added to this and manually stirred. Metal balls are then added to this mixture and the container is closed. A five minute high energy ball milling is performed to homogenize this mixture. The active powder and carbon is then added to the mixture followed by 20 min ball mill. Additional solvent is added to get desired viscosity. A honey like viscosity is found ideal for the following processes.

An aluminum current collector is used for the cathode. The surface is cleaned using methanol wipe followed by NMP solvent clean. The surface is scratched using a paper wipe during the cleaning process. Roughening the Al foil surface improves the adhesion by increasing the contact area between the laminate and the current collector. Commercially, roughening of the metal foil surface is done using sanding, chemical etching, or electrolytically depositing Al onto the foil. Allow the NMP to evaporate before casting the electrode. Little methanol is spread on a flat glass plate and the Al foil is attached to the surface using this. The current collector must be spread extremely flat onto the glass surface since the objective is to cast very thin films on the foil. A doctor blade applicator height of 200 μm is used for the actual casting. The applicator is moved at a slow but continuous pace several times over the current collector. After the casting move the glass plate directly on the

heater and set it at 75 °C to bake out the NMP. Once the film is dry remove it from the heater. To completely remove the NMP solvent, heat it, at 120°C for 12 hours in the box furnace. This also removes residual water which can be detrimental to battery life. Also, residual NMP can lead to delimitation from the current collector. The dried film is next compressed to achieve desired porosity and improve current collector-film adhesion. A compact film is good for electronic conductivity, while porosity allows electrolyte penetration and hence improves ionic conductivity. Generally, a film compressed to about half its initial thickness was found to give optimum performance. The films can be compressed directly in sheet form (standard practice) using a calendaring setup or a hydraulic press. For lab scale work pre-cutting the cathode disk followed by pressing in a hydraulic press was found to give the desired result too. The different equipments used are shown in figure 2.11. The prepared electrode is either stored in the glove box or heated in a furnace at 90°C for 12 hours before transferring to the glove box for cell assembly. The glove box is maintained at 0.1 ppm H_2O and 0.1 ppm O_2. A hammer and punching tool is used to cut 1/2" cathodes and 9/16" Li anodes for half-cell testing.

Figure 2.11. (a) Low and high energy ball mill, (b) box furnace, (c) screen printing using doctor blasé applicator, (d) calendaring machine, e) manual punch.

2.10 Thin Film Cathode Fabrication

Thin film cathodes require a conducting substrate to enable assembly in a coin cell format. A stainless steel substrate was selected for this reason. The current collector size was standardized to 0.8 cm x 0.8 cm to enable 2032 coin cell assembly. Sheets of SS were cut using hydraulic sheet cutter in the mechanical workshop. These were then mounted on flat brass tabs using crystal bond and polished with sand paper with increasing grades ranging

from 320 to 1200. A final polish was done using alumina suspension of 3 and 1 μm particles. The substrate was then removed and cleaned with methanol and dried. Mirror finish substrates were obtained using this process. A gold buffer is deposited on the substrate to reduce Nickel and chrome diffusion into the cathode as well as to provide a textured substrate for film growth. The layer was deposited using a DC sputter system, details of which were discussed earlier. This was followed by the actual cathode material is deposited using the PLD system described earlier. The deposition process itself varied between experiments and will be outlined in detail in the relevant chapters.

2.11 Coin Cell Assembly

The coin cells are assembled inside the glove box. The glove box is a sealed box with an Argon atmosphere. The gas inside is continuously filtered to maintain the environment inside at 0.1 ppm H_2O and 0.1 ppm O_2 or better. This is necessary to prevent the Li metal and electrolytes from reacting with air or moisture. The setup is shown in figure 2.12 below. Nitrile gloves over glove box gloves when handling materials to avoid contamination.

The previously prepared 1/2" cathode is used. These are weighed before transferring into the glove box and appropriately labeled to identify them later. Li metal is used as anode for the

Figure 2.12. a) Glove box and, b) hydraulic crimp used for cell assembly.

half cells and is cut into 9/16'' discs. A hand held punch is used to cut the circular lithium electrodes out of lithium foil purchased from Alfa Aesar. These are flattened after punching to ensure uniform assembly. The separator polymer film is obtained from Celgard. The separator is cut into disc using the manual die sets. The die sets were custom designed using tool steel. The different components of the coin cell are shown in figure 2.12. To begin the actual assembly, the cathode is first placed into the bottom casing (positive casing) of the coin cell. During cell assembly care should be taken to avoid any contact with the cell wall, as this will short the cell. Also the electrodes should not be moved during assembly as the relative position of the anode and cathode might shift resulting incomplete overlap or might be pressed below O-ring of the negative casing. Use a syringe or dropper to slightly wet the cathode. This helps to improve the stiction of the separator with the cathode and also prevents air bubble trapping below the separator. A plastic or electrically insulated tweezers

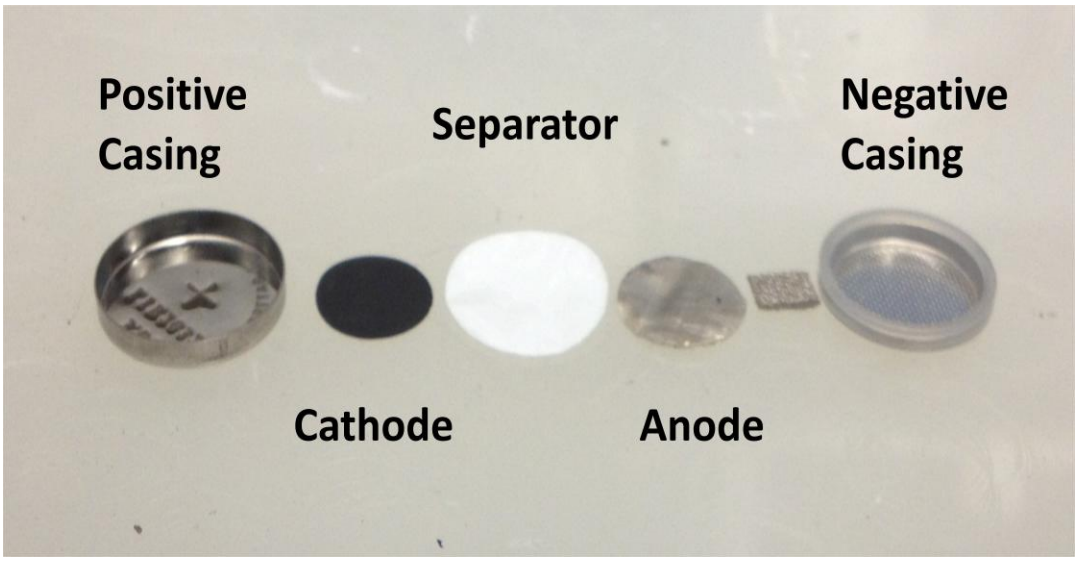

Figure 2.13. Components of the coin cell.

is used to center electrode within the metal casing. Center the separator on top of the electrode. Place one drop of electrolyte onto the separator using a syringe or dropper. Make sure that the electrolyte fully wets the separator. Wetted parts will appear transparent. Again using the plastic tweezers the Li anode was placed and centered the Li anode making continuous contact with the separator. A nickel foam is used as spring for the assembly. Center the spring on the Li foil. The wider part of the spring should be in contact with the Li anode. Additional electrolyte was then poured on the nickel foam till it is saturated. The negative casing is then placed and the pressed to close the cell assembly. Care is taken to ensure that all parts of the cell remain centered; including the top enclosure. The cell was then placed in the hydraulic crimp and sealed at around 750 psi. Excess residue is wiped clean and the coin cell is appropriately labeled.

2.12 Electrochemical Testing

2.12.1 Evaluation Metric

In order to understand the electrochemical testing a better understanding of the evaluation metrics is necessary. The different important parameters for electrochemical evaluation of a material are listed below.

2.12.1.1 Capacity

During charging Li is removed from the cathode and current flows into the battery while during discharge Li is inserted into the cathode accompanied by current flow out of the battery. The cumulative current flowing into the battery is called charge capacity and the net current outflow is termed discharge capacity. Traditionally it is normalized wither with respect to weight or volume. The specific capacity of the battery is given in $mAhg^{-1}$ while the volumetric capacity is given in $mAh.cm^{-3}$. Higher specific capacity means lower weight, while higher volumetric capacity leads to more compact batteries. While these apply to both thin film and thick film batteries, another unit is commonly used for thin film electrodes. The battery capacity can be normalized in terms of surface area ($\mu A.cm^{-2}$) or surface area and thickness ($\mu A.cm^{-2}.\mu m$). The latter is equivalent to volumetric capacity. The latter is very appropriate for solid state battery, which is known for a small foot print. A typical charge discharge curve for one of our $Li(Ni_{0.5}Mn_{0.3}Co_{0.2})O_2$ thin film cathode is shown in the figure below. The red plot is the discharge curve, while the black curve plots the charging curve vs

voltage. The “II” curve shows a discharge curve with two distinct plateaus. The flat slope area or plateaus correspond to the redox voltages of the electrode, in this case the $LiMn^2O^4$. The Mn^{2+}/Mn^{3+} transformation depending on its lattice location gives rise to the distinct plateaus.

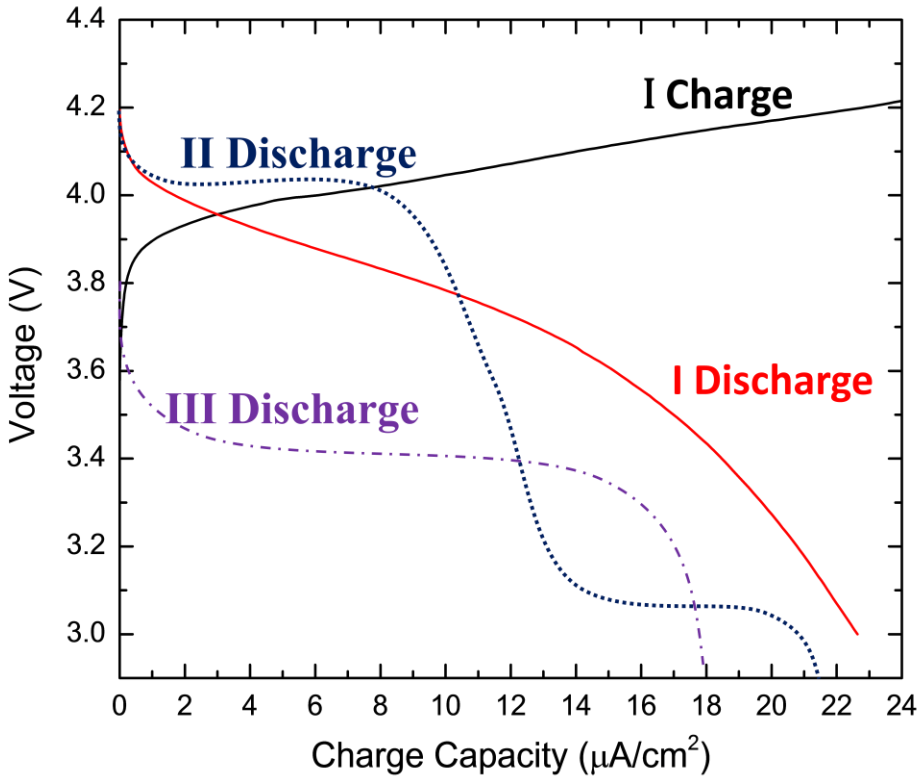

Figure 2.14.Charge discharge curve for different thin film cathode measured vs Li anode
The “III” discharge curve is typical of $LiFePO_4$ cathodes which unlike layered cathodes give a flat single stage discharge.

2.12.1.2 Power

Simply put power corresponds to how fast the battery can charge or discharge. In formal terms it gives the energy supplied by the battery per unit time. The power (P) can be expressed in terms of current (i) and voltage (V) as,

$$P = V\ X\ i$$

The structural and kinetic limitation of the electrode and electrolyte limit the charge transfer at higher rates. Thus if current drawn from the battery exceeds the kinetics of the rate limiting mechanism in the battery, the power drops due to polarization. The rate capability can be measured by charging and discharging the battery at different current levels or C-rate. All batteries show lower capacity at higher c-rates, however lower this loss, betters the power delivery capability of the battery. A typical rate capability study we conducted is shown in the figure 2.15. As expected at higher C-rates the capacity falls significantly with a 40 mAh/g loss at 1.2 C compared to 0.2 C.

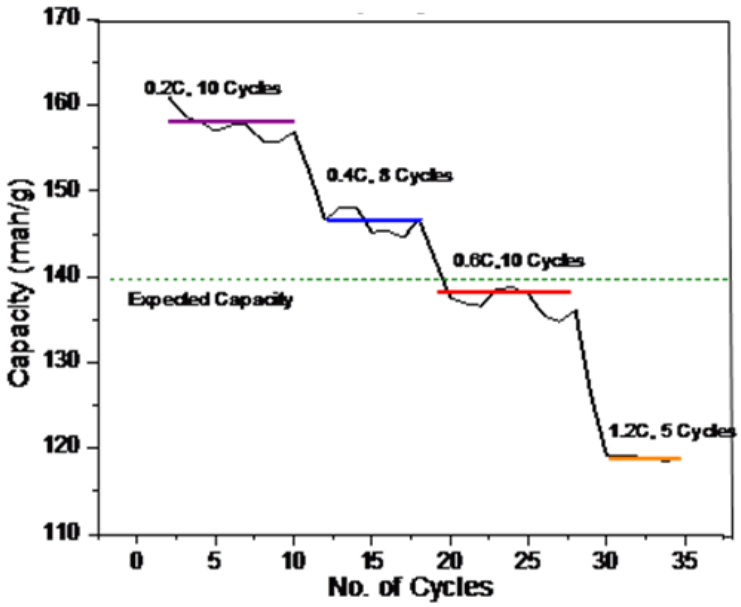

Figure 2.15. Power capability of a typical thick film battery measured at different discharge capacity.

2.12.1.3 Cycle Life

This is a measure of the life cycle of a battery. Upon cycling the capacity of a battery reduces gradually or rapidly depending on the constituent material properties. Structural and phase changes, side reactions and passivation layers lead to irreversible capacity loss. Commercial batteries are designed to last for over 2000 cycles with acceptable capacity deterioration. A cyclability result for one of our initial study is shown in the figure 2.16 below. Thus energy density corresponds to total distance the vehicle can travel on a single charge, while the power density correspond to how fast the vehicle can accelerate. Different existing and next generation energy storage solutions are plotted in this Ragone plot.

Amongst these Li ion gives the highest performance while being available in a commercially viable form.

2.12.2 Open Circuit Voltage

The open circuit voltage (OCV) is the simplest electrochemical test and can be measured using a simple millimeter. It is the voltage measured between the electrodes when the system is in equilibrium and no charge flow is occurring. This is directly related to the Gibbs free energy. This voltage is a quick and useful tool to evaluate the state of the electrodes, internal short, and initial solid electrolyte interface (SEI) reaction. OCV measured over the life cycle of the battery gives useful information about degradation of the electrodes.

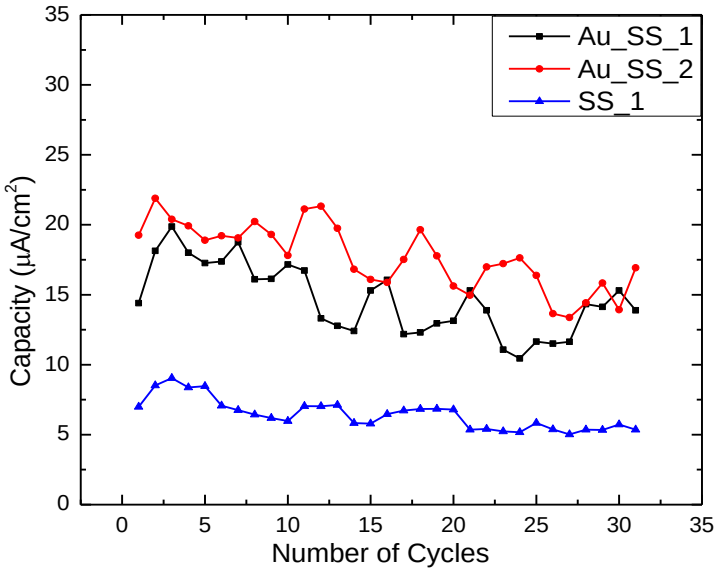

Figure 2.16. Cyclability of different thin film batteries measured over 30 cycles.

A regular fluke portable multimeter was used at various stages of battery testing to monitor OCV for all cells.

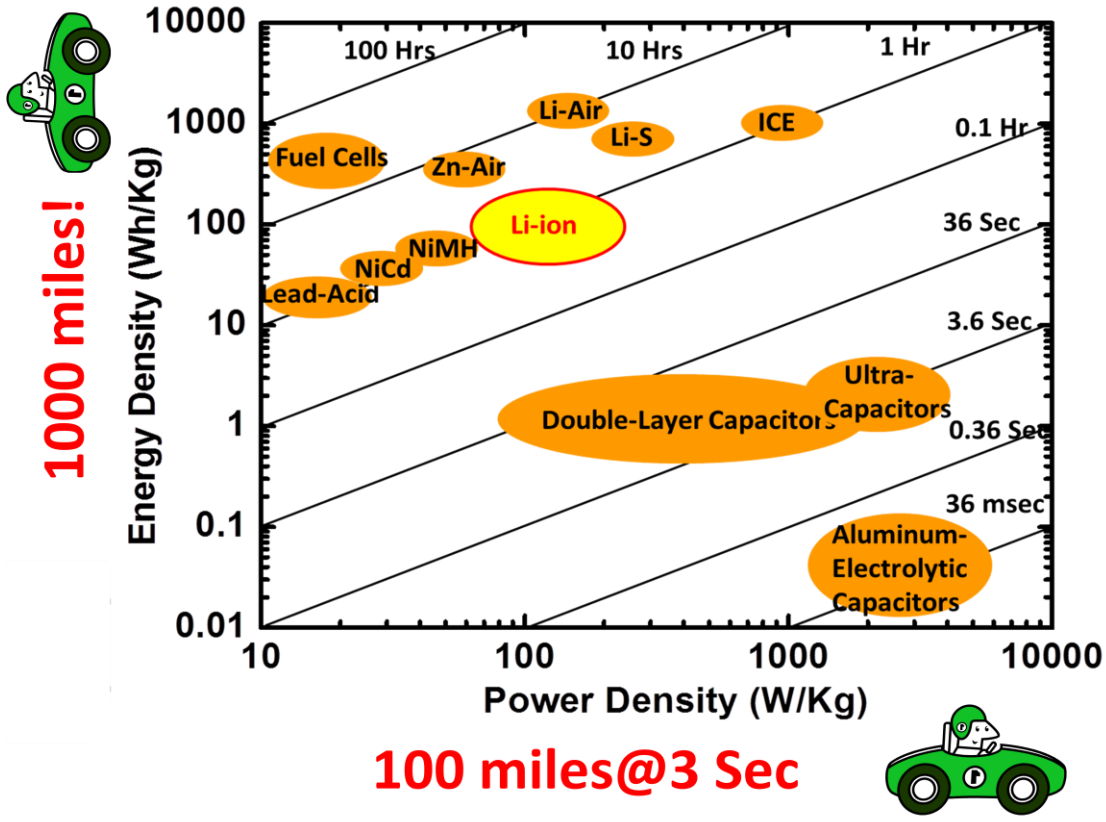

Figure 2.17. Schematic comparing different energy storage technologies.

2.12.3 Cyclic Voltammetry

A sweeping voltage at a constant scan rate is applied to the battery and the resultant current is measured. This is repeated to charge and discharge the cell and the anodic and cathodic current is measured. The current vs voltage curve provides information about the

redox reaction and can be thought of as the electrochemical equivalent of x-ray diffraction. The potential corresponding to current peaks gives information about the cation undergoing redox reaction to contribute towards the capacity of the cathode. Varying the sweep rate and plotting the peak currents for the different scan rates is useful in evaluating the diffusion rate of the Li ion in the battery. The difference between the cathodic and anodic peak can be interpreted for information regarding the reversibility of the electrochemical reaction.

2.12.4 Galvanostatic Charging

Galvanostatic charging or constant current charging is the most common test carried out for the batteries. A constant current is applied to the battery and the voltage and capacity of the battery is monitored. This can be repeated for charging and discharging the cell by reversing the applied voltage alternately. The discharge capacity at the end of each cycle gives the discharge capacity vs number of cycles. This can be used to evaluate the columbic efficiency, life cycle etc. for the cell. Also a dQ/dV curve can be plotted for a given cycle. The differential capacity curve can be used like the cyclic voltametry curve to identify the voltages at which reactions occur. The important difference from cyclic voltammetry is that the over potential in this case is constant. In CV very low sweep rates are required to obtain low or constant over potential. Thus differential capacity curve can give better information about reaction voltages.Figure 2.17 shows capacity of different energy storage technologies.

2.12.5 Potentiostatic Charging

Potentiostatic or constant voltage is a relatively simple method. In galvonostatic charging supplies a constant stream of charge to the electrode. Since the electronic and ionic conductivity of the external components (current collector for electrons and electrolyte for ions) is much higher, there is an inevitable charge build up at the surface. Thus there is a polarization problem and at higher voltage there is a possibility that the surface voltage might exceed the electrode voltage and hence damage the electrode. Under these circumstances, charging using the constant current method initially and constant voltage toward the end can give optimal capacity. Also a potential step method can be used to charge the cell for the entire cycle by applying voltage in increasing steps and allowing the electrodes to charge. This method can be used to measure open circuit voltage at different state of charge and also differential capacity curve and diffusion rates.

2.12.6 AC Impedance Spectroscopy

AC impedance spectroscopy utilizes alternating current to measure complex impedance of the battery. When an AC voltage is applied to a complex impedance system, the current through the system has a phase difference. This can be represented as,

$$V(t) = V_m \, sin\,(\omega t)$$

$$I(t) = I_m \, . \sin(\omega t - \theta)$$

The voltage and current can be separated into real and imaginary components and the corresponding impedance can be calculated. A Nyquist plot can be obtained by plotting the real impedance versus the imaginary resistance. Different components like resistance (R), Capacitance (C) , Inductance (L), series and parallel RC circuits etc., have different

characteristic graphs. Thus a Nyquist plot for a cell can be used to model the battery and identify the different mechanisms and components of impedance in the cell.

CHAPTER III

HIGHLY TEXTURED THIN FILM $Li(Ni_{0.5}Mn_{0.3}Co_{0.2})O_2$ CATHODES*

3.1 Overview

Epitaxial and highly textured $Li(Ni_xMn_yCo_{1-x-y})O_2$ thin film cathodes are deposited by an one-step, high temperature pulsed laser deposition technique. Structural characterization using X-ray diffraction, transmission electron microscopy and selected area electron diffraction (SAED) reveals highly textured film along (003). The best film quality has been achieved at high temperature, with temperature as high as 750℃. Different substrates and buffer layers have been investigated and $Li(Ni_{0.5}Mn_{0.3}Co_{0.2})O_2$ (NMC) on stainless steel with a thin Au-buffer layer gives the best film quality. The NMC thin film cathodes give a high capacity of $167mAhg^{-1}$ and $125mAhg^{-1}$ at 0.1C and 0.5 C, respectively. In addition, the cyclic voltammetry and charge discharge curves obtained after different cycles indicate good electrochemical stability with capacity retention of 89% after 100 cycles at 0.5 C. The electrochemical characteristics are correlated to the microstructure of the film and the effects of texture, grain size and density are discussed.

---

*This chapter is reprinted with permission from "Highly textured $Li(Ni_{0.5}Mn_{0.3}Co_{0.2})O_2$ thin films on stainless steel as cathode for lithium-ion battery", C. Jacob, T . Lynch, A.Chen, J.Jian, H.Wang, J. Power Sources 241 (2013) 410. Copyright © Elsevier 2013

3.2 Introduction

Thin film cathode research has been extensively pursued towards the development of solid state battery [157-161]. Thin film cathodes have also been proven to be a useful tool for investigating the properties of the intrinsic material.$LiCoO_2$ is by far the most popular and well researched material amongst transitional metal oxides for lithium ion batteries[162-164]. However it suffers several shortcomings including poor stability, inability to extract all the lithium ions and the high cost and toxicity of cobalt[65, 165]. One of the most successful strategies to overcome some of these limitations, is the partial substitution of Co with Ni and Mn to form $Li(Ni_xMn_yCo_{1-x-y})O_2$. Ohzuku and Makimura[166], and Lu and Dahn[167] first reported this in 2001. $Li(Ni_xMn_yCo_{1-x-y})O_2$ has a structure similar to $LiCoO_2$, α-$NaFeO_2$ type structure and $R\bar{3}m$ space group. Ohzuku and co-workers reported a capacity of 150mAhg^{-1} for $Li(Co_{1/3}Ni_{1/3}Mn_{1/3})O_2$cell cycled between 2.5 V and 4.2V.There is a renewed interest in transition metal oxides, especially multi-cation Ni, Mn and Co based oxides with the introduction of high capacity transition metal oxide composite [109, 168-170] and core shell structure[171, 172].Thin film batteries can be very useful in exploring such novel materials both for fundamental research and solid state batteries.

Thin film cathode fabrication has been explored over the last two decades [100, 173, 174], primarily using Radio Frequency (RF) sputter[100, 173, 175-180] and pulsed laser deposition (PLD)[180-189]. However, very little work has been done on thin film $Li(Ni_xMn_yCo_{1-x-y})O_2$ cathodes. A detailed examination of the film growth could lead to a better understanding of its crystal structure and offer great opportunity to identify stable and

high performance cathode material. Traditionally high quality films and novel material synthesis requires high temperature deposition. However the only reports in literature for $Li(Ni_xMn_yCo_{1-x-y})O_2$ thin film are those with room temperature (RT) deposition followed by post anneal. Also ambiguity remains about the benefits of the high temperature post annealing. Deng and others observed poor cyclability and adhesion for films annealed above 500^oC[179]. Ding and co-workers reported a RT RF sputtering of $Li(Co_{1/3}Ni_{1/3}Mn_{1/3})O_2$ followed by a post anneal step at 700^oC, however their results is not conclusive as the cyclability is also limited by the interfacial stability of the solid electrolyte used in the experiment[177]. Xie et al. reported good initial capacity for films annealed at 600 ℃for RF sputtered film, but did not investigate cycling capability of the cathodes[90]. Also post annealing of films in all these cases resulted in either amorphous or randomly oriented polycrystalline films. Low temperature amorphous or polycrystalline films can be useful for flexible batteries specially coupled with solid electrolyte like lithium phosphorous oxynitride (LiPON). However, unlike crystalline metal oxide films, which have good conductivity due to sharing of the metal cations between adjacent unit cells, amorphous films tend to impede electron flow [190].A PLD with in-situ heating allows for a one step process for fabricating thin film cathodes. Furthermore, in addition to cost benefits, it gives the capability to control film microstructure by varying oxygen partial pressure, deposition frequency, and temperature and deposition energy. In this work, one step, high temperature deposition of $Li(Ni_{0.5}Mn_{0.3}Co_{0.2})O_2$(NMC)thin film and its cycling performance is reported. The effects of

different substrates and buffer layers on the film crystallography and the electrochemical characteristics of the batteries are investigated.

3.3 Experimental

NMC thin film cathodes were prepared by PLD using a Lambda Physik KrF excimer laser with a wavelength of 248nm and energy of 180mJ-400mJ. The laser energy of 200mJ corresponding to a laser energy density of 6 $Jcm^{-2}$was applied to achieve high quality deposition of NMC film. Commercial NMC powder (MTI; average particle size of 10μm and Brunauer–Emmett–Teller (BET) surface area of 0.2-0.6 m^2g^{-1}) was used for all experiments. To compensate the possible loss of lithium during target calcination and laser ablation during deposition, 20% excess Li was used for the target. The target was prepared by mixing stoichiometric powder with 20% Li_2CO_3 powder (99.99% Alfa Asear). The mixture was first heated at 350 ℃, pressed into a pellet and sintered at 900 ℃ for 12 hours in air. Different substrates were used including Silicon (111), stainless steel (SS) and c-cut sapphire (0001). In addition buffer layer coating of gold (Au) and titanium nitride (TiN) were also used. These will be referred to as Au-SS and TiN-SS respectively. A standard DC sputter system was used for the Au buffer, while TiN was deposited using PLD, at room temperature. The substrate temperature was varied from room temperature to 750℃ during PLD deposition to explore the optimum deposition temperature. Conventional thick film cathodes were also prepared using doctor blade method. A slurry containing 84% NMC, 8% Carbon C45 (Timcal) and 8% polyvinylidene fluoride,(Kureha KF100 binder) and *N*-methyl-2-

pyrrolidinone (NMP) solvent was mixed using ball milling. A doctor blade applicator was then used to coat the slurry on an aluminum current collector followed by drying at 90℃ for 12 hours in air. The film was then pressed and cut into circular cathode discs. The cathode had an average loading of 8 mg cm^{-2}.

The structure and crystallinity of the PLD and doctor blade films were investigated using aBrukerD8 powder X-ray diffractometer. Transmission electron microscopy (TEM) was done using a FEI Tecnai G2 F20 TEM. Coin cells were assembled with Lithium metal anode and EC:DEC:1M$LiPF_6$ (BASF) electrolyte in an argon glove box with well controlled oxygen and moisture levels (O_2<0.1ppm and H_2O<0.1ppm).Galvanostatic charge–discharge cycling tests were carried out between 3V and 4.2V at a constant current density of 22$\mu$$Acm^{-2}$ corresponding to 0.5C, and cyclic voltammetry curves were obtained using a voltage ramp rate of 100$\mu$$Vs^{-1}$ both using the Arbin BTS2000 battery testing system. Impedance spectra were measured on a Gamry Series G 300 setup.

3.4 Results and Discussion

The θ-2θ X-ray diffraction scans of the films deposited on different substrates are given in figure 3.1. Bare stainless steel and silicon give weak (003) peaks. The Au-SS sample shows strong NMC(003) peak and a strong Au(111) peak. The single crystal *c*-cut sapphire displays strong (003), (006) and (009) NMC peaks. The film quality is strongly influenced by the laser fluence and substrate temperature. However since the SS and Si ones did not show a strong(003) peak it is obvious that there is a substrate dependence of the film quality. It is

possible that the Au- buffer layer helps due to its inert nature or acts like a diffusion barrier between stainless steel and the NMC film. Also the lattice match between Au and NMC can be a contributing factor. Yet another possibility is the surface quality of the substrate. To further investigate the role of buffer layer as diffusion barrier, titanium nitride (TiN) coating, a known diffusion barrier was tested. However the TiN buffer sample did not show significant improvement in film crystallinity over the others. This suggests that diffusion barrier may not be the dominating factor. Alternatives to gold buffer are attractive due to obvious cost benefits. Further work on Tin and other alternate buffers is currently underway. Si(111) (3.136Å) and NMC(2.867Å) have a much larger mismatch compared to the 0.62% mismatch between Au and NMC.

This directly correlates to the observed film quality. It was initially expected that high temperature should enable textured film irrespective of the substrate. It is possible that the roughness of the surface of the bare substrate also adversely affected the film quality. The textured nature of the Au-coated substrate likely offsets this as well. Figure 3.2 shows films deposited on Au-SS substrates at different temperatures. At deposition temperatures below 500 ℃ no significant film peaks were observed.

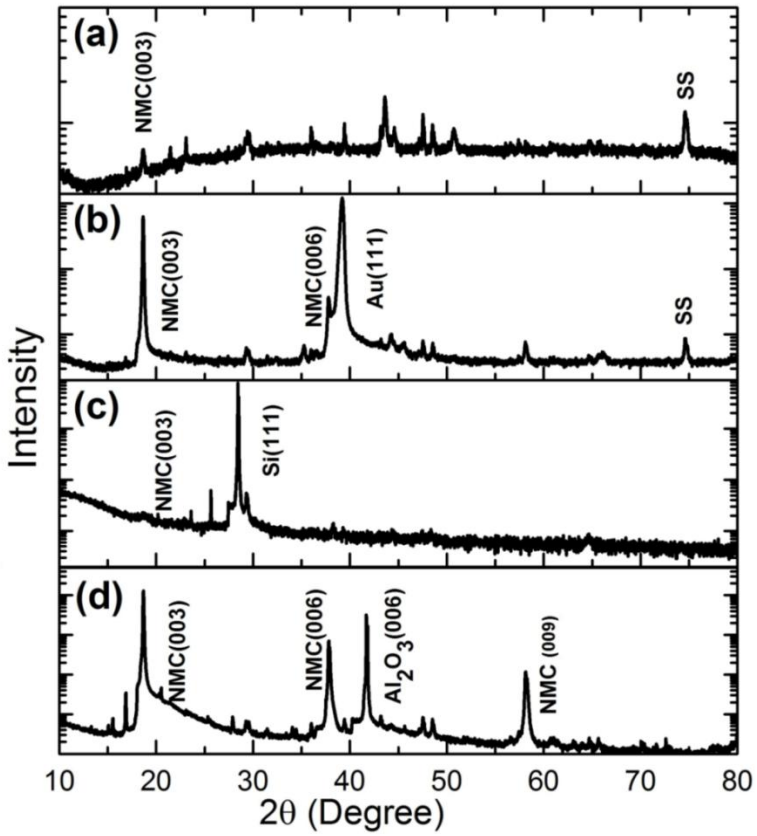

Figure 3.1. XRD pattern of PLD deposited thin film of $Li(Ni_{0.5}Mn_{0.3}Co_{0.2})O_2$, (a) stainless steel, (b) gold coated stainless steel, (c) silicon (111), (d) c-cut sapphire.

The (003) peaks starts to show up as the deposition temperature increases to 650 ℃ and is very strong for films deposited at 750 ℃. This is expected as high density, epitaxial film growth can be achieved at high temperatures. In case of $LiCoO_2$, temperatures above 700 ℃ have been reported to cause impurity phases. However no such impurity phase is observed for NMC in this study. This can be attributed to the stability of the structure which prevents the formation of Co_3O_4 or any other secondary phases.

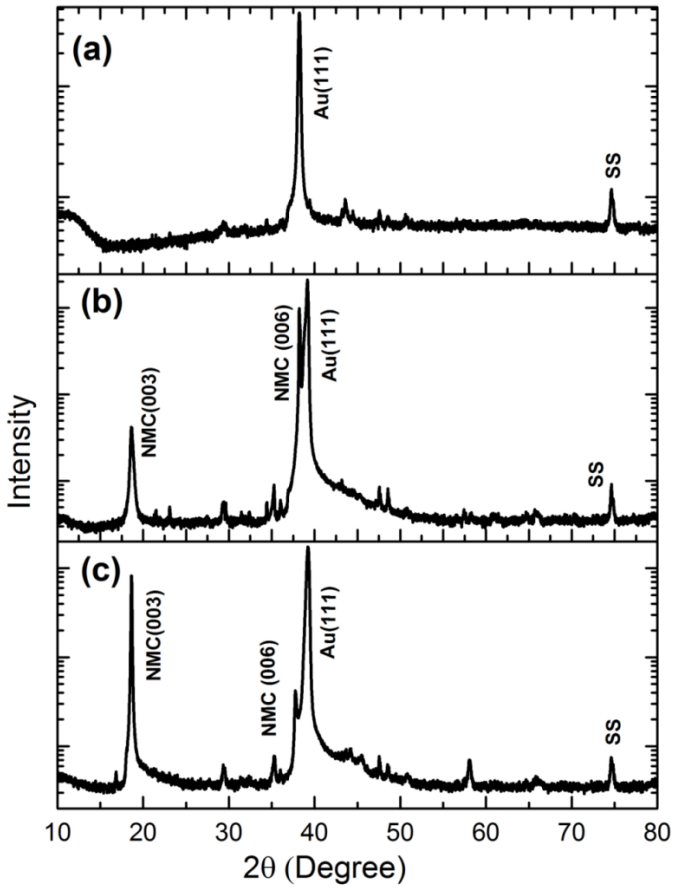

Figure 3.2. XRD pattern of NMC film deposited on Au-SS substrate at, a) 450 ^{o}C, b) 650 ^{o}C and, c) 750 ^{o}C.

Another phenomenon observed is the reduction of the (006) peak intensity with increase in temperature. A strong (003) peak and weak (006) peak is very typical for PLD thin films of this class of material [184].An inexpensive conducting substrate is preferred for actual electrochemical tests while high quality single crystal substrate is desirable for initial studies and film analysis. To compare the quality of the film on the Au-SS and sapphire

substrate, the full width half maxima (FWHM) of the substrate peak and (003) peaks on both substrates is compared. The FWHM of the NMC(003) peak on the Au-SS substrate and sapphire is 0.123 degree and 0.096 degree respectively. This clearly indicates that high quality film has been achieved on the Au-SS substrate.

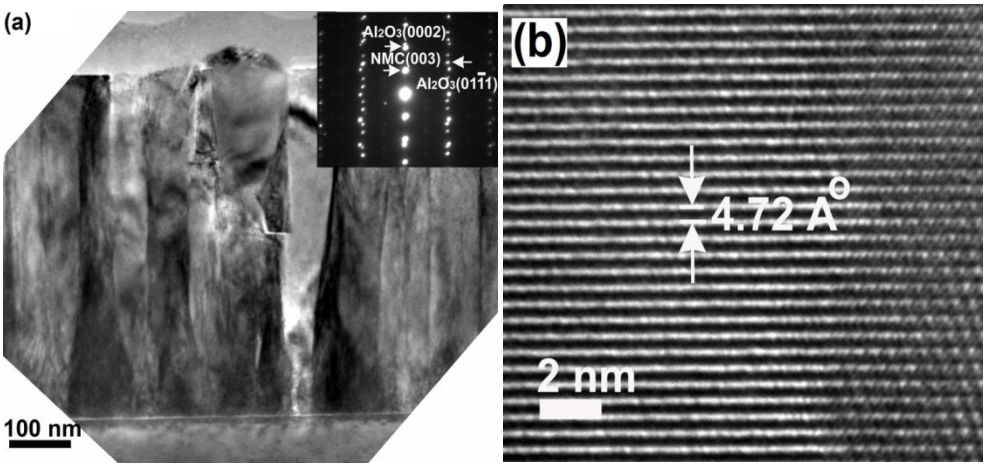

Figure 3.3. TEM image of NMC thin film on c-cut sapphire substrate: (a) low magnification image showing columnar NMC film. Inset shows the diffraction pattern of NMC film with Sapphire substrate, (b) high magnification image of NMC film.

The TEM images and the corresponding selected area electron diffraction (SAED) pattern of the film on sapphire substrate from $[0\bar{1}10]$ zone axis are shown in figure 3.3. The film has grown epitaxially on sapphire (0001) substrate. The film thickness is approximately 450nm. The spacing between successive planes corresponds to approximately 4.72Å which is in agreement with XRD results. The *d*-spacing of (006) estimated from the SAED is 2.39Å and matches with the theoretical models. The SAED analysis gives the lattice parameters

of *a*= 2.83±0.01Åand *c*= 14.06±0.01Å,which is slightly lower than bulk value reported in literature[191].In addition the distinguished diffraction dots observed for NMC film indicate high quality epitaxial growth of NMC film. The epitaxial relationship between the film and the substrates are determined to be $(0002)\,Al_2O_3$// (0003)NMC and $[0\bar{1}10]\,Al_2O_3$//$[\bar{1}\bar{2}10]$ NMC.

The charge-discharge curves after different numbers of cycles for the NMC film on Au-SS substrates are shown in figure 3.4 (a). After the initial cycling the relative change in capacity in subsequent cycles reduces. This is probably due to the progressive stabilization of the cathode and decrease in side reactions. While EC:DEC 1M $LiPF_6$ is stable up to 4.3V, there could still be partial decomposition of electrolyte or reaction at the cathode surface at lower voltages. This could be partially mitigated by a thin coating of solid electrolyte like LiPON, which is a much more stable electrolyte. A sharper discharge curve is seen in figure 3.4, than observed for conventional doctor blade films prepared using the same active material. This can be possibly attributed to the polarization at the cathode. Bouwman and co-workers attributed the polarization and faster discharge rate to the (003) orientation of the film, typical of PLD films. The cyclic voltammetry curve for the cells at different cycling stages is given in figure 3.4 (b). It clearly shows a broad anodic peak at 3.85V and a broad cathodic peak at 3.5 V corresponding to Ni^{2+}/Ni^{4+} redox process, after the 1^{st} cycle. The CV curve for a thick film battery, prepared using the conventional doctor blade method is shown in the inset.

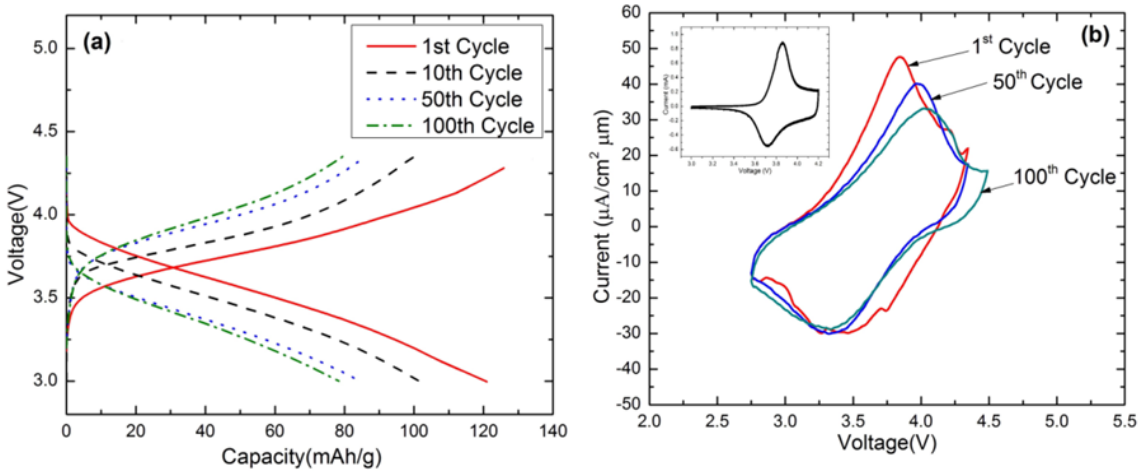

Figure 3.4. a) Charge discharge curve and b) cyclic voltammetry of NMC thin film cathode. Inset shows cyclic voltammetry curve of thick film NMC cathode.

The anodic and cathodic peaks at 3.85 V and 3.7 V are sharper compared to the thin film samples. The shift seen in the cathodic peak is believed to be a result of the fast scan rate. Limited by our measurement capability, the larger scan rates could result in the electrochemical reactions occurring at the surface rather than in the bulk of the film. Another possible contributing factor to the shift as well as the peak broadening is the polarization due to the large grain size and a lack of conductive additives [40].After the 50th and 100th cycle the anodic peak shifts to 3.95V and 4V respectively, while the cathodic peak position does not show a significant shift. Usually, an increase in peak separation is associated with a decrease in reversibility. However it seems that the increased peak separation occurs due

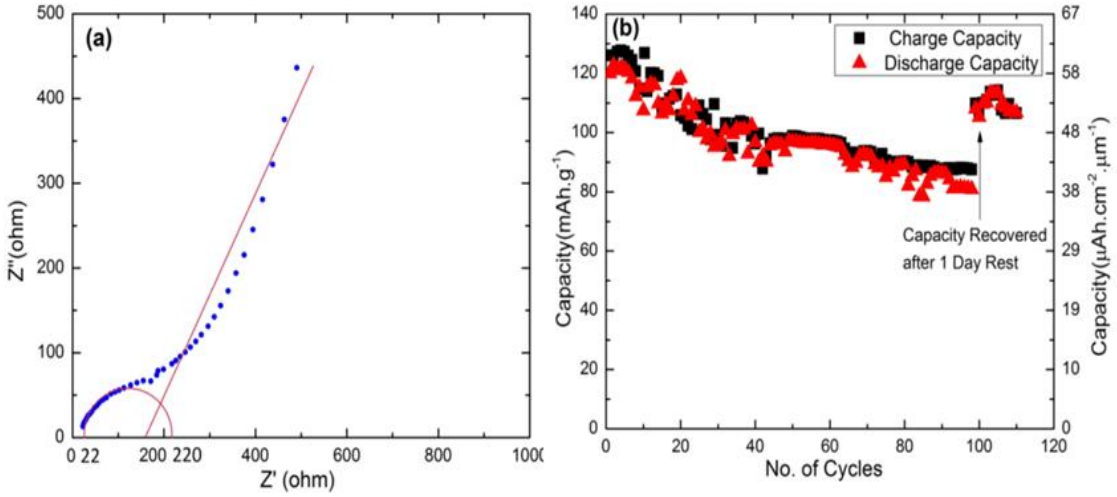

Figure 3.5. (a) Electrochemical impedance spectroscopy of NMC thin film on Au-SS substrates,(b) charge-discharge capacity of NMC thin film cathode on Au-SS substrate as a function of cycle number.

to a combination of the same factors that also resulted in peak shifts discussed earlier. In addition a reduction in the current amplitude of the anodic peak can be seen. This is most likely due to increase in surface resistance of the cathode with increased cycling. However, consistent to the data seen in individual cycles in figure 3.4 (a), the difference between the peak amplitudes reduces progressively with cycling, indicating a good structural stability during the intercalation and de-intercalation of Li ions. Figure 3.5(a) gives a typical electrochemical impedance spectroscopy (EIS) measurement of the cell. The solution resistance and ohmic contact resistance is around 22 Ω while the charge transfer resistance of 275 Ω.The low ohmic resistance is probably due to good adhesion. Kim and coworkers reported that (003) oriented film in $LiCoO_2$ exhibit the least volume expansion during cycling at high voltages as compared to randomly oriented powder samples [192]. NMC has

a similar crystal structure. If the volume expansion during cycling is limited the corresponding increase in interfacial stress between the current collector and cathode film during cycling will be reduced. Since the film substrate adhesion during cycling is excellent, the cycling performance of the battery is improved. The diffusion or Warburg resistance dominates the impedance in the mid and low frequency region. Thin films deposited on Au-SS substrate have a capacity of 125 mAh g^{-1} at 0.5C. This is higher than the values reported in low temperature annealed films at similar charge discharge rate [179]. Furthermore, the high density of the film improves internal adhesion of the film and consequently improves the cycle life of the battery. The charge-discharge capacity of NMC thin film cathodes using Au-SS substrate is shown in figure 3.5(b). The capacity is lower than that reported for bulk batteries. The conductive additives in bulk batteries improve electron transfer, while the film porosity allows better contact with the electrolyte, facilitating improved Li ion transfer. However, thin film cathode do not have inactive mass like carbon and binder and more importantly allows study of material properties independent of such external factors. The cathodes demonstrate good reversibility with 72% capacity retention at 0.5 C after continuous cycling for 100 cycles. Also after resting for a day the cell recovered its capacity significantly. This indicates to a partial reversible capacity loss, probably due to an increase in the polarization of the cathode. The batteries retained 89% of the initial capacity at 0.5C rate.

3.5 Conclusion

NMC films were prepared using a one-step high temperature pulsed laser deposition without a separate post-anneal step. The film quality displays strong substrate dependence and Au-buffered stainless steel substrate is found to be an ideal substrate. The textured nature of the Au- buffer layer and good lattice match between Au and NMC contribute to the high quality NMC film growth. TEM and XRD confirm the highly textured and epitaxial quality of the film. The cyclic voltammetry results show peak shifts due to polarization but this does not adversely affect the cycling capacity of the film. The thin film NMC cathode demonstrated an initial capacity of125mAhg^{-1} at 0.5C and retained 89% capacity after 100 cycles. The high cyclability is attributed to the good adhesion between the film and substrate as well as the internal adhesion of the high density film. This work demonstrates the high quality film directly grown by PLD at high temperature without the need for additional post-annealing. This method can be applied to the investigation of more complex cathode structure and composite films for solid state batteries.

CHAPTER IV

ELECTROCHEMICAL AND STRUCTURAL EFFECTS OF IN-SITU Li_2O EXTRACTION FROM Li_2MnO_3 FOR Li-ION BATTERIES*

4.1 Overview

Li_2MnO_3 is an attractive cathode material due to its low cost, non-toxicity and potentially high capacity. However, its electrochemical inactivity, poor electronic conductivity and uncertainty about underlying mechanism have limited its development. In this work, an in-situ technique for extraction of Li and O during deposition of the thin film cathode is developed to investigate structural and electrochemical effects in a controlled fashion. MnO_2 has been observed in samples with severe O and Li deficiency (capacity of 115 mAh g^{-1}), while Li_2MnO_3 cathodes with slightly excess O and Li (capacity of 225 mAh g^{-1}) can be synthesized by tuning growth conditions appropriately. Formation of MnO_2 phase, especially in Li and O deficient structures, could be a possible reason for irreversible capacity loss in Li_2MnO_3 related materials. Further investigation into stoichiometric and microstructure variations enabled by this technique allows rapid investigation of Li_2MnO_3 as well as other Li-rich composites.

---

*This chapter is reprinted with permission from "Electrochemical and structural effects of In-situ Li_2O extraction from Li_2MnO_3 for Li-ion batteries", C.Jacob, J.Jian, Q.Su, S.Verkhoturov, R.Guillemette and H. Wang, ACS applied mat. & inter.,7,4, (2015), 2433.

4.2 Introduction

Ever since they were first commercialized in 1991, Li ion batteries have been widely popular due to its high energy storage density. While recent advances have increased the capacity of anodes dramatically, the cathode continues to be constrained by capacity, cost and environmental concerns[193].The capacity for most cathode materials is limited to 140 – 170 mAh g^{-1}, while some of the elements like Co (in $LiCoO_2$), Ni (in $LiNiCoMnO_2$) and etc., are expensive and toxic. As alternatives, manganese-based cathode materials like $LiMnO_2$,[194] $LiMn_2O_4$,[195] Li_2MnO_3,[196] etc., have been explored owing to their low cost and environmentally benign nature. However, $LiMnO_2$ and $LiMn_2O_4$ are significantly limited by their capacity and stability issues. Li_2MnO_3 has a high theoretical capacity of 459 mAh g^{-1} and has been used as a component in Li-rich cathode with a demonstrated capacity of around 300 mAh g^{-1}[197]. Despite its great potential, Li_2MnO_3 requires pre-activation by acid etching [197] or high voltage charging[198]. This activation is attributed to stoichiometric variation and associated phase changes. However, Li_2MnO_3-based cathodes are limited by poor cycle life, rate capability and oxygen generation[199]. Rana and co-workers attributed the poor cycling life to repeated stress on Li_2MnO_3 lattice structure due to proton exchange[200]. Thus Li_2O removal by both acid etching and high voltage charging may be playing a role in structural degradation. Lee proposed that Mn occupies Li vacancies in a delithiated state[201]. So, it is plausible that excess Mn plays a role in cathode performance. It was also reported that Li ion dynamics can be tuned by changes in stoichiometry in Li_2TiO_3[202].Fehr et al., reported that excess Li vacancies facilitate Li diffusion in Li_2TiO_3[203]. This approach may also prove advantageous for improving the

performance of Li_2MnO_3 based cathodes. Clearly, a detailed stoichiometry variation study is needed.

In the past, such attempts have been mostly focused on either elaborate chemical synthesis methods to introduce small stoichiometry changes,[204] or theoretical modeling to better understand underlying processes[201]. To our knowledge, there is no prior report on wide range stoichiometric variation for this material. We have previously shown that thin film cathodes can be useful in analyzing various aspects of battery performance[205, 206]. In this work we demonstrate a novel, fast and flexible thin film, pulsed laser deposition (PLD) based approach to directly synthesize $Li_{2\pm x}Mn_yO_{3\pm y}$ with a wide range of stoichiometry by controlling Li and O content of the cathode during deposition. Such wide stoichiometry control is achieved by controlling the deposition parameter during the thin film deposition process. This method can be employed to improve the stability of the layered structure and ionic conductivity. Furthermore, the possibility of simultaneous removal of lithium and oxygen has been explored to probe electrochemically activation and irreversible capacity loss in Li_2MnO_3. Two extreme cases can be created, one with severe Li and O deficiency, thus effectively getting a Mn excess phase, and the other with excess Li. The structural and compositional observations are correlated with corresponding electrochemical properties.

4.3 Experimental

Li_2MnO_3 target was prepared by mixing Li_2MnO_3 (Pfaltz& Bauer) with Li_2CO_3 (Alfa Aesar) in desired molar ratio. The powder was mixed using a high energy ball mill for 1 hour and decomposed in a flowing Ar atmosphere at 350 °C. The resultant powder was then

pressed into a pellet and annealed at600 °C. The film was deposited using a PLD system using a 248 nm KrF laser source with a laser fluence of 1 J cm^{-2} at 10 Hz. The target substrate distance was set at 4 cm for all deposition. A polished stainless steel substrate with a gold coating was used for electrochemical testing and c-cut sapphire

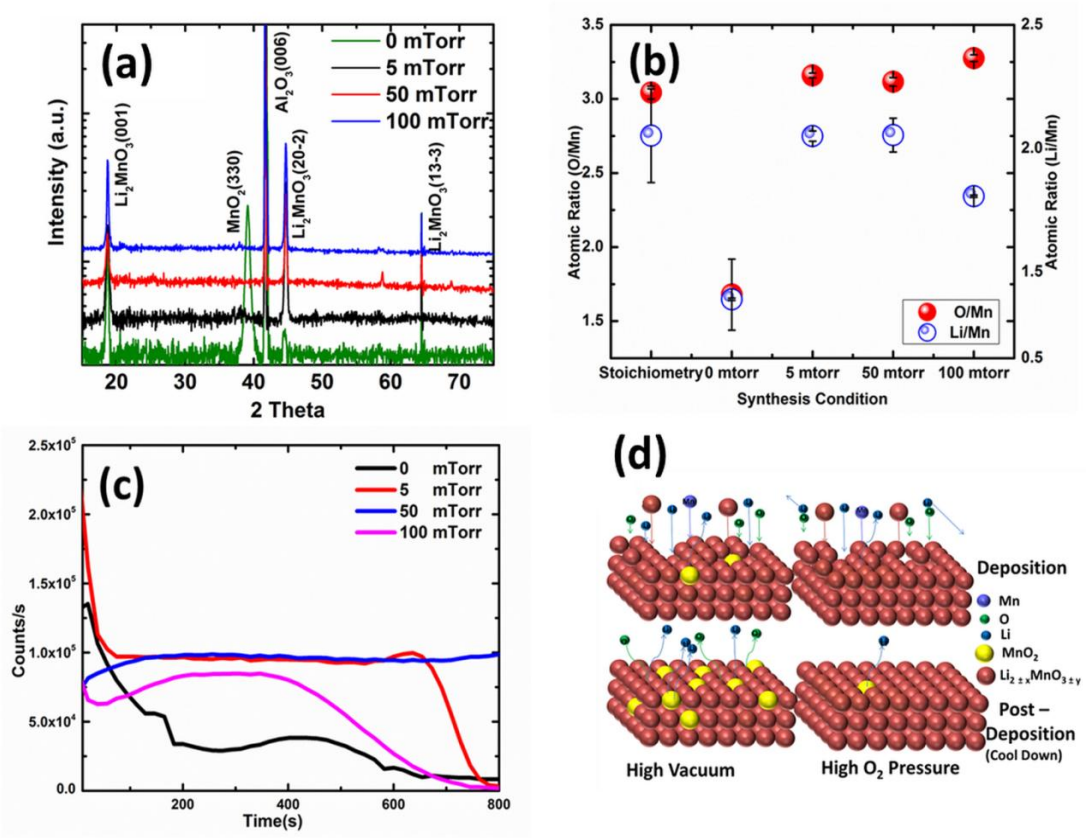

Figure 4.1. (a) X-ray diffraction patterns of films deposited under different oxygen partial pressure, (b) wavelength dispersive spectroscopy results indicating O/Mn and Li/Mn ratio stoichiometric pellets and films deposited under different oxygen partial pressure, (c) secondary ion mass spectroscopy results for Li content for the different cathode films, 9d) model depicting deposition process and resulting stoichiometry for high vacuum and high oxygen partial pressure conditions.

Table 4.1Deposition condition for different cathodes

Oxygen Partial Pressure	Post Deposition Pressure
0 mTorr	0 Torr
5 mTorr	10 Torr
50 mTorr	50 Torr
100 mTorr	500 Torr

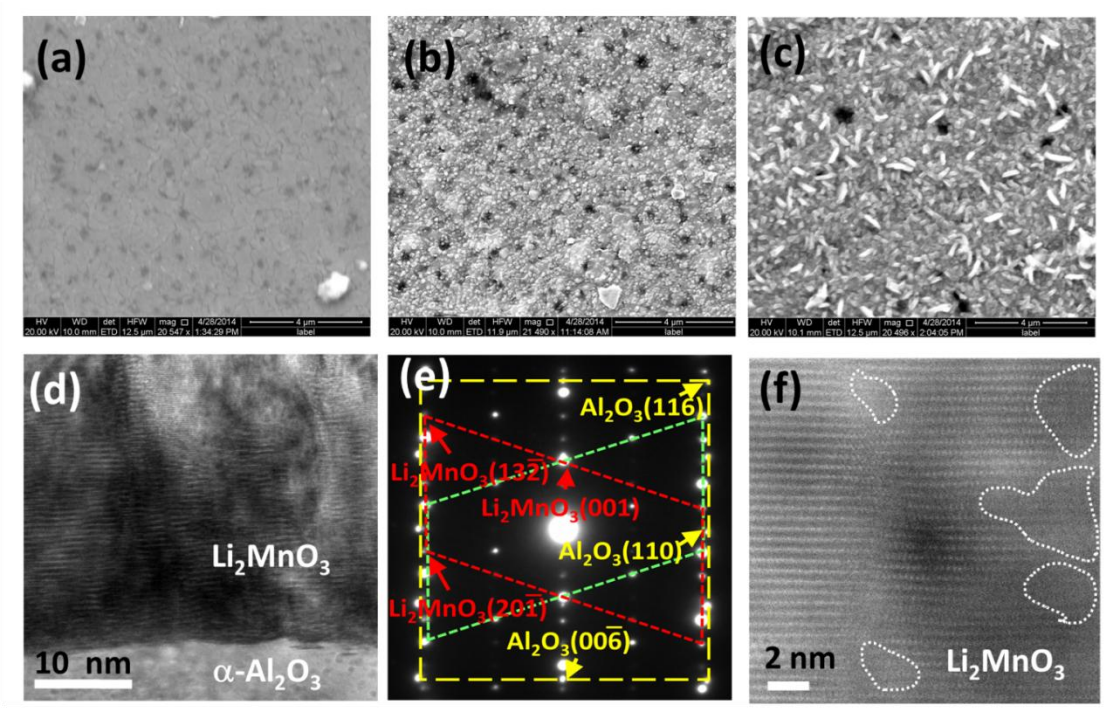

Figure 4.2.(a-c) SEM images for films deposited under vacuum, 50 mTorr and 100 mTorr in order, (d)TEM image of 50 mTorr sample, (e) SAED pattern for film deposited on c-cut sapphire substrate at 50 mTorr O partial pressure, (f) STEM image of sample deposited on c-cut sapphire at 50 mTorr partial pressure.

substrates were used for TEM and XRD. The films were deposited at 750 °C under different oxygen partial pressure ranging from 0 mTorr to 100 mTorr. The samples were cooled down at approximately 10 °C min-1 under different partial oxygen pressures. The details of the deposition condition are listed in table 1. XRD measurements were done on a PANalytical

Empyrean 2 XRD system using a Cu Kα source with a ½ ° fixed diffraction slit and a 1mm receiver slit. SEM images were obtained on a FEI Quanta 600 field emission scanning electron microscope and TEM and STEM images were taken on a FEI Tecnai G2 F20 ST field emission system and an aberration-corrected FEI Titan microscope equipped with a high brightness Schottky-field emission electron source operated at 300 kV respectively. Wavelength dispersive spectroscopy to quantify composition of the films was carried out on a Cameca SX50 electron microprobe. An accelerating voltage of 15 KV and beam current of 20 nA was used for the measurements. Since Li cannot be measured directly a difference method was employed to estimate Li content. The composition was further verified with secondary ion mass spectrometry (SIMS) using a Cameca IMS 4f ion microprobe. CR2032 coin cells were assembled in an Ar atmosphere (Glove Box, O2 0.1ppm, H_2O 0.1 ppm) with Li metal anode and Celgard 2400 separator. An ethylene carbonate: dimethyl carbonate (EC: DMC 1:2 by volume) with 1 M $LiPF_6$ salt was used as electrolyte. Cyclic voltammetry (50 μV s-1) and battery cycling was carried out on an Arbin BT2000 system.

4.4 Results and Discussion

The X-Ray Diffraction (XRD) patterns in figure 4.1a present films grown on sapphire substrates under different conditions as summarized in table 1. XRD data show that the films have a monoclinic structure and the peaks were indexed according to a *C*2/m space group structure, Li_2MnO_3 (ICDD # 202639). The films deposited on the c-cut sapphire substrates are highly textured with predominantly 3 preferred orientations. All samples show a strong (001) peak indicating that one of the preferred orientations is along the c-axis for the

monoclinic phase. In addition all the samples grown under partial oxygen pressure show a stronger $(20\bar{2})$peak. The similarity between the diffraction patterns of the films deposited under 5, 50 and 100 mTorr suggests a stronger dependence on the post deposition conditions rather than the partial pressure during deposition. Based on the diffraction pattern the 50 mtorr sample has lattice parameters a = 4.89 Å, b = 8.44 Å and c = 5.05 Å, for β = 90.4°. This matches well with other reports in literature[207]. The vacuum-deposited sample shows an additional peak around 39° which is likely to be either α-MnO_2 (330) (JCPDS 44-0141) or γ-MnO_2 (222), (JCPDS 44-0992). In the absence of further data it is difficult to determine the exact structure of the phase. The broad peak indicates the poor crystallinity of the MnO_2, which might be due to co-existence of the two MnO_2 phases. This will be discussed further in context of other measurements.

A detailed wavelength dispersive spectroscopy (WDS) study was conducted to determine compositional variation and the data for films on stainless steel substrates are summarized in the plot in figure 4.1b. The stoichiometric sample was a pellet prepared using as-received powder to provide a baseline to compare with the deposited samples. Compared to the stoichiometric case, the oxygen to manganese (O/Mn) ratio in the vacuum sample is determined to be around 1.75. On the other hand the 100 mTorr sample has an O/Mn ratio of about 3.25. Clearly, a large variation in oxygen content has been achieved under different deposition conditions.

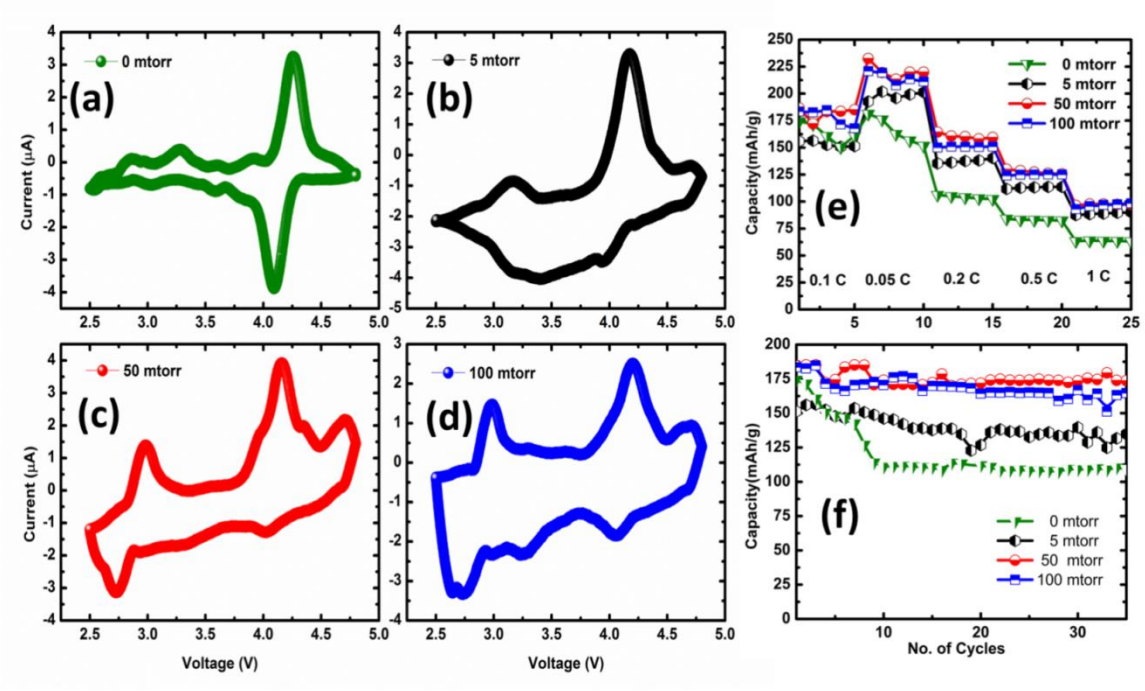

Figure 4.3. (a-d) Cyclic voltammetry obtained for films deposited at 0, 5, 50 and 100 mTorr respectively, (e) rate capability and, (d) cycling performance of films deposited under different conditions.

However, the amount of Li cannot be measured directly with WDS and therefore was calculated by comparing the difference. The Li to Mn (Li:Mn) ratio plot shows that the vacuum and the 100 mTorr samples are both Li deficient. To enable direct measurement of Li concentration, secondary ion mass spectrometry (SIMS) was further conducted to confirm the Li content in the films and the results are shown in figure 4.1c. The SIMS data is mostly consistent with the WDS result and the 6Li profile clearly shows that the 0 mTorr sample contains the least Li followed by the 100 mTorr sample. Similar to the WDS result, the Li contents of the 5 mTorr and 50 mTorr samples are comparable. Under high vacuum, two mechanisms could result in Li deficiency. A lack of oxygen may cause the formation of

metallic lithium or Li_2O during film deposition. This combined with a substrate temperature of 750 °C and high vacuum could cause desorption of Li/Li_2O from the film. Under high oxygen partial pressure, the light Li ions get deflected by ambient oxygen molecules resulting in an oxygen deficient film. The film deposition process can be depicted by the following reaction.

$$Li_2MnO_3 \rightarrow xLi_2O \uparrow + yMnO_2 + (1 - xy)Li_2MnO_3$$

Where, Li_2O represents the various Li and O loss mechanisms described above. The mechanism resulting in stoichiometry variations is illustrated in schematic drawings in figure 4.1d. The 5 mtorr and 50 mtorr samples are closer to the stoichiometric case. The composition data in combination with XRD results show that small stoichiometric variations lead to either Li and/or O deficient or rich films. Furthermore, a large reduction in any of the elements leads to the formation of secondary phases, such as MnO_2 observed in the vacuum case. The presence of MnO_2 further confirms that the removal of Li_2O was achieved as initially proposed. Further work on fine tuning of the process to achieve intermediate stoichiometry between the vacuum and 5 mTorr samples is currently underway.

The effect of deposition parameters on surface morphology was investigated using scanning electron microscopy (SEM) and is shown in figure 4.2 (a) vacuum, (b) 50 mTorr, and (c) 100 mTorr. The surface of the vacuum sample (2a) is quite smooth. Under higher partial pressures the surface shows nano-plate like and/or sphere like features. For example, the 50 mtorr sample (2b) shows nano-spherical grains which naturally maximize surface area. While the grain morphology will affect properties, for thin films the phase and stoichiometry of the film should dominate electrochemical performance.

Transmission electron microscopy (TEM) micrographs of these samples were taken to investigate the microstructure properties further. The results for the 50 mTorr sample are shown in figure 4.2d. The TEM images show that the film is dense with large grains. The obvious lattice fringes indicate obvious c-axis oriented film in this area on a c-cut sapphire substrate. Figure 4.2e shows the selected area electron diffraction (SAED) to confirm the phase and crystallinity of the samples. Based on the diffraction pattern, three sets of diffractions can be identified. The two sets of symmetric diffraction patterns, marked in red and green, are indexed as Li_2MnO_3 and the sapphire diffraction pattern is marked in yellow. No obvious impurity phases were identified in the diffraction pattern in this area. Obviously, Li_2MnO_3 (001) planes are parallel to the sapphire (006) planes and the film shows good crystallinity, evident from the distinguished diffraction dots. Scanning transmission electron microscopy (STEM) images were also taken to resolve chemical disorder in the film. STEM under high angle annular dark field mode (HAADF) is also called Z-contrast where the image contrast is proportional to the atomic number Z. The image of the corresponding film (2f) shows some disordered structure with amorphous-like regions, possibly due to the presence of oxygen vacancies. STEM images indicate that the film composition is not uniform and localized defects are present even in the 50 mTorr samples.

The cyclic voltammetry results for the different cathodes are plotted in figure 4.3a-d after an initial cycle, to evaluate the effect of deposition conditions on electrochemical performance. All batteries show a redox peak pair around 4.2 V with oxidation peak at 4.2 V and the corresponding reduction peak at 4.1 V. This is significantly lower than the standard peak associated with irreversible oxygen loss[208]. Moreover, the small gap in the oxidation

and reduction potentials indicates that the associated redox pair is highly reversible. This is likely associated with Mn ions with different activation energies due to valence or atomic position in the crystal as compared to the redox pair observed around 3 V. In fact this is very similar to the redox pair at 4.1 V attributed to a 2-step extraction of Li reported by M.H.Rossouw et al., in $LiMn_2O_4$.[209].The cathodes synthesized at higher partial pressures show a secondary oxidation-reduction pair at 3 V and 2.75 V. This peak is generally attributed to Mn ion after a layer-to-spinel phase transformation[210]. The additional pair is likely to contribute to a higher capacity for films deposited under higher partial pressures. Increased partial pressure clearly results in stronger redox peak around 3 V. It is surprising as this peak is generally indicative of the activation of this cathode material, which in turn is normally associated with Li_2O removal. This aspect is further discussed in context of structural data below. Nevertheless, very limited cyclic voltammetry result is available in literature for Li_2MnO_3. These data confirm the importance of the 3 V redox reactions for good performance of the batteries to be seen in the following section.

Figure 4.3e shows the charge discharge capacity of the different cathodes vs Li anode when cycled between 2.5 V and 4.5 V at different c-rates. The cathode films deposited at 50 mTorr show the highest capacity, with a discharge capacity of 225 mAh/g at 0.05 C which corresponds to extraction of 0.98 Li per formula. This is close to, but slightly higher than the capacity of the 100 mTorr films. Figure 4.4f shows cycling capability of the different cathodes at 0.1 C. The 50 and 100 mTorr samples show good cycling stability. The capacity and cycle life obtained for the 50 mTorr sample are better than those reported by several groups for Li_2MnO_3 cathodes. [199],[204],[211] The improved capacity is likely

attributed to non-stoichiometry induced defects as reported previously[199]. It is interesting that defects were observed locally even in samples with a slight excess of oxygen. The high density of local defects observed in the STEM images may also be responsible for improved ion dynamics addressing one of the key limitations of Li_2MnO_3 cathodes[203].

This preliminary study has demonstrated that it is possible to design a wide range of stoichiometric derivatives of the native Li_2MnO_3 with the proposed thin film growth technique. We believe that the formation of MnO_2 is consistent with extreme Li and O deficiency, and is result of two different processes. It has been widely reported that a spinel-like phase formation occurs during the activation process driven by Li_2O extraction [201, 212]. Lithium deficiency in the Li layer promotes Mn ions from the transition metal layer to occupy some of these sites. This leads to formation of a spinel-like electrochemically active phase. Further extraction of Li_2O as simulated by the vacuum sample in this work leads to formation of the spinel λ-MnO2 phase. The layered Li_2MnO_3, that is not converted to the spinel-like activated phase during the deposition convert to α- MnO_2 due to Li and O loss. Both these mechanisms are consistent with experimental acid etching results reported by Shao-Horn and co-workers[212]. To the best of our knowledge this is the first report on the formation of MnO_2 with in-situ extraction of Li_2O. α-MnO_2 suffers severe structural degradation upon lithiation during electrochemical cycling[213]. This likely contributed to the poor cycling performance of the 0 mTorr sample. In fact the capacity obtained after cycling in this work agrees well with results reported in literature for α-MnO_2[214]. We had shown in our previous work that in Li-rich chemistries cathodes with nano-domains of Li_2MnO_3 perform better than those with much smaller and uniform distribution of Li_2MnO_3

in the $LiMO_2$ matrix. It is conceivable that better Li mobility in the latter hastens the formation of MnO_2 resulting in the poor performance observed. The good performance of the 100 mTorr sample is partly due to the use of Li anode in the test cells, which compensates for Li deficiency during initial cycling. As shown in the 50 mTorr case, defects can form even in samples without oxygen deficiency. A possible way to achieve this effect in bulk synthesis process would be employing low temperature synthesis techniques. While traditionally electrochemical activity in Li_2MnO_3 has been linked to oxygen defects, in other Mn-based cathodes oxygen deficiency has been linked with capacity decay[215]. In this context, electrochemical activity in samples with slight oxygen excess could be promising. In fact one of the proposed techniques to stabilize α-MnO_2 cathodes is to use lithia-stabilized MnO_2[214]. Fine tuning Li_2O extraction to directly synthesize the "activated" Li_2MnO_3 phase formation should be theoretically possible. Such further investigation would be useful to study various aspects like pre-activation, role of proton exchange and detailed mechanism resulting in the irreversible capacity loss.

4.5 Conclusion

In summary, we successfully demonstrated the synthesis of Li_2MnO_3 with a wide range of stoichiometries by selectively removing Li and O in-situ with a simple thin film deposition process. A large reduction in Li and O content leads to formation of MnO_2 phase that gave a discharge capacity of 112mAh g-1 after 30 cycles. The formation of MnO_2 is a possible factor in the poor cycling capability of Li_2MnO_3 based cathodes. Cathodes with a slight excess of Li and O deposited at 50 mTorr of oxygen partial pressure, showed localized

defects and gave an excellent capacity of 225 mAh g-1 at 0.05 C. The results present a likely reason for poor performance of some Li-rich cathodes. This thin film cathode growth technique can be applied to adjust the Li and O contents of the film independently to investigate various important mechanisms, including Li_2MnO_3 pre-activation, modifying film kinetics, and investigating phase transformation like monoclinic to spinel phases.

CHAPTER V

A NEW APPROACH TO INVESTIGATE Li_2MnO_3 AND $Li(Ni_{0.5}Mn_{0.3}CO_{0.2})O_2$ MIXED PHASE CATHODE MATERIALS*

5.1 Overview

In this work, cathodes consisting of a Mn rich electrochemically inactive Li_2MnO_3 phase and a $Li(Ni_{0.5}Mn_{0.3}Co_{0.2})O_2$ (NMC) phase are processed by pulsed laser deposition (PLD). Different from the traditional bulk / powder synthesis approach, pure materials of the two phases are either uniformly integrated by co-deposition of the two phases or deposited sequentially as layered structure, to emulate Li-rich mixed phase cathode materials. A high deposition temperature, 750 °C, was used to grow the films on *c*-cut sapphire and stainless steel substrates. The films either in a random form or in a more controlled multilayer-type, both show excellent film quality. The multilayer composite films show superior capacity, cycling and rate capabilities with a capacity of 293mAh g^{-1} at 0.05C. This method gives much better control of the Mn content of the cathode, phase purity and combination schemes, i.e., mixing at atomic level or embedding Li_2MnO_3 domains of different sizes in NMC matrix or both. Moreover, this approach can be applied to screen lithium rich Mn and other novel material combinations in a more controlled and expedient manner.

---

*This chapter is reprinted with permission from "A new approach to investigate Li_2MnO_3 and $Li(Ni_{0.5}Mn_{0.3}Co_{0.2})O_2$ mixed phase cathode materials", C. Jacob, J.Jian, Y. Zhu, Q. Su and H. Wang, J. Mater. Chem. A, (2014), 2, 2283.© Royal Society of Chemistry 2014.

5.2 Introduction

A new class of mixed oxide materials like,$xLi_2M'O_3 \cdot (1-x)LiMO_2$ or $xLi_2M'O_3 \cdot (1-x)LiMn_2O_4$ (M' = Ti, Mn, Zr; M = Ni, Mn, Co or a combination ;$0 \leq x \leq 0.3$)amongst others, has recently provided fresh impetus to lithium ion battery research [216-220]. Thackrey and co-workers first reported that mixed phase Li-rich compounds are capable of nearly doubling the capacity of most existing chemistries[217, 219].A variety of synthesis techniques including solid state [221-223], co-precipitation [224, 225], sol-gel [226, 227], amongst others have been demonstrated for synthesis of this material. Studying this class of materials is challenging due to difficulties in characterization, synthesis and selection of structurally and electrochemically compatible combination of phases. The actual microstructure and phase morphology of these compounds, both in the pristine form and after cycling, is a subject of on-going debate Thackrey et al., originally proposed that the two phases co-exist with Li_2MnO_3stabilizing the LiMO2 structure at high voltage extraction and this was supported by work presented by several researchers[110, 219, 228].Others have suggested that a single Li_2MnO_3 like structure is formed during the combined synthesis [110, 229].The $R\bar{3}m$ $LiMO_2$ structure and $C2m$ Li_2MnO_3 structures are closely related and have similar d-spacing and hence distinguishing between them is challenging [229].The proportion of the Mn phase introduced during synthesis also needs optimization to achieve high capacity [170, 216, 230].Li_2MnO_3 is the predominant Li-rich phase used in most of the studies. However, the electrochemical behaviour of Li_2MnO_3 has been reported to be very sensitive to synthesis techniques and the resulted microstructures[231, 232].For example, the size of Li_2MnO_3 particles and the Li and O stoichiometry greatly control its characteristics[233].

Cation mixing in transition metal oxides and formation of impurity phases has been extensively reported in cathode material synthesis [234, 235]. Moreover, Mn based oxides are susceptible to phase transformation which can results in formation of undesirable phases like $LiMn_2O_4$, $Li_2Mn_5O_{12}$ amongst others. Furthermore, the Li-rich cathode materials performance has also been reported to be dependent on synthesis technique[227]. Very little progress has been made to identify substitute for Li_2MnO_3, partly due to the fact that the same precursors are used for synthesizing $Li(Ni_{0.5}Mn_{0.5})O_2$ or $Li(Ni_xMn_yCo_{1-x-y})O_2$. Using conventional synthesis technique with other precursors might lead to impurity phases or generate compounds other than the $Li(Ni_{0.5}Mn_{0.5})O_2$ or $Li(Ni_xMn_yCo_{1-x-y})O_2$ compounds. All these above challenges have hindered the development of this material for commercial applications for the past few years. It is essential for experimental phase and microstructure studies, that a synthesis technique that allows fine control on the above parameters be employed.

Recently, our ability in growing high quality complex metal oxides cathodes by pulsed laser deposition (PLD)[236], without the need for post annealing, provides the possibility of exploring Li-rich chemistries using thin film approach. In this study we report, for the first time, fabrication of Li-rich cathodes by PLD. Through this approach, pure phase materials were used in an effort to demonstrate a more controlled approach for the design and study of these complex composite materials. PLD has been widely used for investigating superconductors [237, 238], ferroelectrics[239, 240],semiconductors [241], and even battery materials . Interests in solid state batteries have spurred several research groups to investigate thin film $LiCoO_2$[242, 243],$LiFePO_4$[244, 245], and $LiMn_2O_4$films [183, 246] in the past.

Here, we propose the use of a PLD-based method to study Li-rich cathode material. The ability of PLD to break down and reconstitute at atomic level could allow the two phases to interact and form both thermodynamically stable composition as well as meta-stable phases. Since the starting material are pure phase compounds, it is reasonable to expect that the end product will be either a mixture of the two or a more stable single phase, whichever is more thermodynamically stable. Moreover, by varying the deposition scheme, the films can be intentionally made more 'domain' or 'integrated' phase like. Two such schemes are attempted in this work. Films were deposited, using either a uniformly mixed two phase composite target (composite films), or in multilayer form, by alternately using two different pure phase targets (multilayer film), as illustrated in Figure 51 a and b, respectively, on stainless steel and c-cut sapphire substrates. Microstructural characteristics by X-ray diffraction [XRD], high resolution transmission electron microscopy [HRTEM], high angle annular dark field mode (HAADF) scanning transmission electron microscopy [STEM] and selected area electron diffraction [SAED] were coupled with the electrochemical properties by cyclic voltammetry [CV], electrochemical impedance spectroscopy [EIS] and charge-discharge cycling.

5.3 Experimental

The Li rich films were deposited using a Lambda Physik KrF excimer laser with a wavelength of 248 nm. Gold buffered stainless steel (Au-SS) and *c*-cut sapphire (α-Al_2O_3) substrate were used for all depositions. Targets were prepared using commercial $Li(Ni_{0.5}Mn_{0.3}Co_{0.2})O_2$ (NMC) and Li_2MnO_3 powder. Pure phase NMC and Li_2MnO_3 targets

were prepared by uniformly mixing the respective powder with additional 15% Li_2CO_3, followed by pressing into a pellet using hydraulic press. The composite target was prepared in a similar manner but with NMC and Li_2MnO_3 powders in a 7:3 molar ratio. All targets were then annealed in a high temperature tube furnace at 950 °C for 8 hours. A laser fluence of 6 J cm^{-2} and a repetition rate of 10 Hz were used for deposition. The 15% Li_2CO_3 was added to compensate for Li loss due to its volatility at high temperature as well as loss during pulsed laser deposition as discussed in our previous work [236].The target substrate distance was kept at 4 cm and substrate temperature was maintained at 750 $^{\circ}C$ during deposition. Films were prepared in an oxygen pressure of 20 mtorr. After deposition the substrate was cooled at a rate of 5 $^{\circ}Cmin^{-1}$ in a 10 torr oxygen partial pressure. The composite film was deposited directly using the composite target. The multilayer films were deposited by alternating the pure NMC (700 pulses) and Li_2MnO_3 (300 pulses) targets for 10 times to achieve the same number of total pulses as that for the composite film. The schematic diagrams of the composite and multilayer films are shown in figure 5.1a and 1b respectively. These are designed structures for the respective deposition schemes.The structure and crystallinity of the film were investigated with grazing incidence X-ray diffraction (GIXRD) (PANalytical Empyrean 2 X-ray diffraction system) and SAED (JEOL 2010 transmission electron microscope) and HRTEM (Tecnai F20 transmission electron microscope). Film thickness was measured using a Dektak 150 profilometer. Electrochemical measurements were carried out using 2032 coin cells prepared in an Ar atmosphere glove box, (O_2 0.1ppm, H_2O 0.1ppm) with a Li metal anode and 1M $LiPF_6$, EC:DEC electrolyte (BASF). A minimum amount of electrolyte was used to prevent erroneous capacity due to oxidation of

electrolyte at high voltage.CV measurements were carried out on an Arbin BT2000 system at a 50 uVs^{-1} scan rate. EIS was carried out on a Gamry system. Charge-discharge cycling and C-rate studies were also performed on the Arbin BTS 2000 system.

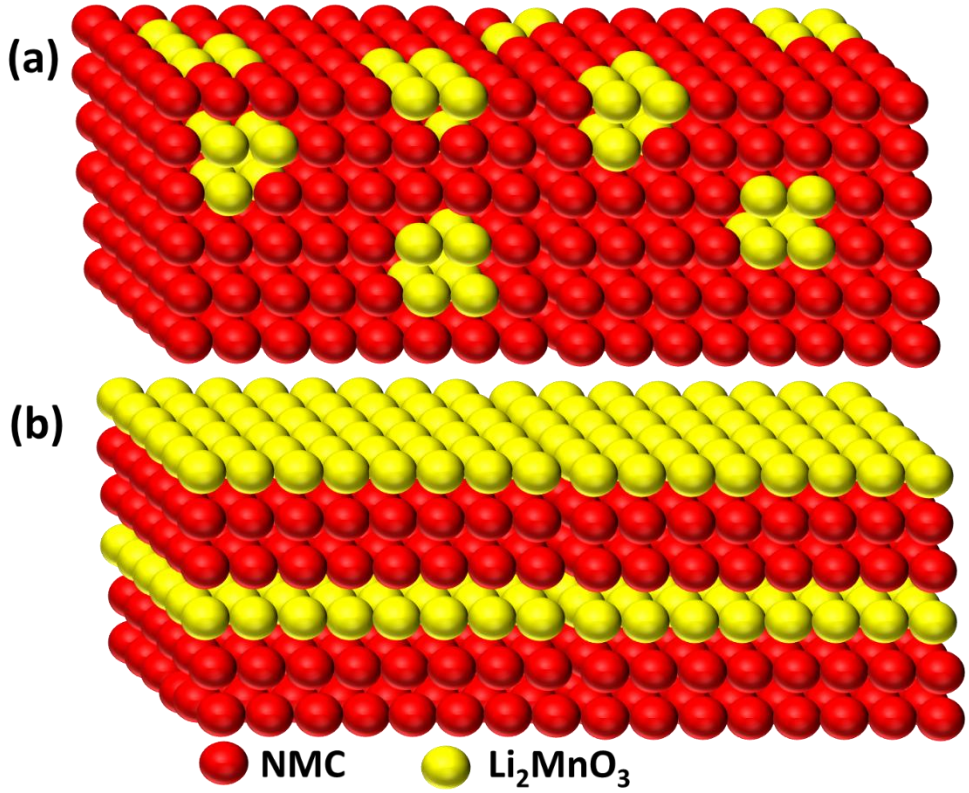

Figure 5.1. Theoretical representation of designed microstructure for, (a) composite, (b) multilayer films with yellow spheres representing Li_2MnO_3 unit and red ones representing NMC unit.

5.4 Results and Discussion

To minimize the substrate influence on the overall XRD results from conventional θ-2θ scans, and to maximize signal strength from weak peaks, GI-XRD is employed for exploring the film microstructure. Figure 5.2 shows a 1° GI-XRD plot of the pure phase

Li_2MnO_3 and NMC films, as well as the composite and multilayer films deposited on the Au-SS substrate at 750 $^{\circ}$C as described above. The Au buffer peak is significantly reduced, with more profound peak information from the films. The pure NMC film is highly textured along the (003) direction while the Li_2MnO_3 pure phase film shows a strong texture along the $(33\bar{1})$ direction. The preferential orientation, partially suppresses weak peaks and hence do not show the characteristic reflection between 20° and 25°. The small film thickness also contributes towards absence of the weak peaks. The composite film displays preferred orientation along $(33\bar{1})$ directions like the pure Li_2MnO_3film, but the (003) $R\bar{3}m$ and (001) $C2m$ peaks almost disappear. On the other hand the multilayer film displays (003) $R\bar{3}m$/ (001) $C2m$ as well as the (110) $R\bar{3}m$/ $(33\bar{1})$ $C2m$. This possibly indicates that, in the composite films, the Li_2MnO_3 type structure dominates due to poor control on composition leading to more Li_2MnO_3 content. Alternatively, as originally intended, during deposition the two phases are integrated very well and the Li_2MnO_3-type structure is more thermodynamically favourable. In comparison, the multilayer film has the strong textured peaks of both Li_2MnO_3 and NMC. This suggests that both these phases are present in the film. This data must however be interpreted cautiously, as most of the characteristic XRD peaks of both Rhombohedral NMC and monoclinic Li_2MnO_3 overlap. During laser ablation of the target material, ionic, atomic, molecular and micro particles are formed. The plasma containing these species further interacts with the laser before adsorbing on the substrate. These energetic species can be reconstituted in target stoichiometry, or can interact to form a new thermodynamically favourable phase. In this case a non-equilibrium technique like PLD can provide activation energy for formation of a more stable single phase [110, 219, 228], or

in the absence of such a stable phase, simply form two different phases [110, 229]. This will depend on the interaction between the two starting phases and deposition conditions. The GI-XRD of the results of the multilayer film suggests that the two phases co-exists, while the composite film data seems to be inconclusive.

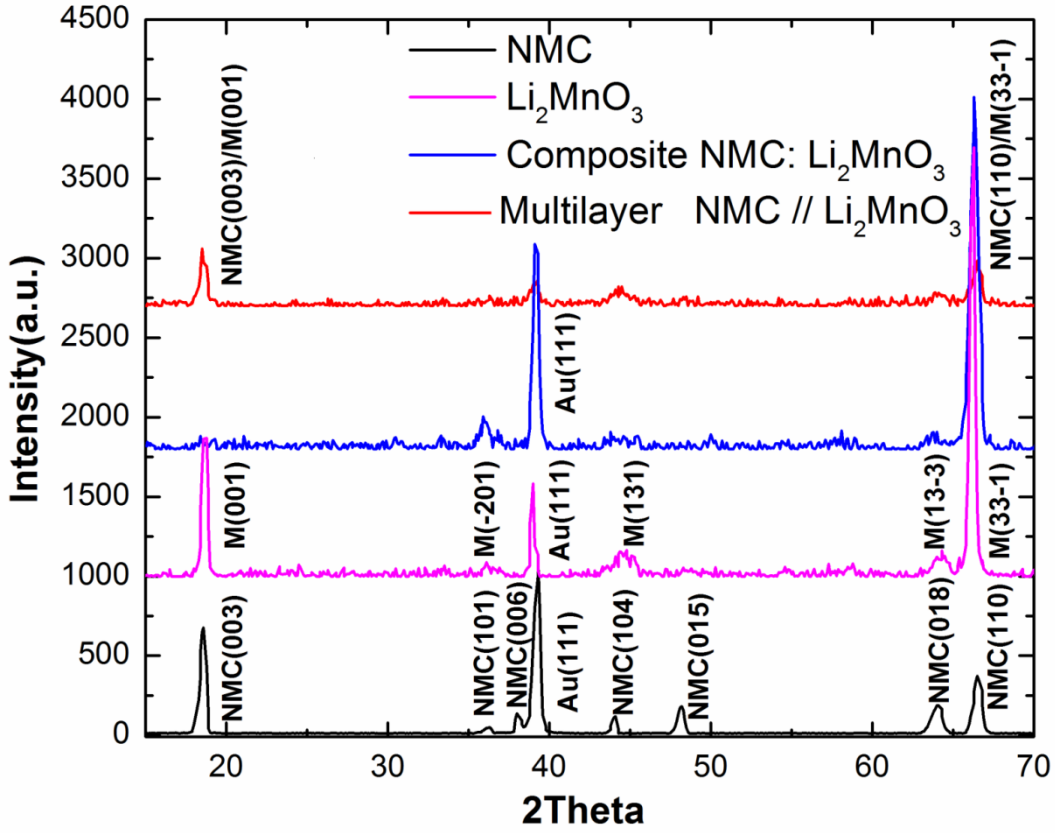

Figure 5.2. Grazing Incidence XRD patterns recorded for thin film, NMC, Li_2MnO_3, Composite NMC:Li_2MnO_3 and multilayer NMC // Li_2MnO_3 on Au-SS substrates.

To further study how the overall microstructure is influenced by the interplay between the two phases, detailed cross-section TEM studies for the multilayer and composite films on α-Al_2O_3 substrates were conducted and the TEM images are shown in figure 5.3a and 5.3b,

respectively. In low magnification images, it is difficult to distinguish the two phases and the composite film seems to be a random mixture of the two phases. In our previous study, it was demonstrated that under similar deposition condition pure phase NMC films show a distinct columnar growth with strong (003) texture[236]. However, the dynamic interaction between Li_2MnO_3 and NMC prevents such growth morphology here, i.e., the film is more uniform without obvious columnar grain boundaries in the view area. The multilayer film shows somewhat similar features as the composite film (e.g., uniform film growth without obvious columnar grain boundaries), but does show obvious multilayer structures as marked by the white arrows in figure 5.3b. Interestingly, the thin Li_2MnO_3 inter layers are not continuous across the film possibly due to the relatively thin layer, ~5 nm to 7 nm. It is also possible that a certain amount of miscibility between the two phases at high deposition temperatures prevents the formation of perfect multilayers. Conversely, a composite film like interaction between the two phases could be occurring. A STEM image (figure 5.3c) of the multilayer film taken under HAADF, also called Z-contrast imaging where the image contrast is proportional to ~ Z^2, clearly shows the multilayer structure with thin Li_2MnO_3 layers across the film area. The sharp interface between the Li_2MnO_3 and NMC regions suggests minimum diffusion of the latter in the Li_2MnO_3domains.This microstructure is uniquely different from conventional Li rich cathodes which are closer to the composite scheme. Further atomic scale STEM analysis to investigate the phase distribution is currently underway. SAED is used to further probe the film phases and the corresponding SAED is shown in figure 5.3d and 5.3e for the composite film (figure 5.3a) and the multilayer film (b), respectively. Surprisingly both diffraction patterns share several common features: (1) both patterns clearly show the

presence of a monoclinic Li_2MnO_3 and rhombohedral NMC component as indexed; (2) both films grow high quality epitaxial-like, with c-axis as the out-of-plane orientation, evidenced by the distinctive diffraction dots from both phases. Except, the composite film displays Several very minor diffraction spots, which can be attributed to in - plane rotations in the

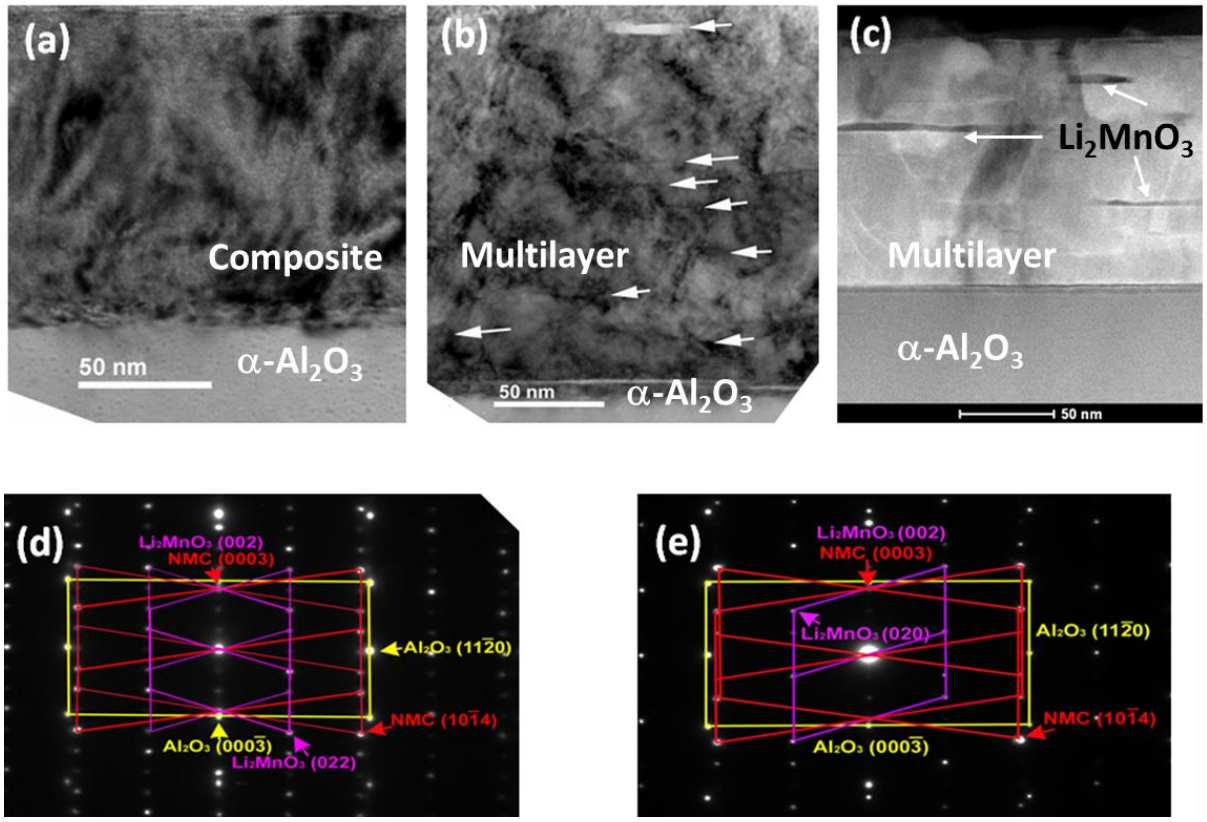

Figure 5.3. Low magnification TEM images, (a) composite NMC:Li_2MnO_3,(b) multilayer NMC // Li_2MnO_3, (c) STEM image of multilayer NMC // Li_2MnO_3, (d) SAED pattern of composite NMC:Li_2MnO_3 ,(e) multilayer NMC // Li_2MnO_3film, on α-Al_2O_3 substrate.

film. The diffraction spots are shaper for multilayer film and unlike the composite film; it does not show weaker diffraction spots. This confirms that the multilayer film has an NMC framework and embedded Li_2MnO_3 nano-domains. This reduces cation mixing in the

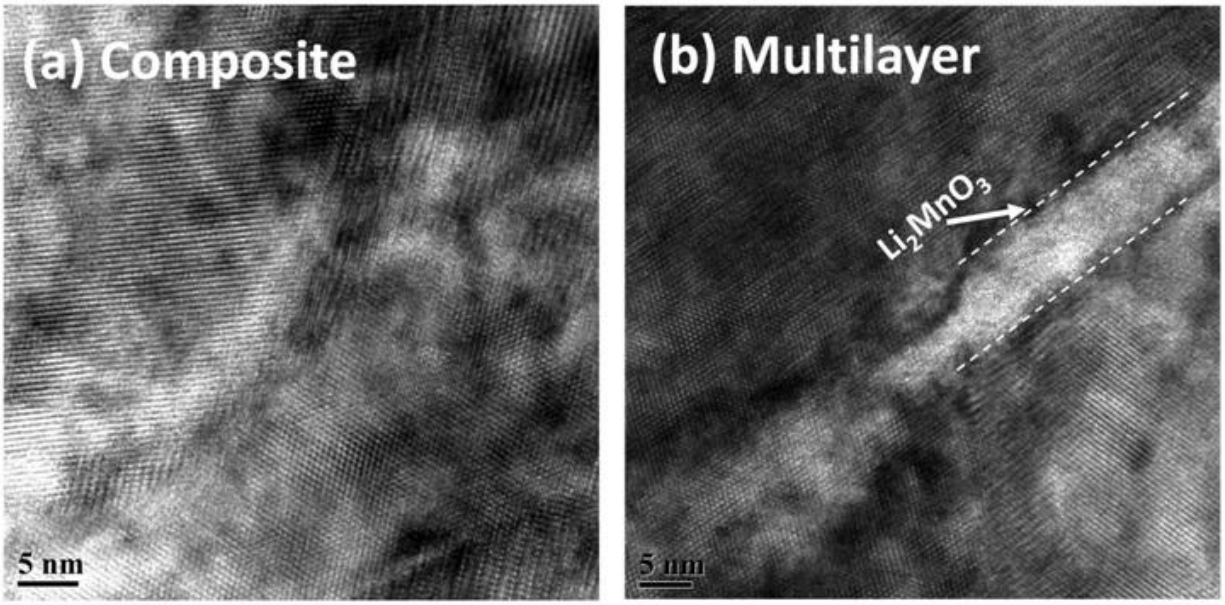

Figure 5.4. HRTEM image of (a) composite NMC:Li_2MnO_3 , (b) multilayer NMC // Li_2MnO_3 film on α-Al_2O_3 substrate.

Li_2MnO_3 regions. The HRTEM images of the composite and multilayer films are shown in figure 5.4a and b, respectively. Similar to the observation in low magnification images, there is no obvious contrast between the two phases in the composite film as shown in figure 5.4a. While similar results have been reported earlier in bulk composite samples [170, 219], this is interesting here since the composition of the target and the expected film composition are known. This also supports our hypothesis that the PLD method can simulate the bulk synthesis process. The multilayer film shows distinct Li_2MnO_3 regions as thin intermittent layers as marked in figure 5.4b. The obvious existence of Li_2MnO_3 provides direct evidence supporting some of the structural features reported previously by several groups where they claimed that the enhanced electrochemical properties are resulted by the existence of Li_2MnO_3, however without direct evidence [170, 219].Since the multilayer structure is not

continuous, we believe that the composite-like regions also exist in the multilayer films. The implications of this morphology are further elaborated in subsequent sections, in context of the electrochemical data. Based on the above structural analysis, the PLD method can be used to vary composition and stoichiometry of the Li-rich films in a more controlled manner by varying targets and deposition sequence. Laser fluence, deposition frequency, ambient gas pressure and substrate temperature can be used to alter nucleation and cluster formation to modify film morphology easily.

The CV of composite, multilayer and pure NMC cathodes are shown in figure 5.5. The results obtained are comparable to bulk composites reported in literature for solution based synthesis [170, 225]. The CV of the composite cathode films shows several distinct peaks. The oxidation peak pair at 3 V and 3.25 V and the corresponding cathodic pair at2.85 V and 3V can be assigned to Mn^{3+}/Mn^{4+} couple. The peak at 3.9 V is associated with Ni^{2+}/Ni^{4+} and Co^{3+}/Co^{4+} pairs. The multilayer mixed phase cathode shows a broad peak during the anodic scan and a 3.1 V peak in the cathodic scan attributable to Mn^{3+}/Mn^{4+} redox couple. The Ni peak is seen at 4.1 V, which is shifted with respect to the composite CV. Li_2MnO_3 domains in the multilayer films likely develop a higher local over potential due to poor conductivity. This results in a large spread of voltages over which the extraction of Li occurs, causing peak broadening. This also explains why distinct Mn peaks seen in the composite film is obscured by a broad peak in the multilayer film. The CV of a pure NMC thin film is provided for reference.

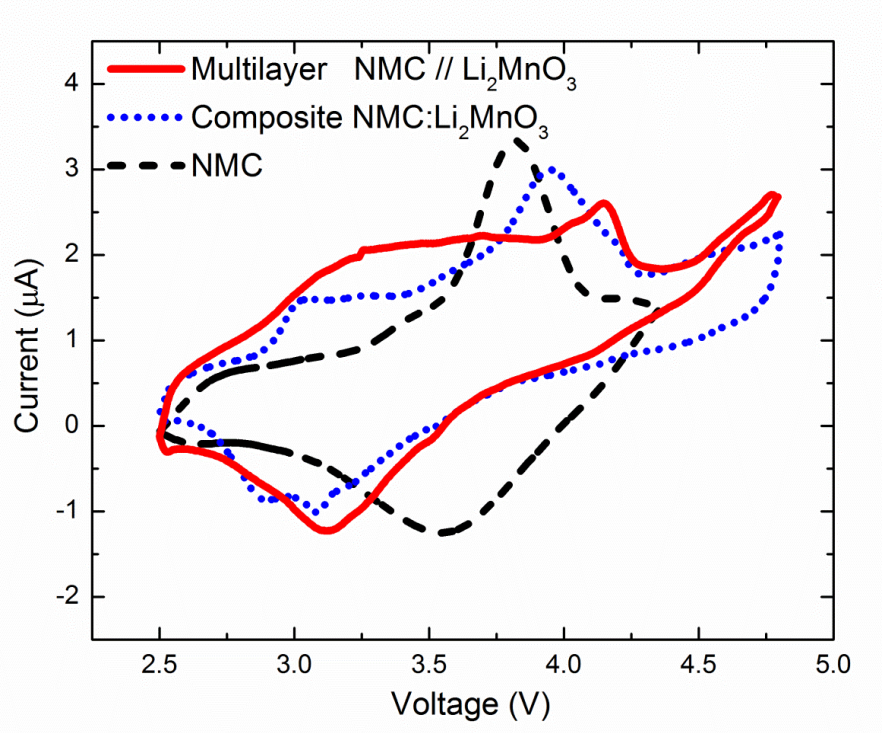

Figure 5.5. Cyclic voltammetry data of pure NMC, composite NMC:Li_2MnO_3 and multilayer NMC // Li_2MnO_3 thin film cathodes on Au-SS substrates.

Cathodic and anodic peaks recorded at 3.55 V and 3.75 V, respectively, can be attributed primarily to the Ni^{2+}/Ni^{4+} redox couples for the pure NMC cathode. There is no peak around 3 V associated with Mn as expected due to the presence of Mn^{+4} in NMC. The discharge capacity of all the cathode films when cycled between 2.75 V and 4.35 V, 4.8 V and 2.5 V is shown in figure 5.6b. A similar trend is seen in this case, as well as with the multilayer, NMC and composite films displaying discharge capacities of 214 mAh g^{-1}, 187 mAh g^{-1} and 169 mAh g^{-1} respectively at 0.1 C. The multilayer film shows a higher or comparable capacity to

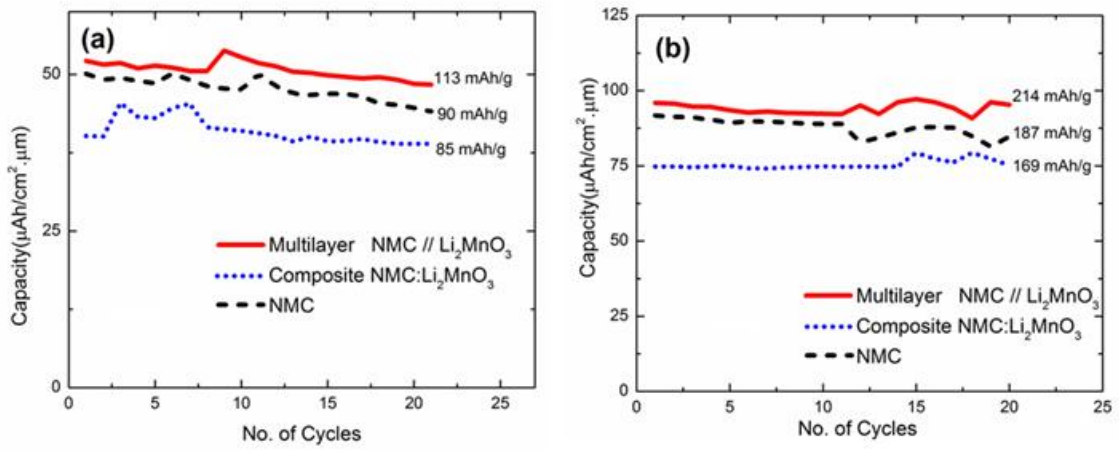

Figure 5.6. Capacity of pure NMC, composite NMC:Li_2MnO_3 and multilayer NMC // Li_2MnO_3 thin film cathodes on Au-SS substrates after electrochemical activation when cycled between, (a) 2.75 V and 4.35 V and, (b) 2.5 V and 4.8 V.

those reported for the similar composition for bulk materials [221, 224, 225]. It is surprising that the composite material capacity is lower than that of NMC; more so, since the CV clearly indicates Mn redox activity, after electrochemical activation. It is possible that complete activation of Li_2MnO_3 does not occur which means that there is less 'active' material in the composite film compared to the pure NMC film. The composite film results obtained here, are consistent with bulk Li rich batteries reported for similar compositions[170]. In fact, for similar composition the multilayer film gives results comparable to an optimized 50% Li_2MnO_3 in bulk cases[170]. It should also be noted that the composite film is deposited from a single target containing both phases. This reduces the control on the composition of the film, especially if the constituent materials have different densities and melting points. The composite approach is thus similar to solution based techniques, where the cation proportion rather than phase is directly controllable. Moreover,

the template-like behaviour of NMC, i.e., Li_2MnO_3 interlayer lattice confined by NMC matrix, could also be responsible for better capacity and cycling behaviour of the multilayer scheme. The NMC film layer will influence the growth kinetics of the Li_2MnO_3 phase more strongly and this confinement effect might make it more stable during cycling. While traditionally Li_2MnO_3 is used to stabilize the $LiMO_2$ phase, the reverse also applies, as reported by *Nakamura* and co-workers [232]. Furthermore, in the composite case, the Li_2MnO_3 and NMC are very closely integrated, and therefore, it is more likely that Ni^{2+} ions (0.69 Å) substitute the Li^+ ions (0.76 Å) during the activation step[234, 235, 247]. This would inhibit Li intercalation/deintercalation from Li_2MnO_3 resulting in irreversible capacity loss. In case of the multilayer samples, the distinct Li_2MnO_3 domains are less likely to suffer from Ni ion substitution. The domain size also plays a critical role in the electrochemical behaviour. Since the Li and electron kinetics is slower in Li_2MnO_3, increasing the domain size beyond a critical value will limit the performance improvement. The multilayer scheme can be used to optimize the Li_2MnO_3 domain size and more work is currently underway to explore the flexibility in materials design based on the PLD technique.

The rate capability of the control NMC and the mixed phase materials are shown in figure 5.7a. The multilayer type battery gave a high capacity of 293 mAh g^{-1}(130 µAh $cm^{-2}\cdot\mu m^{-1}$) at 0.05 C. In general, the multilayer film has a higher capacity at all measured c-rates; but interestingly, the drop in capacity is less severe for the composite case, despite the fact it has the lowest capacity among all three samples compared. Moreover, the rate performance of the multilayer closely follows that of the pure NMC film. This gives further evidence to

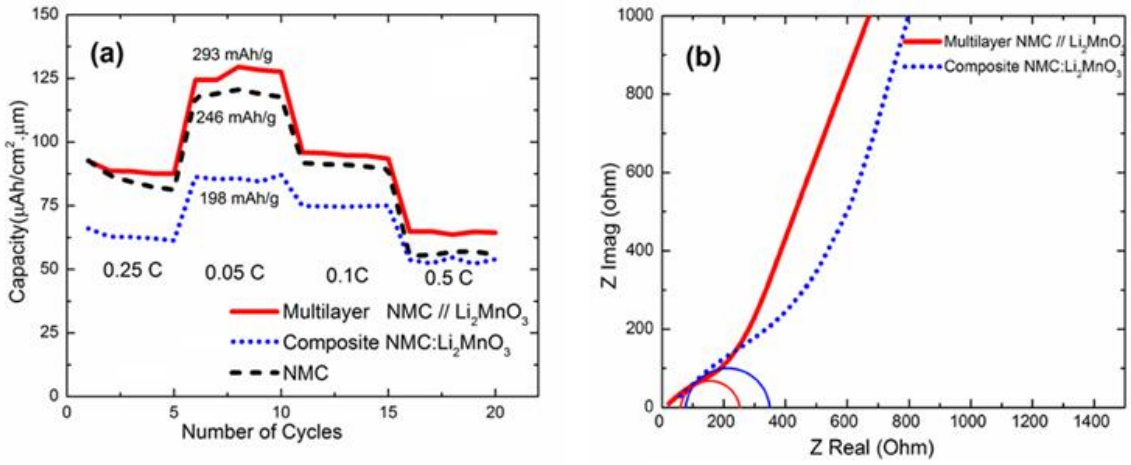

Figure 5.7. (a) Rate capability of pure NMC, composite NMC:Li_2MnO_3 and multilayer NMC // Li_2MnO_3 and, (b) EIS data for the NMC:Li_2MnO_3 and multilayer NMC // Li_2MnO_3 thin film cathodes on Au-SS substrates.

our hypothesis that the structural and electrochemical performance of the multilayer film is more strongly influenced by the NMC phase. In fact since the Li and electron diffusion pathways for the Li_2MnO_3 domains is through the NMC framework, it is expected that the rate capability behaviour of the NMC and multilayer film will be similar. It should be kept in mind that, beyond a critical size, the Li_2MnO_3 domain will dominate the rate capabilities. The ohmic resistance from contact, electrolyte and separator is identical for both the cells as can be seen from the EIS plot in figure 5.7. The left intersection of the projected semicircle gives the ohmic resistance, while the radius corresponds to the respective charge transfer resistance (R_{ct}). Clearly, R_{ct} is significantly higher for the composite sample. R_{ct} for the composite and multilayer film is around 100 Ω and 150 Ω respectively. The Li_2MnO_3 is more closely integrated with the NMC film in the composite case as compared to the multilayer film. This could mean that the multilayer film allows more pathways through the NMC film for the electron and Li flow as well as cation mixing in the composite film.

The composite scheme is in agreement with bulk results for low Mn content[170], while the multilayer scheme with similar Mn content gave superior results. Clearly, in the multilayer film, the existence of both atomically mixed and discrete domains of Li_2MnO_3 improves the battery performance. A possible application towards bulk synthesis technique could be mixing pre-synthesized Li_2MnO_3, with optimized particle size in the Li-rich cathode phase either with simple mechanical mixing or via core shell type structures. Also this study has been limited to 0.3 Li_2MnO_3: 0.7 NMC, and the effect of varying this proportion on the two schemes should be interesting. Whether excess Mn causes phase separation and small nano domains are formed even in the composite case and is responsible for better performance for an optimized ratio is currently being investigated. Furthermore, multilayer and other novel schemes can be used to control domain sizes to optimize battery performance. Effect of doping and coating can also be evaluated by using appropriate targets. This technique can be used as a fast screening method, and also provide guidelines for designing the chemistry and morphology of the end products for solution based techniques.

5.5 Conclusion

A thin film approach to investigate Li-rich materials for Li-ion batteries is presented. The microstructural and electrochemical measurement results suggest that the mixed phase composites obtained are of comparable to those obtained via bulk synthesis techniques for similar stoichiometry. The multilayer deposition scheme allows a greater control on the morphology and composition of the film. The multilayer film, with distinct nano-domains of Li_2MnO_3, in combination with closely integrated Li_2MnO_3 and NMC regions demonstrated

superior capacity. On the other hand the composite film shows more distinct redox activity suggesting the possibility for further improvements via target composition and deposition recipes. This preliminary work suggests that this thin film approach for processing mixed phase composites can be used to probe Li-rich materials with complex stoichiometry and phases. The exploration could lead to interesting insights in the fundamental mechanisms of composition and phase morphology effects on the overall battery performance.

CHAPTER VI

COMPARING THE EFFECT OF OXYGEN STOICHIOMETRY ON THE BEHAVIOR OF Li_2MnO_3 IN PURE PHASE AND Li-RICH FORMS*

6.1 Overview

Thin film batteries have been proposed as a means of designing focused experiments to analyze and develop lithium ion batteries. This works presents an investigation of oxygen stoichiometry on the behavior of Li_2MnO_3 and related cathode materials using thin film techniques. It is shown that pure Li_2MnO_3 and Li_2MnO_3 based Li rich cathodes behave very differently. Li rich cathodes performed best when deposited at low oxygen partial pressure while Li_2MnO_3 required moderate partial pressure for optimum capacity. This behavior is attributed to impurity formation in pure Li_2MnO_3 at low O stoichiometry as well as stabilization of Li_2MnO_3 by NMC matrix in case of the Li rich cathodes.

6.2 Introduction

Recently thin film batteries are gaining popularity due to its flexible form factor and improvements in solid state electrolytes. Solid state batteries are ideal for integration with miniature autonomous platforms, MEMS sensors and even integrated circuits [248]. We

*This chapter is reprinted with permission from "Comparing the effect of oxygen stoichiometry on the behavior of Li_2MnO_3 in pure phase and Li-rich forms", C.Jacob, J.Jian, R.Guillemette, and H.Wang, ECS Trans., 66, 9, (2015), 295. © Electrochemical Society 2015.

report a powerful alternate application of thin film techniques to numerous works has been reported on thin film cathode materials like $LiCoO_2$, $LiMn_2O_4$, and $LiFePO_4$[248, 249]. Most of these efforts are focused on the development of all lithium ion battery development. It is well known that a wide variety of oxides, nitrides and metallic film can be deposited with a variety of deposition systems. These techniques can be harnessed to develop specific controlled experiments to study different aspects of battery materials, as well as develop new materials. Controlled deposition can be used to design and fabricate cathodes with experimental microstructure, phase, stoichiometry, doping etc. These cathodes are ideal for studying electrochemical and structural properties of the material, independent of conventional electrode variables like conductive additive, binder, porosity, loading, electrolyte volume etc. We demonstrate some of the techniques we developed for studying Li_2MnO_3 based cathodes. Li_2MnO_3 has been of active interest both due to its high theoretical capacity, as well as due to difficulty in understanding its crystal structure or operating mechanism[232]. The crystal structure for Li rich cathodes has been reported as both single monoclinic like phase as well as 2-phase Li_2MnO_3-$LiMO_2$ (M= Ni, Co, Mn), depending on interpretation of transmission electron imaging data[110]. The operating mechanism is curious since in its original form it is electrochemically inactive. It is activated either by acid etching or in its combined form with $LiMO_2$. Activation is generally attributed to oxygen and lithium loss. This work presents a combined study of microstructure and oxygen loss in pure Li_2MnO_3 and Li-rich cathodes. We reported development of a thin film based model for Li-rich cathodes recently as well as those for Li_2MnO_3 cathodes [207, 211]. This work compares the performance of both these cathodes when deposited under varying oxygen partial

pressure. The resulting structure and composition was analyzed using x-ray diffraction, Wavelength dispersive spectroscopy (WDS), high resolution transmission electron microscopy (HRTEM). The electrochemical properties of the cathodes were also evaluated with emphasis on effect of oxygen stoichiometry on the Li rich and Li_2MnO_3 cathode performance.

6.3 Experimental

The cathodes were deposited on stainless steel substrate (SS) with a gold buffer layer for electrochemical measurements and on c-cut sapphire for HRTEM and SAED. The SS substrate was first polished with different grades of sandpaper followed by a polish with 1 um alumina dispersion. The gold was sputtered using a DC sputter system at 150 W and 5 x 10^{-3} mbar Ar partial pressure, at room temperature. This gives a highly textured 111 Au layer for depositing the film. The cathode film itself was deposited using a pulsed laser deposition system equipped with a 248 nm KrF laser. A laser fluence of 6 J/cm^2 and substrate temperature of 750 °C was used. The scheme for depositing Li rich cathodes is detailed in our previous work[207]. The partial pressure was varied between 0 and 50 mTorr for the depositions. XRD measurements were done on a PANalytical Empyrean 2 XRD system using a Cu Kα source with a ½° fixed diffraction slit and a 1 mm receiver slit. To quantify composition of the films WDS was carried out on a Cameca SX50 electron microprobe. An accelerating voltage of 15 KV and beam current of 20 nA was used for the measurements. Since Li cannot be measured directly a difference method was employed to estimate Li content. HRTEM images were taken on a FEI Tecnai G2 F20 ST field emission system.

CR2032 coin cells were assembled in an Ar atmosphere (Glove Box, O_2 0.1 ppm, H_2O 0.1 ppm) with Li metal anode and Celgard 2400 separator. An ethylene carbonate: dimethyl carbonate (EC: DMC 1:2 by volume) with 1 M $LiPF_6$salt was used as electrolyte. Cyclic voltammetry (50 $\mu V\ s^{-1}$) and battery cycling was carried out on an Arbin BT2000 system.

6.4 Results and Discussion

The X-ray diffraction pattern of the Li rich and Li_2MnO_3 cathodes under 5 and 50 mTorr partial pressure is given in figure 6.1a. The 001 peak for Li_2MnO_3 deposited at 50 mTorr and the 003 peak for NMC deposited at 5 mTorr are shifted to the right compared to the other peaks, indicating smaller d-spacing. The weak and broader 001 peak for Li_2MnO_3 deposited at 5 mTorr on is likely due to poor stoichiometry of the sample leading to degradation of the structure. The peak is also shifted to the left compared to the Li_2MnO_3 sample deposited at 50 mTorr. Compositional analysis was performed using WDS to confirm variation in oxygen stoichiometry due to oxygen partial pressure difference during the deposition. Both the oxygen and lithium levels are shown since Li content is dependent on ambient partial pressure during deposition. Figure 6.1b shows the approximate oxygen stoichiometry. The oxygen content in Li_2MnO_3 is proportional to the partial pressure. The Li content is inversely proportional as seen clearly in figure 6.1c. At higher oxygen partial pressure the Li species in the plume are deflected, resulting in lower Li content in the film. HRTEM of the Li rich cathode deposited at 5 mTorr is shown in figure 6.2a. The cathode is designed to have layers or nano-domains of Li_2MnO_3 in a NMC matrix. This structure agrees well with results of bulk Li rich batteries. It was determined that Li_2MnO_3 regions play a

critical role in electrochemical behavior of the cathode (6). The effect of oxygen stoichiometry on the film is shown in figures 6.2b and 6.2c. The sample deposited at 5 mtorr

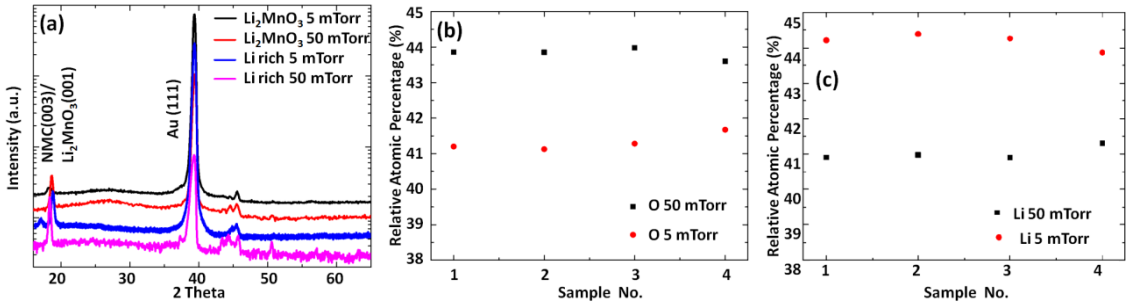

Figure 6.1. (a) XRD Pattern of Li_2MnO_3 and Li rich cathodes deposited on Au-SS Substrate under different oxygen partial pressure. WDS measurement showing, b) oxygen content of Li_2MnO_3 under different partial pressure, (c) lithium content of Li_2MnO_3 under different partial pressure.

shows a distorted lattice as compared to the cathode deposited at 50 mTorr. Both samples showed some localized variations as well. While both the 5 mTorr and 50 mTorr samples show defects, clearly the oxygen stoichiometry causes significantly more distortion to the crystal structure. This agrees well with reports in literature that report defects in Li_2MnO_3 due to Li and O removal by acid etching. A similar result seems to have been achieved by the Li and oxygen loss achieved directly during the deposition process. Further work on comparison of the nature of defects in the two cases and its effect of activation of the cathode is underway.

The rate capability of Li rich cathodes deposited at 5 mTorr and 50 mTorr is shown in figure 6.3a. During initial cycling immediately after high voltage activation cycles, the 5 mTorr sample at a discharge rate of C/30 gave a capacity of 363 mAh/g. Under the same conditions the 50 mTorr sample gave a capacity of 275 mAh/g. While both capacity is significantly higher than any layered cathode material of the $LiMO_2$ class (M= Ni, Mn, Co),

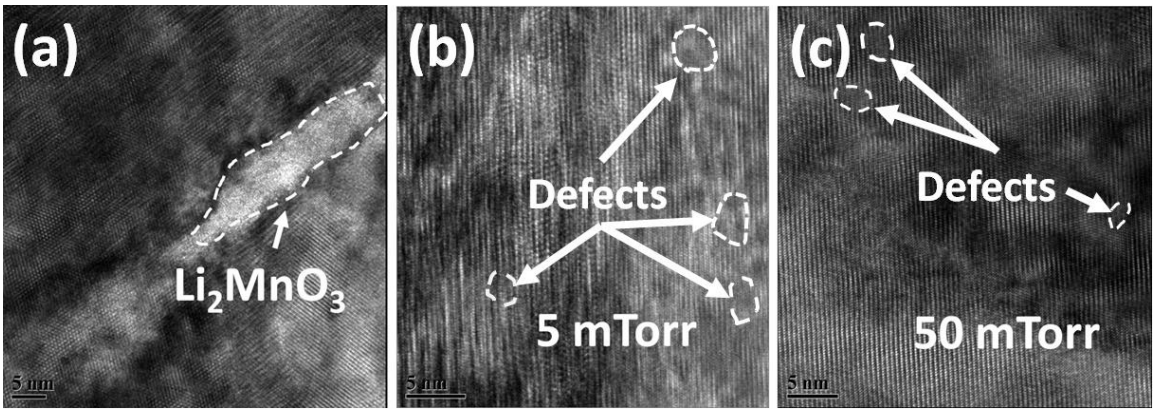

Figure 6.2. HRTEM of (a) Li rich cathode on c-cut sapphire substrate and, Li_2MnO_3 film deposited at, (b) 5 mTorr and, (c) 50 mTorr oxygen partial pressure.

the sample deposited at 5 mTorr shows a sharp improvement over the 50 mTorr sample. This pattern is consistently observed at other C rates as well. Moreover, the capacity of the 50 mTorr Li rich sample decays much faster at higher C-rates. The discharge capacity of the pure Li_2MnO_3 cathodes deposited at 5 and 50 mTorr is also plotted in figure 6.3a. Surprisingly, the effect of oxygen partial pressure on capacity is opposite of that observed for the Li rich cathodes. The cathode deposited at 5 mtorr shows a lower capacity (212 mAh/g) compared to that deposited at 50 mTorr (280 mAh/g) at C/30 rate. This trend remains the same at higher c-rates although the capacity degradation at higher rates is not as severe as those seen in the Li-rich cathodes. The cycling capability of the different cathodes at C/20 rates is shown in figure 6.3b. The trends observed during the cycling is consistent with those observed for rate capability tests see in figure6. 3a. The 5 mTorr Li rich sample gives the best capacity at 290 mAh/g and Li_2MnO_3 cathode performed better at 50 mTorr with a discharge capacity of 225 mAh/g. The effect of deposition under other oxygen partial pressures is currently underway to confirm these results. As stated earlier the behavior of the Li_2MnO_3

phase has been determined to be critical to the behavior of the Li rich cathode. Moreover, oxygen vacancy has been widely reported to be responsible for activation and subsequent capacity of Li_2MnO_3 cathodes[232]. Hence preliminary comparison of the effect oxygen partial pressure on its electrochemical behavior is probed using cyclic voltammetry and is shown in figure6.3c. The cathodes synthesized at 50 mTorr shows a stronger peak at 3 V compared to that observed for the 5 mTorr sample. This accounts for the higher capacity of the 50 mTorr sample. This secondary oxidation-reduction pair at 3 V and 2.75 V is generally attributed to Mn ion after a layer-to-spinel phase transformation that occurs during activation[211].

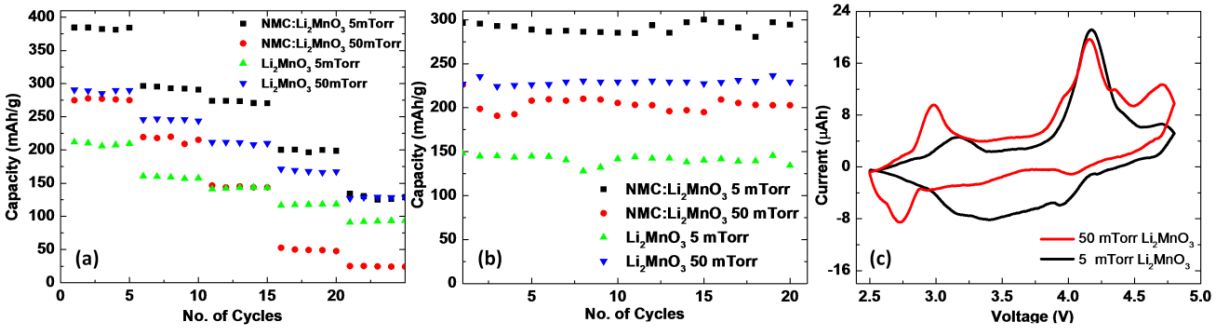

Figure 6.3.(a) Rate capability and, (b) cycling capability of Li rich and Li_2MnO_3 cathodes deposited under different oxygen partial pressure, (c) cyclic voltammetry of Li_2MnO_3 deposited under different oxygen partial pressure.

The WDS data showed that both the samples are oxygen deficient with the 5mTorr sample having lower oxygen content. This resulted in defects in both the samples as confirmed by the HRTEM results. While the XRD pattern for both samples look very similar, in a previous study we had observed that when the cathode was deposited at 0 mTorr MnO_2 impurity phase is observed in the samples [101]. It is possible that this also occurs in the

5mTorr sample but to a lesser extent and hence does not show up in a standard XRD graph. Furthermore, a larger oxygen deficiency could aggravate structural stability since the cathode loses even more oxygen and lithium during cycling. In case of the Li rich cathode since the Li_2MnO_3 domains are embedded in the NMC matrix. The resulting confinement effect helps stabilize the Li_2MnO_3, slowing possible phase transformation. Furthermore, oxygen released by the Li_2MnO_3 domains could be partially trapped in the matrix and re-incorporated into the structure during lithiation preventing irreversible phase change and hence capacity loss.

6.5 Conclusion

Thin film deposition process was used to vary the oxygen stoichiometry of Li-rich and Li_2MnO_3 cathodes. Compositional analysis confirmed that the oxygen content was directly proportional and the Li content varied inversely with the oxygen partial pressure. Li_2MnO_3 films in both cases exhibited defects as confirmed by HRTEM. However the electrochemical performance of Li_2MnO_3 was better at moderate partial pressure of 50 mTorr while the Li rich cathodes gave the highest capacity at low oxygen partial pressure. Initial analysis indicates that the NMC matrix in the Li rich cathode stabilized the Li_2MnO_3 phase, suppressing irreversible structural changes. In the absence of such a framework pure Li_2MnO_3 showed lower capacity at low partial pressure.

CHAPTER VII

CORRELATING COMPOSITION, MICROSTRUCTURE AND ELECTROCHEMICAL PERFORMANCE OF Li-RICH CATHODES USING THIN FILM TECHNIQUES

7.1 Overview

Currently most commercial solid state batteries employ established commercial materials like $LiCoO_2$ and $LiMn_2O_4$, deposited with standard schemes. However, there is a need not only to develop high voltage high capacity electrodes, but also to utilize various thin film techniques to incorporate microstructure engineering, strained layers, and selective doping to optimize thin film performance. In addition, thin film battery research in next generation material is critical to investigate complex electrode systems. In this work, we report the growth of multilayer Li-rich cathodes of $Li(Ni_{0.5}Mn_{0.3}Co_{0.2})O_2$(NMC):$Li_2MnO_3$in thin film form with the layer ratios varied from 30:70, 50:50, to 70:30. We studied the effects of composition variation on the overall battery performance and found that the 50:50 films gave the highest capacity of around 250 mAh/g. Moreover, the results indicate a strong correlation between Li_2MnO_3 domain size on the capacity of the Li rich electrode. Studies into electrode architecture and composition indicate that defect density and conductivity in the system can be tuned using composition and microstructure to yield optimum performance.

7.2 Introduction

Thin film cathodes for Li ion batteries are of interest both for fundamental investigation as well solid state battery development. Solid state batteries have inherent advantages such as higher safety, co-fabrication capability with integrated circuits, longer shelf life, higher thermal and shock resistance[250]. Commercial applications of solid state batteries include embedded battery on various computer components, smart cards, medical devices etc. Cathodes for solid state batteries are mostly restricted to single phase of $LiCoO_2$ and $LiMn_2O_4$.[100, 251-254]Several groups have reported work on $LiFePO_4$ thin film cathodes,[181, 255] but its poor intrinsic conductivity makes it a poor choice for additive free thin film batteries.[256]Some work has been done on changing film orientation by using different techniques.[253, 257] Recently minor stoichiometric variation of Li and O in Li_2MnO_3[101] and Mn in $LiMn_2O_4$[258] has been reported. Up-to-date, limited thin film work has been reported to advance cathode materials via strained layers[259], optimization of substrate film interfaces[260],multilayer structures[261],selective doping, etc. In addition, since most solid electrolytes can operate at high voltage, developing thin film cathodes that operate at high voltage[165], is necessary to fully explore the benefits of solid state batteries. One such material that has generated great interests is the Li-rich cathode. Unlike the traditional materials which take the form of $LiMO_2$, these can be represented as $LiMO_2.Li_2MnO_3$.[110] Traditionally, solution based or solid state synthesis of this material in bulk form leads to formation of an active powder of $Li_{1+x}MO_2$(Where M = Ni, Mn, Co).[216, 262-265]While this has shown promising results in terms of capacity, many scientific questions regarding its structure and operating mechanisms remain. Thackrey et al., originally proposed that the two phases co-exist with Li_2MnO_3stabilizing the $LiMO_2$ structure at high voltage extraction and this was supported by

several reports.[109, 110, 113]Others have suggested that a single Li_2MnO_3 like structure has formed during the combined synthesis [110, 229]. Recently, Bagetto et al. studied the degradation mechanism in Li-rich materials by preparing thin film cathodes from pre-synthesized Li rich powder.[115]Yan et al., also reported a similar finding using pulsed laser deposition.[266] However, thin film techniques can potentially allow for far more complex optimization of such materials. Our earlier report demonstrated that sequential deposition of $Li(Ni_{0.5}Mn_{0.3}Co_{0.2})O_2$(NMC) and Li_2MnO_3 could replicate the results of Li rich chemistry.[207]The resultant structure consisted of nano domains of Li_2MnO_3 in an NMC Matrix. In this work we take advantage of the multilayer architecture to vary the film composition of NMC and Li_2MnO_3. The composition study allows us to further explore the two aspects of Li-rich chemistry and the effects of composition and film architecture on this unique thin film scheme of Li-rich cathodes. Microstructure analysis including X-ray diffraction (XRD), high resolution transmission electron microscopy (HRTEM), high angle annular dark field mode (HAADF) scanning transmission electron microscopy (STEM), was coupled with the electrochemical properties by cyclic voltammetry (CV), rate capability and charge- discharge cycling.

7.3 Experimental

All the multilayer thin films of NMC and $Li_2MnO_3$with different layer ratios were prepared using pulsed laser deposition (PLD) using a 248 nm KrFexcimer laser. The target substrate distance was set at 3.5 cm and a partial oxygen pressure between 5 to 10 mTorr was used. Au-buffered stainless steel, silicon and *c*-cut sapphire were all used as substrates. The Au buffer layer was deposited using a DC Magnetron Sputter at 150 W and 5 mtorr partial pressure with a 6 sccm Ar gas flow. The PLD depositions on all substrates were carried out

at 750 °C. The multilayer scheme was achieved by alternating deposition of the NMC and Li_2MnO_3 targets. Details about target preparation can be found elsewhere.[84] The film composition was controlled by varying the number of deposition pulses on each target, e.g., NMC:Li_2MnO_3 pulse ratios of 30:70, 50:50, 70:30. Under constant pressure conditions this would lead to constant alternating film thickness; while varying partial pressure could lead to progressive varying multilayer film thickness. Film thickness was measured using a Dektak profilometer. The microstructure of the films was determined using XRD measurements (PANalytical Empyrean 2 XRD system using a Cu Kα source with a ½ ° fixed diffraction slit and a 1 mm receiver slit). TEM and STEM study was conducted using a FEI Tecnai G2 F20 ST field emission system and an aberration corrected FEI Titan microscope equipped with a high brightness Schottky-field emission electron source operated at 300 kV respectively. The film composition was verified using a Cameca IMS 4f ion microprobe secondary ion mass spectrometry (SIMS). CR2032 coin cells were assembled in an Ar atmosphere (Glove Box, O2 0.1 ppm, H_2O 0.1 ppm) with Li metal anode and Celgard 2400 separator. An ethylene carbonate: dimethyl carbonate (EC: DMC 1:2 by volume) with 1 M $LiPF_6$ salt was used as electrolyte. Battery cycling was carried out on an Arbin BT2000 system. Differential charge curves were derived from the charge discharge curves.

7.4 Results and Discussion

The XRD θ-2θ plots of the films with different ratios of NMC and Li_2MnO_3layers grown on *c*-cut sapphire substrate are shown in Figure 7. 1. The films show a sharp peak corresponding to the (003) NMC and (001) Li_2MnO_3 peak which coincide at 18.5^o. The

corresponding higher order peaks (006) NMC/(002) Li_2MnO_3 and (012) NMC/(003) Li_2MnO_3 are also seen in the plots. In addition the 50:50 and 70:30 show distinct super lattice peak at 21^o. This peak is very weak in the 30:70 samples. No impurity peaks can be seen in the scans. The compositional profile of the film was measured using SIMS. Since the alternate Li_2MnO_3 layers are expected to be Ni and Co free isotopes of these elements are traced using depth profiling SIMS. Also Li content in Li_2MnO_3 layer will be higher than that in the NMC layer. The SIMS plot showing 58 Ni, 59Coand 7 Li is shown in Figure 7. 2. The Co and Ni plots clearly show a periodic variation with the broad peaks corresponding to NMC Layer. The 70:30 ratio has the widest peaks while the 30:70 samples show relatively narrower peaks. This clearly indicates that distinct peak profile variations corresponding to different compositions and layer thickness have been obtained. Furthermore, the 7 Li trace shows distinct layered structure for the 70:30 and 50:50 samples, however the 30:70 sample shows a relatively flat profile. This is most likely due to the thinner Li_2MnO_3regions not generating enough counts to show distinct peaks.

To further verify the layered structure, cross section TEM and STEM analysis were conducted on the samples. Figure 7. 3a shows a typical cross-section TEM image of a multilayer film deposited under various partial pressures. Since the partial pressure affects the mean free path as well as angular spread of the plume, changing the pressure will vary the film thickness and film morphology. In addition, pressure variation has to be limited to ensure the stoichiometry of the Li based films. Since Li is lighter compared to the other

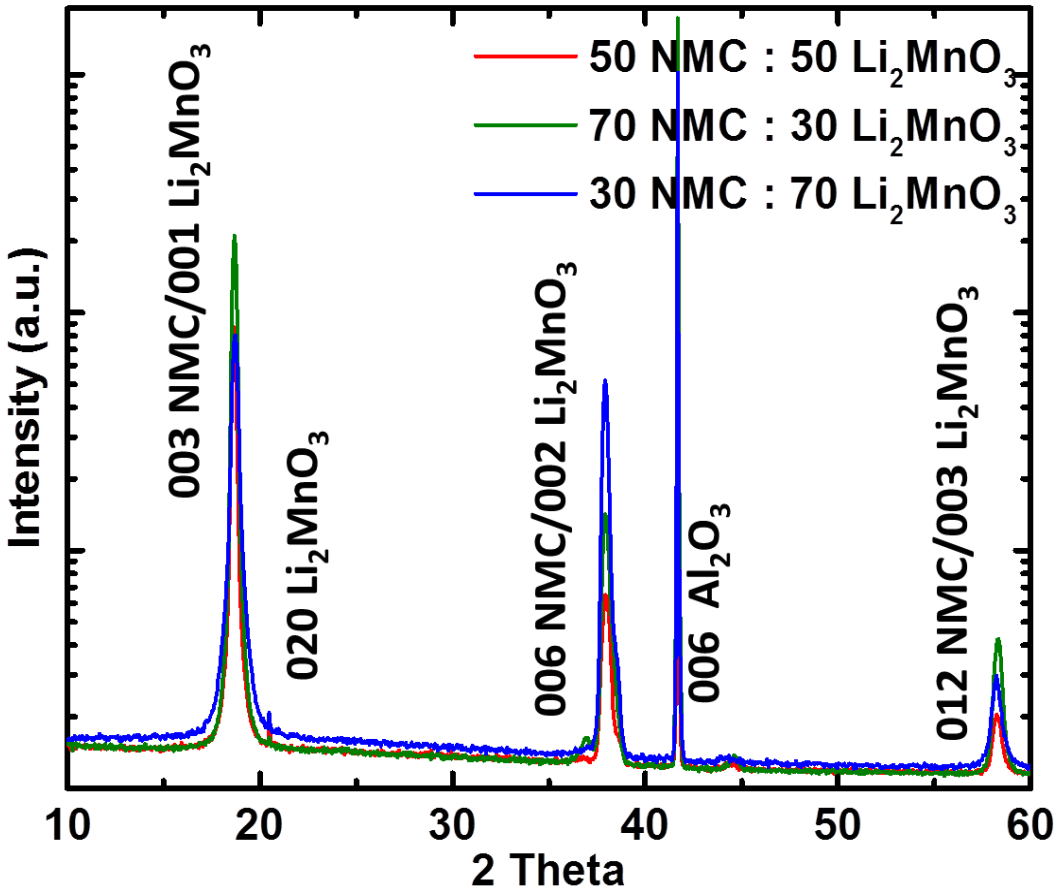

Figure 7.1. XRD patterns showing diffraction pattern of different deposition schemes.

transition metal ions, collision with ambient oxygen molecules results in a larger angular spread compared to other cations. This could lead to lithium deficiency in the film as reported previously.[84]A more flexible way of varying composition is to vary the number of pulses for each target. Figures 7.3b and 7.3c show the cross-section TEM images of those films deposited using this approach. These films were deposited by alternating between the NMC and Li_2MnO_3targetwith a laser pulse ratio of 30:70 and 50:50 respectively. In the TEM images the darker regions correspond to NMC while the lighter regions are Li_2MnO_3 layers. The layers are continuous and even. The thin layers do not show obvious diffusion or

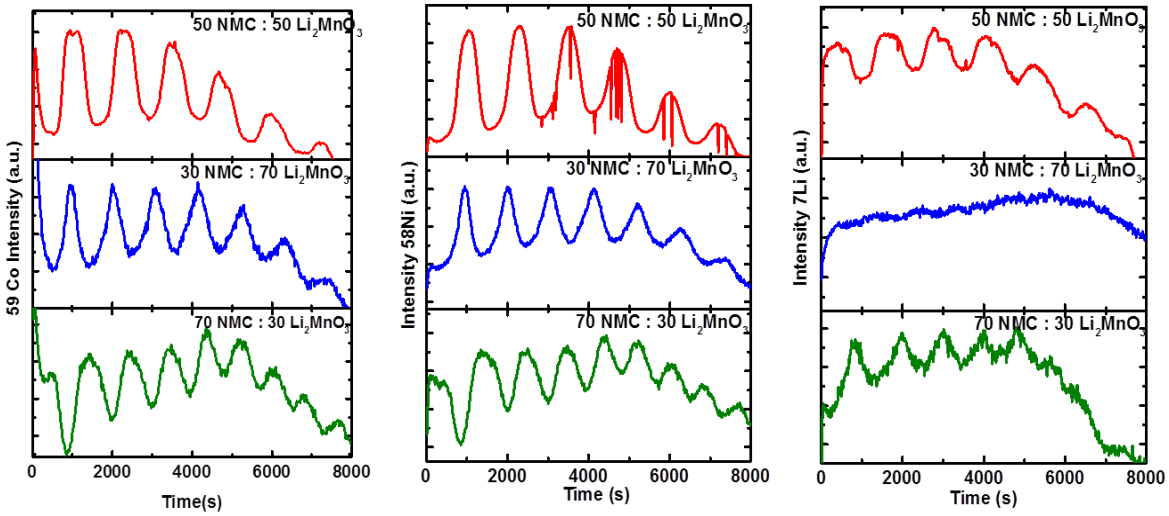

Figure 7.2.SIMS plot showing multilayer films for different schemes**.**

miscibility related issues, thus controlling the layer thickness allows the composition tuning of the overall thin films. In our previous study, a nano-domain structure forms in multilayer structures with thinner bilayer structures achieved by maintaining desired pulse ratio while increasing the number of layers. Such thin bi-layer formation allows the discontinuities, i.e., the formation of nano-domains. [207]Similarly, to make nano-domain structure, the pulse ratio and film thickness are adjusted accordingly in this work. Figure 7. 3d shows a high resolution STEM image of the interface between the NMC and Li_2MnO_3 region. Compared to the TEM images (Figure 7. 3a-c), the image contrast is reversed in the STEM images taken under the high angle annular dark field mode since the contrast is proportional to Z^2. For this case, NMC shows a brighter contrast and the Li_2MnO_3 region is darker. High quality epitaxial growth of NMC on Li_2MnO_3can be seen with clear lattice matching between the two layers. Comparing to the nearly perfect lattice structure in NMC layer, the Li_2MnO_3 layer shows a relatively distorted structure with obvious stacking faults and lattice

distortions. This is a characteristic of defect rich Li_2MnO_3 region seen for this material in both bulk and thin film form.[101, 267] The interface looks sharp, although in certain regions show intermixing within a few nanometers of the interface.

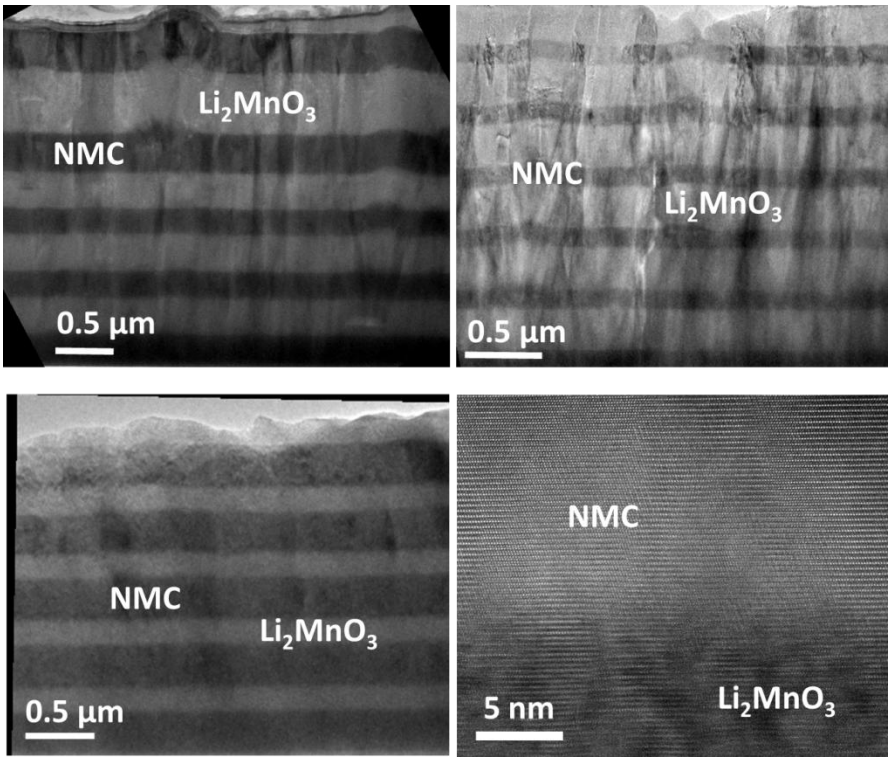

Figure 7.3. HRTEM images of different multilayer schemes and STEM Image showing interface between the films.

Cyclic voltammetry results for different thin film compositions and schemes are presented in Figure 7. 4. All films show an anodic peak around 4.1 V. This peak can be attributed to Ni^{2+}/Ni^{4+}.[266] Mn can also contribute at this voltage due to partial spinel transformation in the Li_2MnO_3layerallowing Mn^{3+}/Mn^{4+} redox reaction.[268] The cathodic peak for the 30:70 sample occurs at 3.55 V while that for the 50:50 sample has the cathodic peak at 3.75 V. The smaller the gap between the redox peaks the better the reversibility. A

higher reversible capability is expected from the 50:50 cathodes. Interestingly no appreciable redox activity is observed around 3 V that's been reported for Li_2MnO_3.[269] Again comparing with the nano-domain model where we noticed such redox activity. In fact the smaller the Li_2MnO_3 region the better defined the 3V peaks were observed. In fact our

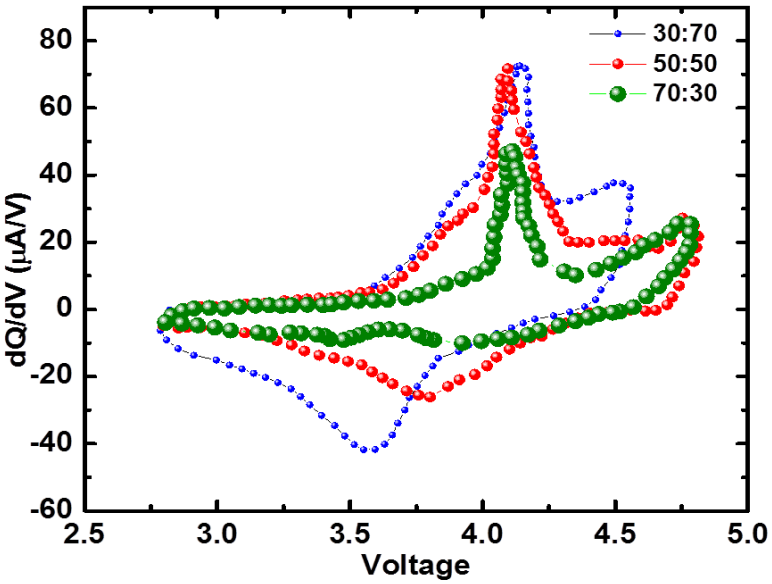

Figure 7.4.Differential charge vs voltage curve for the different multilayer schemes.

earlier work a composite sample showed sharper 3 V peak than those seen upon increasing the Li_2MnO_3 regions to nano-domains size.[207] The results observed here further confirm this trend as larger and continuous domains in this work shows no 3 V activities. While it is likely that some redox activity indeed occurs, it is possibly only a fraction of the actual activity that should occur under optimized conditions. This will be discussed in more details in the following section.

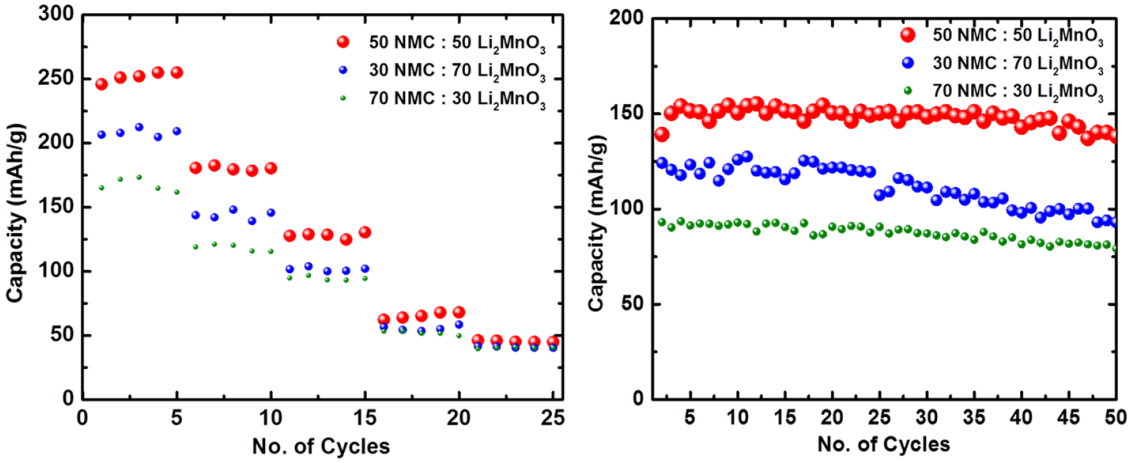

Figure 7.5.Rate capability and cycling performance of the three schemes.

The rate capability of the samples is shown in Figure 7. 5a. The 50:50 sample gives a capacity of 250 mAh/g at C/20 rate almost 20% higher than the 30:70 sample which gave a capacity of 210 mAh/g under similar conditions. At higher C-rates all the samples showed a capacity loss, where both 50:50 and 70:30 samples show very minor capacity loss while that in the 30:70 sample is more obvious. The obvious capacity loss in 30:70 sample can be attributed to the increase in the Li_2MnO_3 content which has much lower conductivity compared to NMC. Thus the 70:30 samples show the least capacity loss with increasing C-rate. This loss occurs due to a combination of poor Li ion and electron conductivity. The latter is traditionally addressed by adding conductive carbon additive in thick film battery. Since this is not possible in thin films due to the high temperature deposition process, other alternative strategies, such as increasing interface area by 3D architecture[270] and doping.[199] The cycling performance is shown in Figure 7. 5b.The 70:30 samples demonstrated the lowest capacity. The 30:70 sample gives an initial capacity of 125 mAh/g but this reduces to around 100 mAh/g at the end of 50 cycles. The 50:50 cathode scheme, has

the highest capacity at 150 mAh/g and this remains almost constant after 50 cycles. This agrees with the interpretation of the dQ/dV plot of Figure 7. 4. The effect of composition variation and its impacts on the electrochemical properties are obvious. The first lies in the poor intrinsic electronic conductivity of Li_2MnO_3. Thicker layers of Li_2MnO_3 will increase the overall resistance of the system by blocking electron paths of the higher conducting NMC component. A higher resistance will lead to increased polarization in the thin film cathode. This can be confirmed by the increased distance between the cathodic and anodic peak observed in the differential charge curve seen for the 30:70 sample in figure 7. 4.The second mechanism arises from the defect linked performance of Li_2MnO_3. It has been widely reported that the electrochemical activity of Li_2MnO_3 is linked to defect driven valence and phase change of MninLi_2MnO_3.[232, 271] On the other hand spinel phase transformation will lead to irreversible capacity loss. This transformation is more likely to occur at the interface between NMC and Li_2MnO_3. Thus compared to thicker Li_2MnO_3 layers this transformation occurs more rapidly in the thinner layer. Hence the 50:50 and 30:70 samples with thicker Li_2MnO_3 layers show higher capacity. An equivalence of this phenomenon in bulk battery work can be observed in grain size effect studies. In fact, Cheng and co-workers recently reported an inverse relation between grain size and capacity for Li_2MnO_3.[272] The composition variation results agree well with a recent core-shell bulk results reported by Noh and co-workers.[273]The core shell structure is the thin film analogy of this work.Li_2MnO_3 stabilizes the NMC phase, however when Li_2MnO_3 becomes the majority component, the stacking faults reduce in a way similar to that in large grains. On the other hand having too low Li_2MnO_3 content reduces the stabilization effect on the overall system.

7.5 Conclusion

This work reports, for the first time, the effect of multilayer architecture and composition variation on capacity of thin film Li-rich cathodes, i.e.,NMC:$Li_2MnO_3$with the composition ratios of 30:70, 50:50 and 70:30. The thin film cathodes with 50:50ratio gave the highest capacity. Furthermore, nano-domain structure in samples with thinner bilayers demonstrate higher capacity compared to the samples with continuous multilayer structure. The thin film-based study results suggest that a combination of composition variation and microstructure control can be used to tune the overall defect density and conductivity of the cathodes. The thin film-based study provides s a unique approach for near independent optimization of composition and microstructure to achieve high capacity in Li-rich cathodes. This approach also provides design guidelines for efficient architectures for bulk Li-rich cathode.

CHAPTER VIII

ENHANCING Li_3PO_4 SOLID ELECTROLYTE FOR $Li(Ni_{0.5}Mn_{0.3}Co_{0.2})O_2$ BASED LITHIUM ION BATTERIES

8.1 Overview

Li_3PO_4 based solid electrolytes are investigated using different pulsed laser deposition schemes. Traditionally nitrogen doping has been pursued to enhance the ionic conductivity and electrochemical performance of this system. This work explores the affect of oxygen [Li_3PO_4 (O_2)], lithium [$Li_{3-x}PO_4$] and nitrogen [$Li_3PO_4(N_2)$] stoichiometry variations on the properties of Li_3PO_4electrolyte film. Since ionic conductivity is enhanced by increasing defect density, such variations should enhance the electrochemical properties. Li_3PO_4 (O_2) coated cathodes demonstrated a high capacity of ~ 80 µAh/µm.cm^2 at 0.75 µA/cm^2 , compared to~ 65 µAh/µm.cm^{2}that was observed in bare electrode and $Li_3PO_4(N_2)$ coated cathodes. However, at higher discharge current (3 µA/cm^2), this behavior was reversed with the Li_3PO_4 (N_2) coated sample showed 50 µAh/µm.cm^{2}capacity, compared to 45 µAh/µm.cm^2 seen in the bare and Li_3PO_4 (O_2) coated samples. Interfacial properties as well as defects were found to be responsible for the observed results. This work demonstrates significant improvement in capacity and cycling performance of cathodes with solid electrolyte coating deposited using pulsed laser deposition.

8.2 Introduction

Li ion batteries are rapidly replacing other battery technologies due to superior energy density and life cycle.[55, 56, 274] However, the use of organic electrolytes limits their operating voltage, volumetric density and operational safety.[56, 275] Solid state electrolytes overcome these limitations and are able to operate safely over wider voltage and temperature range, have higher volumetric density and shock resistance, have flexible form factor and enable co-fabrication with electronic circuits.[276] These advantages make solid state batteries ideal for integration with integrated circuits[277], portable medical devices[278] and space applications.[279, 280] Li_3PO_4 was one of the early solid electrolytes investigated for Li ion battery. Poor ionic conductivity limited its use. Ionic Conductivity (σ), is proportional to concentration (c) of the conducting ion (substitution or interstitial) and its mobility (μ). Nitrogen doping has been shown to improve ionic conductivity.[281, 282] It is believed that nitrogen substitutes oxygen and increases the non-bridging oxygen in the structure. This in turn leads to increased sites for Li ions, improving mobility.[283-285] However, while increasing N ($0.14 < N < 0.29$) improves conductivity ofLi_3PO_4, this effect saturates on further increase of nitrogen. This effect of nitrogen on the lithium environment together with the increased glass density is thought to be counteracting the increase of conductivity for high nitrogen contents.[285] Unuma and co-workers et al.also pointed out that an increase in the network-strain energy by incorporation of nitrogen should produce the opposite effect, i.e. an increase in the total activation energy for conductivity, hence reducing conductivity.[282, 286]

Since mobility can be improved by increasing defects that allow for charge hoping, we explore a more direct means to investigate this. Very little work has been reported on oxygen based defect engineering for Li_3PO_4 thin film. H. Rabaa et al., investigated Li_3PO_4 and N-doped Li_3PO_4 and determined theoretically that N substitution or Oxygen and Li deficiency improves Li conductivity. They predicted that a large concentration of such defects is needed to produce high Li mobility.[287] In a previous study of Li_2MnO_3 we had observed that PLD deposition of Li_2MnO_3 at 50 mTorr of partial pressure lead to defects in the structure. An oxygen deficient structure can also be formed using a nitrogen rich atmosphere during the deposition. While during RF sputter this leads to formation of LiPON.[288, 289] PLD at low energy might not lead to LiPON formation. Zhao et al., reported LiPON film deposited using PLD, though they did not report battery testing results.[290]Another approach is to improve mobility or concentration at the bottle neck like the interface, where trap levels, defects etc. can limit ion mobility. Annealing has been shown to improve interface resistance, but also leads to overall electrolyte resistance.[291] Traditionally, pulsed laser deposition (PLD) supplies higher kinetic energy to the adatoms and can be an alternate to improving the electrode-electrolyte interface.[148] In this work Li_3PO_4 films were deposited under low oxygen partial pressure as well as a range of nitrogen partial pressures. The resulting films are analyzed using X-Ray Diffraction (XRD), Transmission electron microscopy (TEM), Scanning Electron Microscopy (SEM) as well as compositional analysis tools like wavelength dispersive spectroscopy (WDS) and secondary ion mass spectroscopy (SIMS). CR2032 coin cells were assembled for electrochemical testing.

8.3 Experimental

The thin film depositions were done using a KrF, 248 nm, excimer laser. The NMC target was prepared in house by compressing commercial NMC powder into a pellet using a hydraulic press. Details about target preparation have been published in our earlier work. The Li_3PO_4 target was procured from Kurt J Lesker. Gold buffer layer was deposited on stainless steel (SS) substrate using a DC Magnetron Sputter at 150 W power and 5 mtorr partial pressure. These were used for coin cell assembly. C-cut sapphire was used as substrate for samples prepared for structural characterization. The electrolyte was deposited using PLD depositions 750 °C for the cathode at room temperature. Oxygen and Nitrogen partial pressures were varied between 10 mTorr and 200 mTorr. Film thickness was measured using a Vecco Dektak 150 surface profiler. The phases of the substrates were analyzed using a PANalytical Empyrean 2 XRD system. XRD was used to analyze the structure, purity and stoichiometry of the films. TEM and STEM images were taken on a FEI Tecnai G2 F20 ST field emission system and an aberration corrected FEI Titan microscope equipped with a high brightness Schottky-field emission electron source respectively. The film composition was verified with a Cameca IMS 4f ion microprobe secondary ion mass spectrometry (SIMS) as well as Wavelength Dispersive Spectroscopy (WDS). CR2032 coin cells were assembled in an Ar atmosphere (Glove Box, O_2 0.1 ppm, H_2O 0.1 ppm) with Li metal anode and Celgard 2400 separator. An ethylene carbonate: dimethyl carbonate (EC: DMC 1:2 by volume) with 1 M $LiPF_6$ salt was used as liquid electrolyte electrolyte. Battery cycling was carried out on an Arbin BT2000 system. Differential charge curves were derived from the charge discharge curves.

8.4 Result and Discussion

To ensure conformal and pinhole free coverage of the solid electrolyte on the cathode material, the roughness of the NMC cathode film needs to be minimized. Surface roughness has been found to be directly proportional to the deposition partial pressure.[84] Lower pressures tend to reduce surface roughness and 10 mTorr oxygen partial pressure was used for NMC film deposition in this work. Also lower temperatures tend to reduce columnar growth and possibly surface roughness. However, temperature can affect the crystal structure or phase of the film. Depositions were attempted at different temperatures from room temperature to 750 °C. At temperatures below 500 °C no peaks were observed in the diffraction pattern. The film is likely polycrystalline with not preferred orientation. The

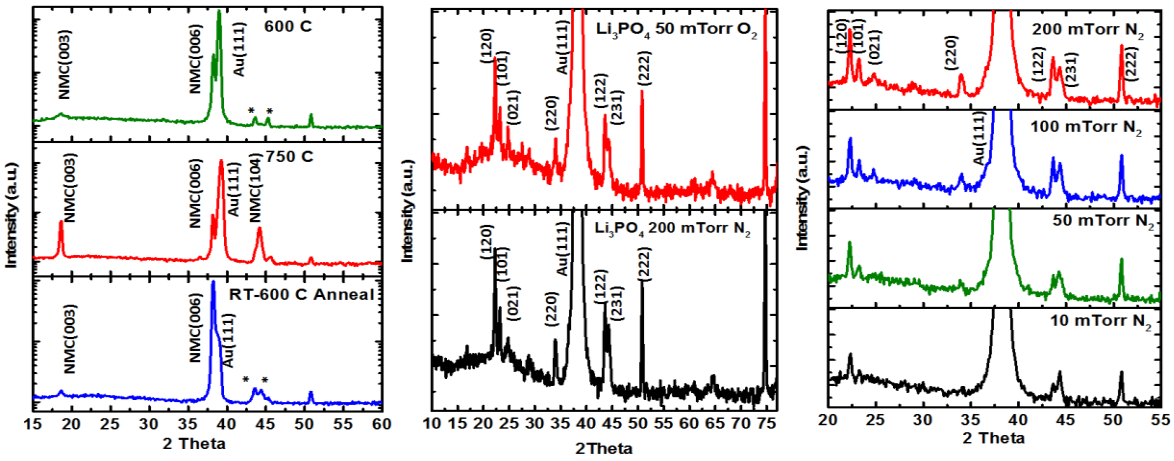

Figure 8.1. X-ray diffraction pattern of, (a) NMC Film deposited under different temperature condition, (b)Li_3PO_4 film deposited under oxygen and nitrogen ambient, (c) different nitrogen partial pressure.

XRD of films deposited at 600 °C, 750 °C and room temperature with 600 °C anneal is shown in figure 8. 1a. The sample deposited at 600 °C as well as the one deposited at room

temperature followed by 600 °C anneal show a peak split of the 104 peak. This likely indicates to lattice distortion leading to a super lattice or monoclinic structure as has been indicated in other layered Li oxides.[292, 293] Figure 8. 2a confirms that the film roughness is within acceptable limits for this recipe. The XRD patterns of the films deposited under different nitrogen partial is shown in figure 8. 1b. Diffraction patterns of thin films deposited under 50 mTorr of oxygen and nitrogen partial pressures respectively are compared in figure 8. 1b. The pattern concurs well with the expected pattern for γ-Li_3PO_4 (PDF #25-1030) and can be indexed as orthorhombic with *Pnma* symmetry. There is no significant difference between the films deposited under oxygen and nitrogen. The films are polycrystalline, although the weak peaks suggest that the reflections are due to small regions of polycrystalline films either at the interface or dispersed in the film. Successful doping of the Li_3PO_4 with nitrogen should lead to some structural changes. However, no peak shifts suggesting this is observed for the 50 mTorr Nitrogen sample. Kozen et al. recently reported amorphization of LiPON occurs for nitrogen content greater than 4.5%.[294] Based on this

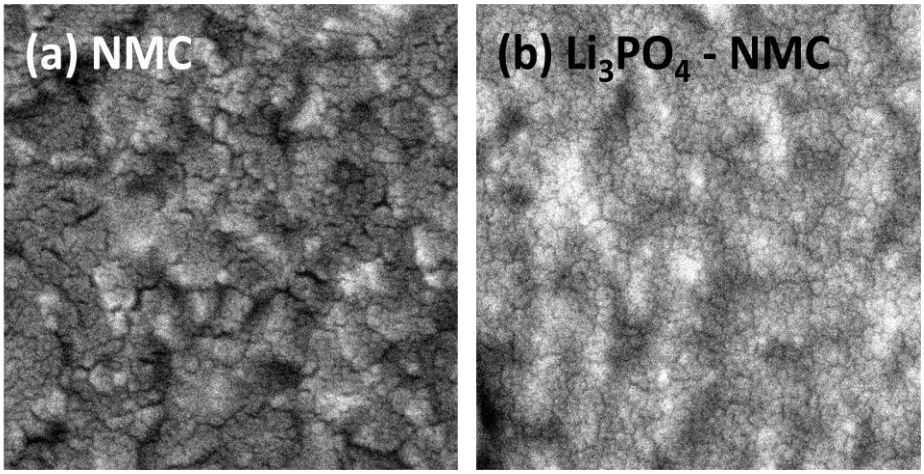

Figure 8.2. Scanning Electron Micrographs of, (a) bare NMC film and, (b) Li_3PO_4 coated NMC film.

observation, it is likely that no significant nitrogen doping was achieved at 50 mTorr. To further investigate this films were deposited under different nitrogen partial pressure. The corresponding patterns are shown in figure 8. 3c. The 120 peak shows a small shift with increasing nitrogen partial pressure. The crystal lattice expands with increase in deposition partial pressure, and is likely due to incorporation of nitrogen in the structure. Since the peak shift is small, this might indicate to very small amount of doping. The ratio of the (122) and (231) peaks changes with increased nitrogen partial pressure. This is either linked to lattice distortion due to nitrogen doping or Li stoichiometric variations due to higher partial pressure. Investigation is currently underway to understand this variation. Irrespective, lattice distortions and stoichiometric variations can potentially increase defects, which might promote Li conductions. It should be noted that Li deficiency can counter any such gain in ionic conductivity. These results will be further discussed in the context of the other measurements.

The SEM image in figure 8.2 shows the bare NMC film and the Li_3PO_4 coated sample. The NMC film was designed to be relatively smooth. The Li_3PO_4 coated samples is smoother and the coverage is fairly uniform. The electrolyte thickness was measured using a profilometer to be approximately 200 nm and is thought to provide good coverage. Composition analysis performed using wavelength dispersive spectroscopy indicate good stoichiometric match for the Li_3PO_4samples deposited under oxygen partial pressure. However, no significant nitrogen content was observed in the samples deposited under nitrogen ambient, with the nitrogen being less than 1%. This agrees well with the XRD patterns observed earlier. It is likely that even at 200 mTorr nitrogen pressure, not enough

nitrogen atoms dissociated into corresponding ions. This limits nitrogen doping in the film. High resolution STEM images of the film deposited on c-cut sapphire substrate, under 50 mTorr oxygen (a & b), and 200 mTorr nitrogen (c & d) is shown in figure 8. 3. Figure 8. 3a shows Li_3PO_4 electrolyte (O_2) deposited on NMC cathode film. Figure 8.3c shows Li_3PO_4 (N_2) electrolyte on NMC cathode film. Both films show dense electrode films coated by respective electrolytes. Figure 8. 3b shows a high magnification image of the indicated area for Li_3PO_4 film deposited under oxygen. The interface is clean and the NMC structure near the interface does not show significant damage. The inset shows the NMC film near the interface. The area further away from the electrolyte, indicated by the white arrow, shows continuous atomic row. The atomic planes represent the transition metal rows in the layered $R\bar{3}$m structure. The region closer to the electrolyte interface, indicated by the black arrow also shows continuous atomic rows.

However, more pronounced row of atoms is seen between the previously seen transition metal rows. This is likely due to presence of transition metal ions in the Li ion plane in a 10 Å thick layer at the electrolyte-electrode interface. Similar observations have been made in bulk electrode materials at grain boundaries. Figure 8.3d shows a magnified view of the NMC-Electrolyte interface for the nitrogen ambient case. The NMC film at the interface is highly distorted without continuous atomic planes as seen for the previous case. The inset shows an absence of layered structure at the interface. Further away from the interface weak layered structure is seen. The layered structure is responsible for the fast Li ion conduction in the cathode.

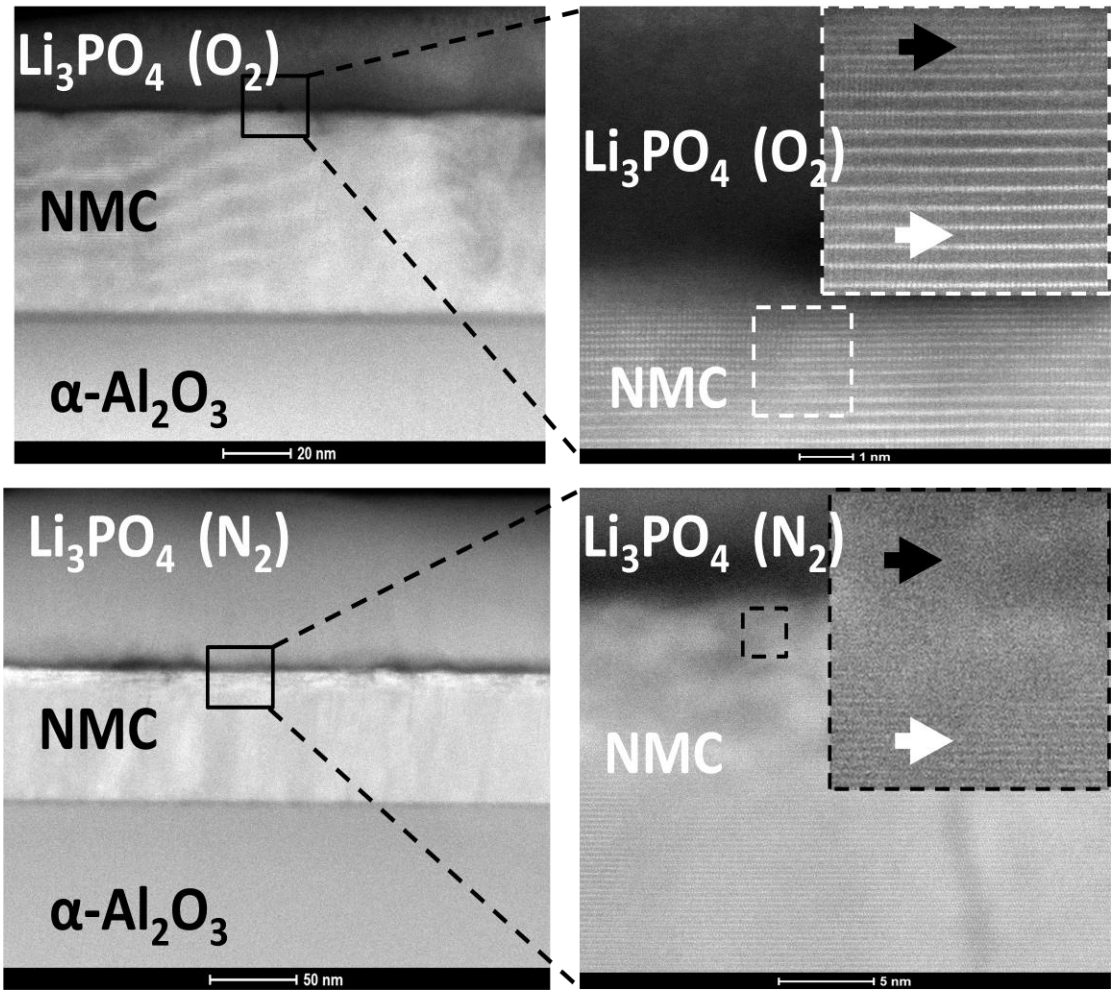

Figure 8.3. Low resolution STEM image of Li3PO4 film deposited on NMC film under, a) oxygen and, (c) nitrogen and the corresponding high resolution images, (b) and (d) respectively.

Electrochemical testing for the bare NMC, Li_3PO_4 and LiPON coated NMC were carried out to investigate the cycling and rate capability of the respective cathodes. The cycling performance of the cathodes is shown in figure 8. 4a. The bare NMC cathode initially shows a high capacity of 85 µAh. $\mu m^{-1}.cm^{-2}$. This then falls down to around 65 µAh. $\mu m^{-1}.cm^{-2}$ after 2 cycles. This can be attributed to the formation of a solid-electrolyte interface (SEI) layer.

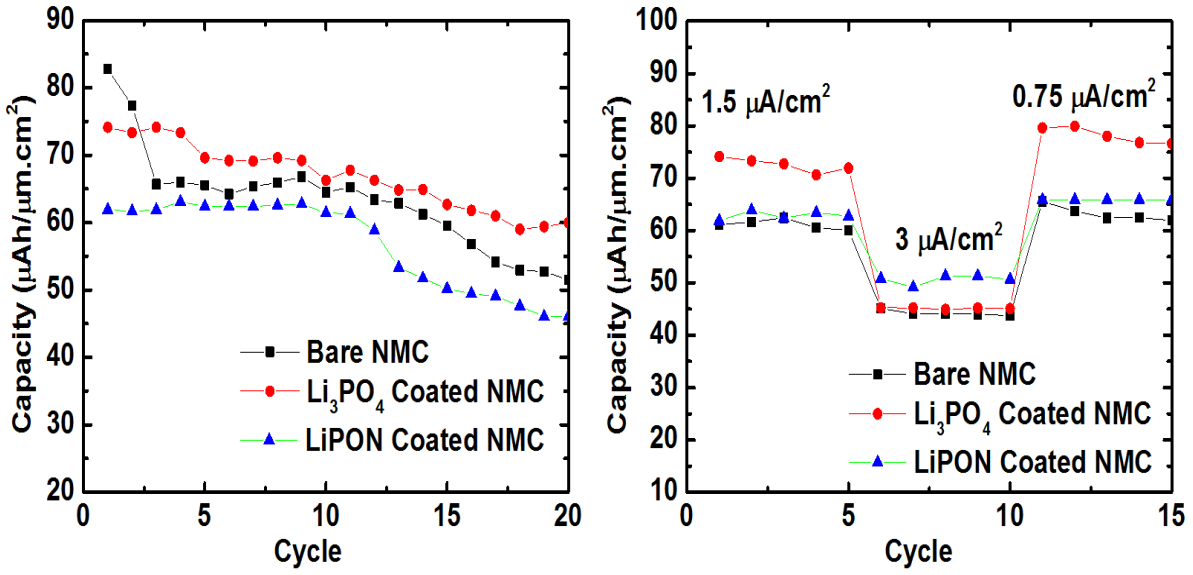

Figure 8.4. (a) Cycling performance and, (b) Rate capability of bare $Li(Ni_{0.5}Mn_{0.3}Co_{0.2})O_2$ (NMC), $Li_3PO_4(O_2)$, and $Li_3PO_4(N_2)$coated NMC cathodes.

Similar results were observed in case of bulk Li3PO4 coated LiNi0.5Mn1.5O4 powder synthesized by Chong and co workers[295]. The Li_3PO_4 and LiPON coated sample do not show this phenomenon indicating that the coating suppressed SEI layer formation and the associated irreversible capacity loss. This agrees well with observations by Chung et al., who speculated that solid electrolyte coating suppressed solvent decomposition at the electrode surface and hence reduces initial irreversible capacity loss.[296] Furthermore, it can be clearly seen that the Li_3PO_4 coated samples show a higher capacity compared to the bare NMC and LiPON coated samples.

It is likely that the PLD process has resulted in better interface between the NMC and Li_3PO_4. The high energy PLD process leads to highly energetic species, including ions, molecules and particulates. The ionic species are particularly energetic and would lead to defect formation due to back sputter of successive electrolyte film deposits. Li based

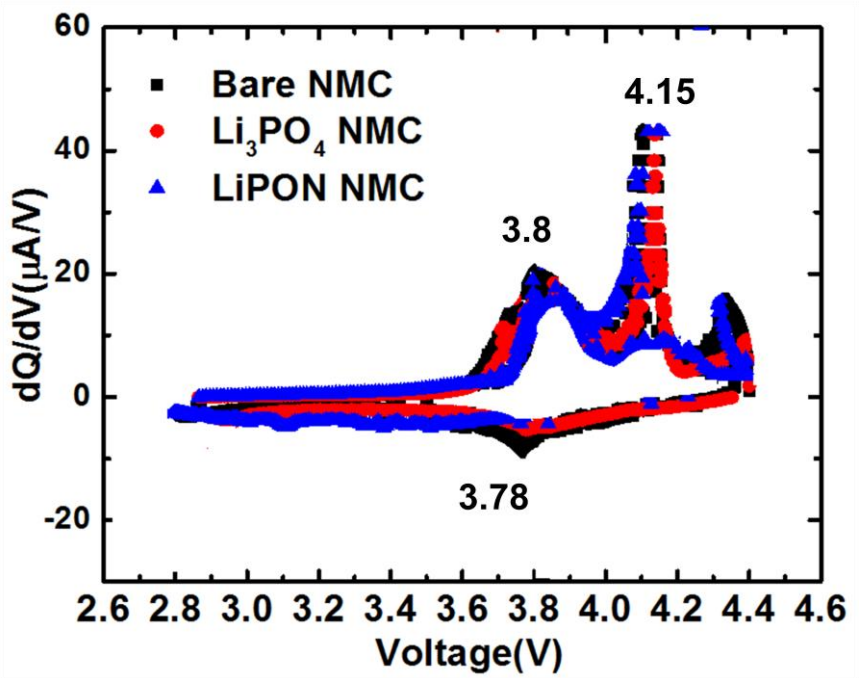

Figure 8.5. Cyclic Voltammetry of Bare $Li(Ni_{0.5}Mn_{0.3}Co_{0.2})O_2$ (NMC), Li_3PO_4 , and $Li_3PO_4(N_2)$ coated NMC Cathodes.

materials are more susceptible to this because of its lower melting point.[206] This agrees well with ab-initio simulation based predictions by Santosh et al that a high energy is required at the Li_3PO_4 interface to generate defects.[297]At the same time higher energy kinetics will also lead to better interface region. Iriyama and co-workers had earlier attempted to use thermal treatment after electrolyte deposition reduced the interfacial resistance between the electrode and electrolyte. While interfacial resistance reduced, the thermal treatment also increased the overall resistance because of annealing effect on the electrolyte.[291] The PLD process potentially improves the interface while at the same time modifies the deposited film to give a defect rich electrolyte. The Li_3PO_4 film deposited under nitrogen shows a much lower capacity in spite of the surface reaction suppression and advantages of the PLD process described above. Traditionally Li_3PO_4 target RF sputtered in

nitrogen ambient gives a LiPON film. LiPON has higher ionic conductivity than Li_3PO_4 and should give better electrochemical properties. However, as discussed above XRD and composition tests reveal that only limited nitrogen doping was achieved. This is likely due to the relatively low laser energy utilized in this work. Nitrogen dissociation requires higher energy compared to oxygen. Lower nitrogen ions in the plasma leads to reduced nitrogen incorporation, which limits associated improvements. Lower N incorporation in the film has been reported to reduce ionic conductivity in RF sputtered LiPON film.[289, 298]Moreover, the high nitrogen partial pressure (200 mTorr), will reduce the kinetic energy of the impinging ions reducing defect levels in the film. Another contributing factor can be inferred by comparing the interfacial micrographs of Li_3PO_4 deposited under oxygen and nitrogen partial pressure, shown in figure 8. 3. In the Li_3PO_4 (N_2) case, the NMC film at the interface shows a distorted structure. Since the electrolyte deposition was done at room temperature and at relatively low energy, process driven interface reaction is not very likely. None the less, since the plasma plume covers the substrate, it might promote a reaction. Brike and Weppner had reported that a change in oxidation state of phosphorus in RF sputtered thin film leading to increased reactivity of the deposited film.[299]Jacke and co-workers used XPS analysis to report a thin layer at the RF sputtered LIPON/$LiCoO_2$ interface, which they attributed to NO_3^- or NO_2^- radicals and proposed that this does not affect Li diffusion. However, no direct imaging results supporting this analysis were presented.[300]A high nitrogen partial pressure would have the twin effect of reducing Li and oxygen in the film in a pulsed laser deposition process.[206] This means that the film is not completely oxidized and can react with the NMC film. Layered transition metal cathodes belonging to $LiMO_2$

(M= Ni, Co, Mn), allow for fast Li transport along the parallel Li plane between the metal-oxygen planes The surface reactions will cause defects and block the Li transport. Thus while limited improvements has probably been achieved with nitrogen doping, the capacity is limited by other factors. Higher laser energy to increase nitrogen ionization in the plume along with nitrogen partial pressure optimization is likely to offset some of these limitations. An interlayer to protect the electrode film can also reduce the reaction at the interface. The rate capability of the cathodes is given in figure 8. 4b. At low to moderate discharge current the Li_3PO_4 shows superior capacity (80 $\mu Ah.\ \mu m^{-1}.cm^{-2}$) compared to bare NMC and LiPON coated cathodes. However at higher C-rates the LiPON coated sample perform better. This is most likely due the higher Li conductivity of nitrogen doped Li_3PO_4. These batteries still performs better then the bare NMC, again likely due to suppression of side reactions by the coating. Further investigation of the electrolyte coating was conducted using differential charging curves as shown in figure 8. 5. All films show similar cathodic peaks at 3.8 V and 4.15 V. These can be attributed to Ni^{2+}/Ni^{4+} and Co^{3+}/Co^{+4} redox reactions. No additional redox peaks are observed in the coated samples, indicating that the higher capacities observed in those cathodes resulted from the improved stability of the active NMC film rather than any direct electrochemical activity of the electrolyte or secondary impurity phases. It should be noted that after around 10 cycles the two redox peaks merge to form a single broad peak, centered around 3.9 V. The peak broadness can be attributed to polarization in the NMC thin film.

8.5 Conclusions

Li_3PO_4 solid electrolyte deposited under different oxygen and nitrogen partial pressure were investigated using pulsed laser deposition. $Li_3PO_4(O_2)$ films gave the best performance at low and moderate C-rates with a capacity of 80 µAh. $\mu m^{-1}.cm^{-2}$ observed at a current rate of 0.75µA.cm^{-2}. At a higher c- rate of 3µA. $cm^{-2}Li_3PO_4(N_2)$ coated samples displayed higher capacity, 55 µAh. $\mu m^{-1}.cm^{-2}$. The results prove the viability of using pulsed laser deposition to grow solid electrolyte and significantly improve performance of thin film cathodes. This work can next be extended to develop all solid-state battery using PLD.

CHAPTER IX

SUMMARY AND FUTURE WORK

This work explores next generation Li ion battery materials which are environmentally friendly, cost effective and significantly improve on the performance of current commercial materials. Several manganese based oxides and solid state electrolytes that meet these criteria were investigated. Thin film based techniques were developed to investigate different aspects of the materials as well as to enhance their properties.

9.1 Present Work

A majority of thin film techniques rely on epitaxial or high crystalline films. This is not possible with traditional thin film battery work which relies on low temperature deposition followed by annealing. Highly textured LiNiMnCoO2 (NMC) films were prepared using a one-step high temperature pulsed laser deposition without a separate post-anneal step. This was confirmed with XRD and TEM analysis. The thin film NMC cathode demonstrated an initial capacity of125mAhg^{-1} at 0.5C and retained 89% capacity after 100 cycles. Another manganese based material we investigated was Li_2MnO_3. In its native form Li_2MnO_3 is electrochemically inactive due to the +4 valence state of Mn. Acid etching to remove Li_2O from the oxide is known to activate it. A PLD process was developed to selectively remove Li and O in-situ with a simple thin film deposition process. Cathodes with a slight excess of Li and O deposited at 50 mTorr of oxygen partial pressure, showed

localized defects and gave an excellent capacity of 225 mAh g^{-1} at 0.05 C. On the other hand a large reduction in Li and O content leads to formation of MnO_2phase that gave a discharge capacity of 112 mAh g^{-1} after 30 cycles. It was demonstrated that thin film cathode growth technique can be applied to adjust the Li and O contents of the film independently to investigate various important mechanisms, including Li_2MnO_3 preactivation, modifying film kinetics, and investigating phase transformation like monoclinic to spinel phases.Another study investigated the behavior of Li_2MnO_3 in relation to stoichiometry when it was used as a standalone cathode and embedded in a NMC matrix. Surprisingly, it was found that the electrochemical performance of Li_2MnO_3 was better at moderate partial pressure of 50 mTorr while the Li rich cathodes gave the highest capacity at low oxygen partial pressure. Initial analysis indicates that the NMC matrix in the Li rich cathode stabilized the Li_2MnO_3 phase, suppressing irreversible structural changes. In the absence of such a framework pure Li_2MnO_3 showed lower capacity at low partial pressure.

A promising new class of Mn based cathode material; Li-rich metal oxidewas investigated. The structural complexity and limitation traditional solution based synthesis limits the understanding of this material. Questions like composition (single phase or two phases) and operation (reason for high capacity) is still being investigated by researchers. Model thin film cathodes were made to emulate both the single and two phase theories. The microstructural and electrochemical measurement results suggest that the mixed phase composites obtained are of comparable to those obtained via bulk synthesis techniques for similar stoichiometry. The model with distinct nano-domains of Li_2MnO_3, in a NMC matrix best matched the characteristic performance of the Li rich material. Having established the

domain nature of Li-rich cathodes, we next investigated the affects of composition variation and multilayer structure. The thin film cathodes were deposited by alternating between the targets and a pulse ratio of 50:50 gave the highest capacity. However, it was also shown that the nano-domain model demonstrate higher capacity compared to continuous multilayer structure. A combination of composition and microstructure can be used to tune the defects and conductivity of the cathodes. This thin film technique will allow for near independent optimization of composition and microstructure to optimize capacity of Li-rich cathodes.

Solid state batteries have become increasingly popular due to advantages like compact form factor, safety, and ability to integrate with electronic systems. Towards that end Li_3PO_4 solid electrolyte deposited under different oxygen and nitrogen partial pressure were investigated using pulsed laser deposition. $Li_3PO_4(O_2)$ films gave the best performance at low and moderate C-rates with a capacity of 80 µAh. $\mu m^{-1}.cm^{-2}$ observed at a current rate of 0.75µA.cm^{-2}. At a higher c- rate of 3µA. cm^{-2} $Li_3PO_4(N_2)$ coated samples displayed higher capacity, 55 µAh. $\mu m^{-1}.cm^{-2}$. The results prove the viability of using pulsed laser deposition to grow solid electrolyte and significantly improve performance of thin film cathodes. This work can next be extended to develop all solid-state battery using PLD.

9.2 Future Work

9.2.1 Correlations Between Thin and Thick Film Cathodes

As mentioned earlier, a majority of the research efforts in lithium ion battery is focused on bulk synthesis technique. This work hopes to bring a new set of diagnostic tools to help

improve existing and develop new materials. An important intermediatory step is to understand the differences and similarities between thin film and thick film electrodes. Based on our initial comparison between thin and thick films of NMC, it was determined that difference in conductivity and film density leads to problems like polarization. This leads to shifting of characteristics redox peaks and can potentially reduce obtainable capacity. Another likely problem is the variation of performance occurring due to film thickness of the thin film electrodes. Since conductivity, density etc. vary widely between different materials, a broad range of materials must be investigated to obtain generalized conclusion. We intend to carry out a systematic comparison between thin and thick film cathodes for different major classes of cathode material. We hope this study will bridge the gap between thin and thick film electrodes and allow other researchers to translate our thin film studies better to thick film cathode development.

9.2.2 Vertically Aligned Architecture for Li-rich Cathodes

A lot of next generation cathodes including $LiMPO_4$ (M =Co, Mn), Li_2MnO_3 etc. have poor electronic conductivity.[272] Attempts to overcome such limitations in bulk material research include doping[301, 302], or particle geometry[302, 303]. An alternate approach for thin film electrode is 3D architectures with a 3D current collector. However, instead of a template or lithography based technique[304, 305], which is both time consuming and expensive, we propose a self-assembled vertically aligned composite structures. These can be implemented as a VAN of a metal current collector and active electrode or the active electrode with solid state electrolyte. The metal/electrode architecture

will improve electronic conductivity through the metal pillars, and ionic conductivity via the interface region. The electrode/electrolyte VAN system will likewise improve ionic conductivity in the solid state battery by reducing the diffusion length between the electrode and electrolyte. Since the fabrication can be done in a single step as opposed to the photolithography or template based techniques, it is expected to be less expensive.

REFERENCES

1. Whittingham, M.S., *Lithium batteries and cathode materials.* Chemical Reviews, 2004. **104**(10): p. 4271-4301.
2. Tarascon, J.M. and M. Armand, *Issues and challenges facing rechargeable lithium batteries.* Nature, 2001. **414**(6861): p. 359-367.
3. Li, L., et al., *Degradation analysis of commercial lithium-ion batteries.* Xiandai Huagong/Modern Chemical Industry, 2006. **26**(SUPPL. 2): p. 204-206.
4. Han, X., et al., *A comparative study of commercial lithium ion battery cycle life in electric vehicle: Capacity loss estimation.* Journal of Power Sources, 2014. **268**: p. 658-669.
5. Chu, A. and P. Braatz, *Comparison of commercial supercapacitors and high-power lithium-ion batteries for power-assist applications in hybrid electric vehicles: I. Initial characterization.* Journal of Power Sources, 2002. **112**(1): p. 236-246.
6. Li, L., et al., *Electrochemical performance and EIS analysis of commercial lithium-ion battery.* Journal of Beijing Institute of Technology (English Edition), 2008. **17**(2): p. 222-226.
7. Han, S.W., et al., *Solid-state synthesis of Li4Ti5O12 for high power lithium ion battery applications.* Journal of Alloys and Compounds, 2013. **570**: p. 144-149.
8. Wang, X.Q., et al., *Synthesis and performance of LiFe0.9Ni0.1PO4 as cathode material in lithium-ion battery.* Zhongguo Youse Jinshu Xuebao/Chinese Journal of Nonferrous Metals, 2006. **16**(4): p. 739-745.

9. Li, J., et al., *Microwave solid-state synthesis of spinel Li4Ti5O12 nanocrystallites as anode material for lithium-ion batteries.* Solid state ionics, 2007. **178**(29-30): p. 1590-1594.

10. Bach, S., et al., *Sol-gel synthesis of manganese oxides.* Journal of Solid State Chemistry, 1990. **88**(2): p. 325-333.

11. Dominko, R., et al., *Wired porous cathode materials: A novel concept for synthesis of LiFePO4.* Chemistry of Materials, 2007. **19**(12): p. 2960-2969.

12. Manthiram, A. and J. Kim, *Low Temperature Synthesis of Insertion Oxides for Lithium Batteries.* Chemistry of Materials, 1998. **10**(10): p. 2895-2909.

13. Lin, C., et al., *Hydrogen peroxide assisted synthesis of LiNi1/3Co1/3Mn1/3O2 as high-performance cathode for lithium-ion batteries.* Journal of Power Sources, 2015. **280**: p. 263-271.

14. Fuller, T.F., M. Doyle, and J. Newman, *Simulation and optimization of the dual lithium ion insertion cell.* Journal of The Electrochemical Society, 1994. **141**(1): p. 1-10.

15. Gao, L., S. Liu, and R.A. Dougal, *Dynamic lithium-ion battery model for system simulation.* IEEE Transactions on Components and Packaging Technologies, 2002. **25**(3): p. 495-505.

16. Santhanagopalan, S., et al., *Review of models for predicting the cycling performance of lithium ion batteries.* Journal of Power Sources, 2006. **156**(2): p. 620-628.

17. Bates, J.B., et al., *Thin-film lithium and lithium-ion batteries.* Solid state ionics, 2000. **135**(1-4): p. 33-45.

18. Jung, Y.S., et al., *Enhanced stability of LiCoO2 cathodes in lithium-ion batteries using surface modification by atomic layer deposition.* Journal of The Electrochemical Society, 2010. **157**(1): p. A75-A81.

19. Abel, P.R., et al., *Improving the stability of nanostructured silicon thin film lithium-ion battery anodes through their controlled oxidation.* ACS Nano, 2012. **6**(3): p. 2506-2516.

20. Baggetto, L., et al., *On the electrochemistry of an anode stack for all-solid-state 3D-integrated batteries.* Journal of Power Sources, 2009. **189**(1): p. 402-410.

21. Schwenzel, J., V. Thangadurai, and W. Weppner, *Developments of high-voltage all-solid-state thin-film lithium ion batteries.* Journal of Power Sources, 2006. **154**(1): p. 232-238.

22. Liu, J., et al., *All-solid-state lithium ion battery: Research and industrial prospects.* Acta Chimica Sinica, 2013. **71**(6): p. 869-878.

23. Piccolino, M. and M. Bresadola, *Shocking frogs: Galvani, Volta, and the electric origins of neuroscience* 2013: Oxford University Press, USA.

24. Mertens, J., *Shocks and sparks: the voltaic pile as a demonstration device.* Isis, 1998: p. 300-311.

25. Bockris, J.O.M. and A.K. Reddy, *Modern electrochemistry: an introduction to an interdisciplinary area*2012: Springer Science & Business Media.

26. Daniel, C. and J.O. Besenhard, *Handbook of battery materials*2012: John Wiley & Sons.

27. Van Schalkwijk, W. and B. Scrosati, *Advances in lithium-ion batteries*2002: Springer Science & Business Media.

28. Barsukov, Y. and J. Qian, *Battery power management for portable devices*2013: Artech House.

29. Masaki, Y., J. Brodd Ralph, and K. Akiya, *Lithium-Ion Batteries, Science and Technologies*, 2009, Springer, New York.

30. Dell, R. and D.A.J. Rand, *Understanding batteries*2001: Royal Society of Chemistry.

31. Beck, F. and P. Rüetschi, *Rechargeable batteries with aqueous electrolytes.* Electrochimica Acta, 2000. **45**(15-16): p. 2467-2482.

32. Aifantis, K.E., S.A. Hackney, and R.V. Kumar, *High energy density lithium batteries: materials, engineering, applications*. 2010.

33. Powers, R.A., *Advances and trends in primary and small secondary batteries.* IEEE Aerospace and Electronic Systems Magazine, 1994. **9**(4): p. 32-36.

34. Rao, M.L.B.,Investigation of an alkaline electrolyte for Zn-PbO2 cells. Journal of The Electrochemical Society, 1973. **120**(7): p. 855-857.

35. Urfer, A., G.A. Lawrance, and D.A.J. Swinkels, *Measuring variation in EMD reduction with location in primary alkaline batteries.* Journal of Applied Electrochemistry, 1997. **27**(6): p. 667-672.

36. Battery Schematics, 2015; Available from: http://www.baj.or.jp/e/.

37. Holmes, L., *Lithium primary batteries: An expanding technology.* IEEE Review, 1980. **26**(8): p. 658-660.

38. Read, J., et al., *Low temperature performance of λ MnO2 in lithium primary batteries.* Electrochemical and Solid-State Letters, 2001. **4**(10): p. A162-A165.

39. Bullock, K.R., *Lead/acid batteries.* Journal of Power Sources, 1994. **51**(1): p. 1-17.

40. Dell, R.M., *Batteries -fifty years of materials development.* Solid state ionics, 2000. **134**(1-2): p. 139-158.

41. Ellis, S.R., et al., *The lead dioxide electrode.* Journal of Applied Electrochemistry, 1986. **16**(2): p. 159-167.

42. Linden, D., *Handbook of batteries and fuel cells.* New York, McGraw-Hill Book Co., 1984, 1075 p. No individual items are abstracted in this volume., 1984. **1**.

43. Shukla, A.K., S. Venugopalan, and B. Hariprakash, *Nickel-based rechargeable batteries.* Journal of Power Sources, 2001. **100**(1-2): p. 125-148.

44. Feng, F., M. Geng, and D.O. Northwood, *Electrochemical behaviour of intermetallic-based metal hydrides used in Ni/metal hydride (MH) batteries: A review.* International Journal of Hydrogen Energy, 2001. **26**(7): p. 725-734.

45. Taniguchi, A., et al., *Development of nickel/metal-hydride batteries for EVs and HEVs.* Journal of Power Sources, 2001. **100**(1-2): p. 117-124.

46. Sakai, T., I. Uehara, and H. Ishikawa, *R&D on metal hydride materials and Ni-MH batteries in Japan.* Journal of Alloys and Compounds, 1999. **293**: p. 762-769.

47. Yoshino, A., *The birth of the lithium-ion battery.* Angewandte Chemie - International Edition, 2012. **51**(24): p. 5798-5800.

48. Nelson, P., K. Bloom, and D. I Dees, *Modeling the performance and cost of lithium-ion batteries for electric-drive vehicles*, 2011, Argonne National Laboratory (ANL), Argonne, IL (United States).

49. Takada, K., *Progress and prospective of solid-state lithium batteries.* Acta Materialia, 2013. **61**(3): p. 759-770.

50. Dudney, N.J., *Solid-state thin-film rechargeable batteries.* Materials Science and Engineering B: Solid-State Materials for Advanced Technology, 2005. **116**(3 SPEC.ISS.): p. 245-249.

51. Ellis, B.L., K.T. Lee, and L.F. Nazar, *Positive electrode materials for Li-Ion and Li-batteries.* Chemistry of Materials, 2010. **22**(3): p. 691-714.

52. Gong, Z. and Y. Yang, *Recent advances in the research of polyanion-type cathode materials for Li-ion batteries.* Energy and Environmental Science, 2011. **4**(9): p. 3223-3242.

53. Kraytsberg, A., et al., *Higher, stronger, better ... A review of 5 volt cathode materials for advanced lithium-ion batteries.* Advanced Energy Materials, 2012. **2**(8): p. 922-939.

54. Goodenough, J.B. and Y. Kim, *Challenges for rechargeable Li batteries.* Chemistry of Materials, 2010. **22**(3): p. 587-603.

55. Liu, C., et al., *Advanced materials for energy storage.* Advanced Materials, 2010. **22**(8): p. E28-E62.

56. Etacheri, V., et al., *Challenges in the development of advanced Li-ion batteries: A review.* Energy and Environmental Science, 2011. **4**(9): p. 3243-3262.

57. McCreery, R.L., *Advanced carbon electrode materials for molecular electrochemistry.* Chemical Reviews, 2008. **108**(7): p. 2646-2687.

58. Zhang, W.J., *A review of the electrochemical performance of alloy anodes for lithium-ion batteries.* Journal of Power Sources, 2011. **196**(1): p. 13-24.

59. Deng, Y., et al., *Recent advances in Mn-based oxides as anode materials for lithium ion batteries.* RSC Advances, 2014. **4**(45): p. 23914-23935.

60. Wu, H.B., et al., *Nanostructured metal oxide-based materials as advanced anodes for lithium-ion batteries.* Nanoscale, 2012. **4**(8): p. 2526-2542.

61. Hayner, C.M., X. Zhao, and H.H. Kung, *Materials for rechargeable lithium-ion batteries.* Annual review of chemical and biomolecular engineering, 2012. **3**: p. 445-471.

62. Zhang, Q. and X. Li, *Recent developments in the doped-Li 4 Ti 5 O 12 anode materials of Lithium-ion batteries for improving the rate capability.* Int J Electrochem Sci, 2013. **8**: p. 6449-6456.

63. Park, C.-M., et al., *Li-alloy based anode materials for Li secondary batteries.* Chemical Society Reviews, 2010. **39**(8): p. 3115-3141.

64. Zhu, G.-N., Y.-G. Wang, and Y.-Y. Xia, *Ti-based compounds as anode materials for Li-ion batteries.* Energy & Environmental Science, 2012. **5**(5): p. 6652-6667.

65. Whittingham, M.S., *Lithium batteries and cathode materials.* Chemical Reviews, 2004. **104**(10): p. 4271-4302.

66. Whitfield, P., et al., *Investigation of possible superstructure and cation disorder in the lithium battery cathode material LiMn 1/3 Ni 1/3 Co 1/3 O 2 using neutron and anomalous dispersion powder diffraction.* Solid state ionics, 2005. **176**(5): p. 463-471.

67. Zheng, J., et al., *Mitigating voltage fade in cathode materials by improving the atomic level uniformity of elemental distribution.* Nano letters, 2014. **14**(5): p. 2628-2635.

68. Park, J.-K., *Principles and applications of lithium secondary batteries*2012: John Wiley & Sons.

69. He, P., et al., *Layered lithium transition metal oxide cathodes towards high energy lithium-ion batteries.* Journal of Materials Chemistry, 2012. **22**(9): p. 3680-3695.

70. Itou, Y. and Y. Ukyo, *Performance of LiNiCoO 2 materials for advanced lithium-ion batteries.* Journal of Power Sources, 2005. **146**(1): p. 39-44.

71. Kim, K.M., et al., *Capacity and cycle performance of a lithium-ion polymer battery using commercially available LiNiCoO2.* Journal of Power Sources, 2003. **123**(1): p. 69-74.

72. Doeff, M.M., T. Conry, and J. Wilcox. *Improved layered mixed transition metal oxides for Li-ion batteries*. in *Proceedings of SPIE - The International Society for Optical Engineering*. 2010.

73. Nayak, P.K., et al., *Multiphase LiNi0.33Mn0.54Co0.13O2 Cathode material with high capacity retention for Li-Ion batteries.* ChemElectroChem, 2015.

74. Wei, G., T.E. Haas, and R.B. Goldner. *Lithium cobalt oxide thin film and its electrochromism*. in *Proceedings - The Electrochemical Society*. 1989.

75. Wei, G., T.E. Haas, and R.B. Goldner, *Thin films of lithium cobalt oxide.* Solid state ionics, 1992. **58**(1-2): p. 115-122.

76. Bates, J.B., et al., *Thin-film rechargeable lithium batteries.* Journal of Power Sources, 1995. **54**(1): p. 58-62.

77. Antaya, M., et al., *In situ growth of layered, spinel, and rock-salt LiCoO2 by laser ablation deposition.* Journal of Applied Physics, 1994. **76**(5): p. 2799-2806.

78. Hart, F.X. and J.B. Bates, *Lattice model calculation of the strain energy density and other properties of crystalline LiCoO2.* Journal of Applied Physics, 1998. **83**(12): p. 7560-7566.

79. Morcrette, M., et al., *LiMn2O4 thin films for lithium ion sensors.* Solid state ionics, 1998. **112**(3-4): p. 249-254.

80. Rho, Y.H., K. Dokko, and K. Kanamura, *Li+ ion diffusion in LiMn2O4 thin film prepared by PVP sol-gel method.* Journal of Power Sources, 2006. **157**(1): p. 471-476.

81. Zhu, J., K. Zeng, and L. Lu, *Cycling effects on surface morphology, nanomechanical and interfacial reliability of LiMn2O4 cathode in thin film lithium ion batteries.* Electrochimica Acta, 2012. **68**: p. 52-59.

82. Mohamedi, M., et al., *Electrochemical investigation of LiNi0.5Mn1.5O4 thin film intercalation electrodes.* Electrochimica Acta, 2002. **48**(1): p. 79-84.

83. Deng, J., et al., *Electrochemical performance of LiNi 1/3Co 1/3Mn 1/3O 2 thin film electrodes prepared by pulsed laser deposition.* Journal of Power Sources, 2012. **217**: p. 491-497.

84. Jacob, C., et al., *Highly textured Li(Ni0.5Mn0.3Co0.2)O 2 thin films on stainless steel as cathode for lithium-ion battery.* Journal of Power Sources, 2013. **241**: p. 410-414.

85. Oh, Y., et al., *The enhancement of cycle-life performance in LiCoO2 thin film by partial Al2O3 coating.* Electronic Materials Letters, 2008. **4**(3): p. 103-105.

86. Lee, J.H. and K.J. Kim, *Superior electrochemical properties of porous Mn2O 3-coated LiMn2O4 thin-film cathodes for Li-ion microbatteries.* Electrochimica Acta, 2013. **102**: p. 196-201.

87. Schlom, D.G., et al., *A thin film approach to engineering functionality into oxides.* Journal of the American Ceramic Society, 2008. **91**(8): p. 2429-2454.

88. Clark, S.L. and P.T. Hammond, *Engineering the microfabrication of layer-by-layer thin films.* Advanced Materials, 1998. **10**(18): p. 1515-1519.

89. Sauvage, F., et al., *Factors affecting the electrochemical reactivity vs. lithium of carbon-free LiFePO4 thin films.* Journal of Power Sources, 2008. **175**(1): p. 495-501.

90. Xie, J., et al., *Li-ion diffusion kinetics in LiFePO4 thin film prepared by radio frequency magnetron sputtering.* Electrochimica Acta, 2009. **54**(20): p. 4631-4637.

91. Lu, Z.G., M.F. Lo, and C.Y. Chung, *Pulse laser deposition and electrochemical characterization of LiFePO 4-C composite thin films.* Journal of Physical Chemistry C, 2008. **112**(17): p. 7069-7078.

92. Lafont, U., et al., *Electrostatic spray pyrolysis of LiNi0.5Mn1.5O4 films for 3D Li-ion microbatteries.* Thin Solid Films, 2012. **520**(9): p. 3464-3471.

93. Yim, H., et al., *Three-dimensional hemisphere-structured LiSn0.0125Mn 1.975O4 thin-film cathodes.* Electrochemistry Communications, 2014. **43**: p. 36-39.

94. Tarascon, J.M., Journal of the Electrochemical Society 1991. **138**(10): p. 2859 - 2864.

95. Amatucci, G. and J.M. Tarascon, *Optimization of insertion compounds such as LiMn2O4 for Li-Ion batteries.* Journal of The Electrochemical Society, 2002. **149**(12): p. K31-K46.

96. Mukai, K., et al., *The gradient distribution of Ni ions in cation-disordered Li [Ni 1/2 Mn 3/2] O 4 clarified by muon-spin rotation and relaxation (μSR).* RSC Advances, 2013. **3**(29): p. 11634-11639.

97. HRTEM image 2015 [cited 2015; Available from: http://www.jfe-tec.co.jp/en/nano-c/.

98. Xia, Y., Y. Zhou, and M. Yoshio, *Capacity fading on cycling of 4 V Li/LiMn2 O 4 Cells.* Journal of The Electrochemical Society, 1997. **144**(8): p. 2593-2600.

99. Fu, L., et al., *Surface modifications of electrode materials for lithium ion batteries.* Solid State Sciences, 2006. **8**(2): p. 113-128.

100. Bates, J., et al., *Thin-film lithium and lithium-ion batteries.* Solid state ionics, 2000. **135**(1): p. 33-45.

101. Jacob, C., et al., *Electrochemical and structural effects of in situ Li2O extraction from Li2MnO3 for li-ion batteries.* ACS Applied Materials and Interfaces, 2015. **7**(4): p. 2433-2438.

102. Padhi, A.K., K.S. Nanjundaswamy, and J.B. Goodenough, *Phospho-olivines as positive-electrode materials for rechargeable lithium batteries.* Journal of The Electrochemical Society, 1997. **144**(4): p. 1188-1194.

103. Maxisch, T. and G. Ceder, *Elastic properties of olivine Li x FePO 4 from first principles.* Physical Review B, 2006. **73**(17): p. 174112.

104. Yuichi Ikuhara, N.S., Teruyasu Mizoguchi and Takashisa Yamamoto, *Interface Studies by Cs corrected STEM.* JEOL News, 2008. **43**(1): p. 2.

105. Morgan, D., A. Van der Ven, and G. Ceder, *Li Conductivity in LixMPO4 (M = Mn, Fe, Co, Ni) Olivine Materials.* Electrochemical and Solid-State Letters, 2004. **7**(2): p. A30-A32.

106. Song, S.W., et al., *Electrochemical studies of the LiFePO4 thin films prepared with pulsed laser deposition.* Journal of The Electrochemical Society, 2006. **153**(1): p. A12-A19.

107. Croce, F., et al., *A novel concept for the synthesis of an improved LiFePO4 lithium battery cathode.* Electrochemical and Solid-State Letters, 2002. **5**(3): p. A47-A50.

108. Hunter, J.C., *Preparation of a new crystal form of manganese dioxide: λ-MnO 2.* Journal of Solid State Chemistry, 1981. **39**(2): p. 142-147.

109. Thackeray, M.M., et al., *Li 2 MnO 3-stabilized LiMO 2 (M= Mn, Ni, Co) electrodes for lithium-ion batteries.* Journal of Materials Chemistry, 2007. **17**(30): p. 3112-3125.

110. Yu, H. and H. Zhou, *High-energy cathode materials (Li2MnO3–LiMO2) for lithium-ion batteries.* The Journal of Physical Chemistry Letters, 2013. **4**(8): p. 1268-1280.

111. Koga, H., et al., *Li1. 20Mn0. 54Co0. 13Ni0. 13O2 with different particle sizes as attractive positive electrode materials for lithium-ion batteries: insights into their structure.* The Journal of Physical Chemistry C, 2012. **116**(25): p. 13497-13506.

112. Ammundsen, B., et al., *Local structure and first cycle redox mechanism of layered Li1. 2Cr0. 4Mn0. 4 O 2 Cathode Material.* Journal of The Electrochemical Society, 2002. **149**(4): p. A431-A436.

113. Bareno, J., et al., *Long-range and local structure in the layered oxide Li1. 2Co0. 4Mn0. 4O2.* Chemistry of Materials, 2011. **23**(8): p. 2039-2050.

114. Bareno, J., et al., *Localstructure of layered oxide electrode materials for lithium-ion batteries.* Advanced Materials, 2010. **22**(10): p. 1122-1127.

115. Baggetto, L., et al., *Degradation mechanisms of lithium-rich nickel manganese cobalt oxide cathode thin films.* RSC Advances, 2014. **4**(45): p. 23364-23371.

116. Kuwabata, S., et al., *Electrochemical synthesis of composite films of manganese dioxide and polypyrrole and their properties as an active material in lithium secondary batteries.* Journal of The Electrochemical Society, 1994. **141**(1): p. 10-15.

117. Shao, L., J.W. Jeon, and J.L. Lutkenhaus, *Polyaniline nanofiber/vanadium pentoxide sprayed layer-by-layer electrodes for energy storage.* Journal of Materials Chemistry A, 2014. **2**(35): p. 14421-14428.

118. Jacob, C., et al., *A new approach to investigate Li2MnO3 and Li(Ni 0.5Mn0.3Co0.2)O2 mixed phase cathode materials.* Journal of Materials Chemistry A, 2014. **2**(7): p. 2283-2289.

119. Ellis, B.L., K.T. Lee, and L.F. Nazar, *Positive electrode materials for Li-ion and Li-batteries†.* Chemistry of Materials, 2010. **22**(3): p. 691-714.

120. Yang, H., et al., *A review of Li-Ion cell chemistries and their potential use in hybrid electric vehicles.* Journal of industrial and engineering chemistry, 2006. **12**(1): p. 12-38.

121. Liu, D., et al., *Spinel materials for high-voltage cathodes in Li-ion batteries.* RSC Advances, 2014. **4**(1): p. 154-167.

122. Santhanam, R. and B. Rambabu, *Research progress in high voltage spinel LiNi0.5Mn1.5O4 material.* Journal of Power Sources, 2010. **195**(17): p. 5442-5451.

123. Aurbach, D., et al., *Design of electrolyte solutions for Li and Li-ion batteries: a review.* Electrochimica Acta, 2004. **50**(2): p. 247-254.

124. Xu, K., *Nonaqueous liquid electrolytes for lithium-based rechargeable batteries.* Chemical Reviews, 2004. **104**(10): p. 4303-4418.

125. Mizuno, F., et al., *Rechargeable Li-air batteries with carbonate-based liquid electrolytes.* Electrochemistry, 2010. **78**(5): p. 403-405.

126. Ozawa, K., *Lithium Ion Rechargeable Batteries: Materials, Technology, and New Applications*, 2012: John Wiley & Sons.

127. Park, M., et al., *A review of conduction phenomena in Li-ion batteries.* Journal of Power Sources, 2010. **195**(24): p. 7904-7929.

128. Zhang, S.S., *A review on electrolyte additives for lithium-ion batteries.* Journal of Power Sources, 2006. **162**(2): p. 1379-1394.

129. Meyer, W.H., *Polymer electrolytes for lithium-ion batteries.* Advanced Materials, 1998. **10**(6): p. 439-448.

130. Wu, Y., *Lithium-Ion Batteries: Fundamentals and Applications*. Vol. 4. 2015: CRC Press.

131. Muldoon, J., et al., *Polymers: Opening Doors to Future Batteries.* Polymer Reviews, 2015. **55**(2): p. 208-246.

132. Quartarone, E. and P. Mustarelli, *Electrolytes for solid-state lithium rechargeable batteries: Recent advances and perspectives.* Chemical Society Reviews, 2011. **40**(5): p. 2525-2540.

133. Gellings, P.J. and H. Bouwmeester, *Handbook of solid state electrochemistry*1997: CRC press.

134. Dudney, N.J., W.C. West, and J. Nanda, *Handbook of solid state batteries*. Vol. 6. 2015: World Scientific.

135. Thangadurai, V., et al., *Fast solid-state Li ion conducting garnet-type structure metal oxides for energy storage.* Journal of Physical Chemistry Letters, 2015. **6**(2): p. 292-299.

136. Liu, H.C. and S.K. Yen, *Characterization of electrolytic Co3O4 thin films as anodes for lithium-ion batteries.* Journal of Power Sources, 2007. **166**(2): p. 478-484.

137. Baggetto, L., et al., *Fabrication and characterization of Li-Mn-Ni-O sputtered thin film high voltage cathodes for Li-ion batteries.* Journal of Power Sources, 2012. **211**: p. 108-118.

138. Xie, J., et al., *Kinetics investigation of a preferential (104) plane oriented LiCoO2 thin film prepared by RF magnetron sputtering.* Solid state ionics, 2007. **178**(19-20): p. 1218-1224.

139. Sauvage, F., et al., *Pulsed laser deposition and electrochemical properties of LiFePo 4 thin films.* Electrochemical and Solid-State Letters, 2004. **7**(1): p. A15-A18.

140. Kuwata, N., et al., *Thin film lithium ion batteries prepared only by pulsed laser deposition.* Solid state ionics, 2006. **177**(26-32 SPEC. ISS.): p. 2827-2832.

141. Hämäläinen, J., et al., *Lithium phosphate thin films grown by atomic layer deposition.* Journal of The Electrochemical Society, 2012. **159**(3): p. A259-A263.

142. Comstock, D.J. and J.W. Elam, *Mechanistic study of lithium aluminum oxide atomic layer deposition.* Journal of Physical Chemistry C, 2013. **117**(4): p. 1677-1683.

143. Donders, M.E., et al., *Atomic layer deposition of LiCoO2 thin-film electrodes for all-solid-state Li-ion micro-batteries.* Journal of The Electrochemical Society, 2013. **160**(5): p. A3066-A3071.

144. Gallasch, T., et al., *Ion beam sputter deposition of V2O5 thin films.* Journal of Power Sources, 2011. **196**(1): p. 428-435.

145. Morales, J., et al., *Use of low-temperature nanostructured CuO thin films deposited by spray-pyrolysis in lithium cells.* Thin Solid Films, 2005. **474**(1-2): p. 133-140.

146. Sato, H., et al., *Electrochemical characterization of thin-film LiCoO2 electrodes in propylene carbonate solutions.* Journal of Power Sources, 1997. **68**(2): p. 540-544.

147. Ma, J. and Q.Z. Qin, *Electrochemical performance of nanocrystalline LiMPO4 thin-films prepared by electrostatic spray deposition.* Journal of Power Sources, 2005. **148**(1-2): p. 66-71.

148. Chrisey, D.B. and G.K. Hubler, *Pulsed laser deposition of thin films.* 1994.

149. Granozio, F.M., et al. *In-situ investigation of surface oxygen vacancies in perovskites*. in *Materials Research Society Symposium Proceedings*. 2006.

150. Lippmaa, M., et al., *Growth mode mapping of SrTio3 epitaxy.* Applied Physics Letters, 2000. **76**(17): p. 2439-2441.

151. Singh, R.K. and J. Narayan, *Pulsed-laser evaporation technique for deposition of thin films: Physics and theoretical model.* Physical Review B, 1990. **41**(13): p. 8843-8859.

152. Wasa, K., *Handbook of sputter deposition technology: fundamentals and applications for functional thin films, nano-materials and MEMS* 2012: William Andrew.

153. Guinier, A., *X-ray diffraction in crystals, imperfect crystals, and amorphous bodies*1994: Courier Corporation.

154. Singh, A.K., *Advanced x-ray techniques in research and industry*2005: IOS Press.

155. Gauglitz, G. and D.S. Moore, *Handbook of Spectroscopy, 4 Volume Set*2014: John Wiley & Sons.

156. Egerton, R., *Physical principles of electron microscopy: an introduction to TEM, SEM, and AEM*2006: Springer Science & Business Media.

157. Julien, C.M., et al., *Comparative issues of cathode materials for Li-ion batteries.* inorganics, 2014. **2**(1): p. 132-154.

158. Dudney, N.J., *Solid-state thin-film rechargeable batteries.* Materials Science and Engineering: B, 2005. **116**(3): p. 245-249.

159. Golodnitsky, D., et al., *Progress in three-dimensional (3D) Li-ion microbatteries.* Solid state ionics, 2006. **177**(26): p. 2811-2819.

160. Patil, A., et al., *Issue and challenges facing rechargeable thin film lithium batteries.* Materials research bulletin, 2008. **43**(8): p. 1913-1942.

161. Dillon, S.J. and K. Sun, *Microstructural design considerations for Li-ion battery systems.* Current Opinion in Solid State and Materials Science, 2012. **16**(4): p. 153-162.

162. Ozawa, K., *Lithium-ion rechargeable batteries with LiCoO 2 and carbon electrodes: the LiCoO 2/C system.* Solid state ionics, 1994. **69**(3): p. 212-221.

163. Jung, Y.S. and A.S. Cavanagh, *b Anne C. Dillon, Markus D. Groner, Steven M. George, and Se-Hee Leea.* Journal of The Electrochemical Society, 2010. **157**(1): p. A75-A81.

164. Ruffo, R., et al., *Electrochemical behavior of LiCoO 2 as aqueous lithium-ion battery electrodes.* Electrochemistry Communications, 2009. **11**(2): p. 247-249.

165. Tarascon, J.-M. and M. Armand, *Issues and challenges facing rechargeable lithium batteries.* Nature, 2001. **414**(6861): p. 359-367.

166. Ohzuku, T. and Y. Makimura, *Layered lithium insertion material of LiCo1/3Ni1/3Mn1/3O2 for lithium-ion batteries.* Chemistry Letters, 2001(7): p. 642-643.

167. Lu, Z., D. MacNeil, and J. Dahn, *Layered Li [Ni x Co1− 2x Mn x] O 2 Cathode materials for lithium-ion batteries.* Electrochemical and Solid-State Letters, 2001. **4**(12): p. A200-A203.

168. Gao, J., J. Kim, and A. Manthiram, *High capacity Li [Li 0.2 Mn 0.54 Ni 0.13 Co 0.13] O 2–V 2 O 5 composite cathodes with low irreversible capacity loss for lithium ion batteries.* Electrochemistry Communications, 2009. **11**(1): p. 84-86.

169. Yu, H., et al., *High-energy 'composite'layered manganese-rich cathode materials via controlling Li 2 MnO 3 phase activation for lithium-ion batteries.* Physical Chemistry Chemical Physics, 2012. **14**(18): p. 6584-6595.

170. Amalraj, F., et al., *Synthesis of Integrated Cathode Materials xLi2MnO3·(1− x) LiMn1/3Ni1/3Co1/3O2 (x= 0.3, 0.5, 0.7) and Studies of Their Electrochemical Behavior*. Journal of The Electrochemical Society, 2010. **157**(10): p. A1121-A1130.

171. Ki-SooLi, S.-T.S., Yang-Kook Sun,, J. of Power Sources 2010(195): p. 6043.

172. Koenig Jr, G.M., et al., *Composition-tailored synthesis of gradient transition metal precursor particles for lithium-ion battery cathode materials.* Chemistry of Materials, 2011. **23**(7): p. 1954-1963.

173. Bates, J., et al., *Thin-film rechargeable lithium batteries.* Journal of Power Sources, 1995. **54**(1): p. 58-62.

174. Liao, C.-L. and K.-Z. Fung, *Lithium cobalt oxide cathode film prepared by rf sputtering.* Journal of Power Sources, 2004. **128**(2): p. 263-269.

175. Hong, J., et al., *Characterization and performance of LiFePO4 thin-film cathodes prepared with radio-frequency magnetron-sputter deposition.* Journal of The Electrochemical Society, 2007. **154**(8): p. A805-A809.

176. Shi, Q., et al., *High-capacity LiV 3 O 8 thin-film cathode with a mixed amorphous–nanocrystalline microstructure prepared by RF magnetron sputtering.* Electrochemistry Communications, 2009. **11**(11): p. 2169-2172.

177. Ding, J.-J., Q. Sun, and Z.-W. Fu, *Layered Li (Ni1/4Mn1/2Co13) O2 as cathode material for all-solid-state thin-film rechargeable lithium-ion batteries.* Electrochemical and Solid-State Letters, 2010. **13**(8): p. A105-A108.

178. Xie, J., et al., *Electrochemical kinetics of nanosized Ag and Ag2O thin films prepared by radio frequency magnetron sputtering.* Journal of Solid State Electrochemistry, 2011. **15**(9): p. 2031-2039.

179. Deng, J., et al., *Electrochemical performance of LiNi 1/3 Co 1/3 Mn 1/3 O 2 thin film electrodes prepared by pulsed laser deposition.* Journal of Power Sources, 2012. **217**: p. 491-497.

180. Bouwman, P., et al., *Structure-related intercalation behaviour of LiCoO 2 films.* Solid state ionics, 2002. **152**: p. 181-188.

181. Sauvage, F., et al., *Pulsed laser deposition and electrochemical properties of LiFePO4 thin films.* Electrochemical and Solid-State Letters, 2004. **7**(1): p. A15-A18.

182. Yamada, I., et al., *Lithium-ion transfer at LiMn 2 O 4 thin film electrode prepared by pulsed laser deposition.* Electrochemistry Communications, 2003. **5**(6): p. 502-505.

183. Kuwata, N., et al., *Thin film lithium ion batteries prepared only by pulsed laser deposition.* Solid state ionics, 2006. **177**(26): p. 2827-2832.

184. Xia, H., et al., *Phase transitions and high-voltage electrochemical behavior of LiCoO2 thin films grown by pulsed laser deposition.* Journal of The Electrochemical Society, 2007. **154**(4): p. A337-A342.

185. Rao, M., *Growth and microstructural features of laser ablated LiCoO 2 thin films.* Journal of Crystal Growth, 2010. **312**(19): p. 2799-2803.

186. Imanishi, N., et al., *Impedance analysis of PLD LiNi 0.8 Co 0.2 O 2 film electrode.* Journal of Power Sources, 2007. **174**(2): p. 751-755.

187. Matsumura, T., et al., *Electrochemical performances for preferred oriented PLD thin-film electrodes of LiNi 0.8 Co 0.2 O 2, LiFePO 4 and LiMn 2 O 4.* Solid state ionics, 2008. **179**(35): p. 2011-2015.

188. Dumont, T., et al., *Influence of experimental parameter on the Li-content of LiMn 2 O 4 electrodes produced by pulsed laser deposition.* Applied surface science, 2006. **252**(13): p. 4902-4906.

189. Xia, H., L. Lu, and Y.S. Meng, *Growth of layered LiNi0. 5Mn0. 5O2 thin films by pulsed laser deposition for application in microbatteries.* Applied Physics Letters, 2008. **92**(1): p. 011912.

190. Whitacre, J., et al., *Crystallographically oriented thin-film nanocrystalline cathode layers prepared without exceeding 300 C.* Journal of The Electrochemical Society, 2001. **148**(10): p. A1078-A1084.

191. Shaju, K., G.S. Rao, and B. Chowdari, *Performance of layered Li (Ni 1/3 Co 1/3 Mn 1/3) O 2 as cathode for Li-ion batteries.* Electrochimica Acta, 2002. **48**(2): p. 145-151.

192. Kim, Y.J., et al., *Changes in the lattice constants of thin-film LiCoO2 cathodes at the 4.2 V charged state.* Journal of The Electrochemical Society, 2004. **151**(7): p. A1063-A1067.

193. Goodenough, J.B. and K.-S. Park, *The Li-ion rechargeable battery: a perspective.* Journal of the American Chemical Society, 2013. **135**(4): p. 1167-1176.

194. Bruce, P., A. áRobert Armstrong, and R. Gitzendanner, *New intercalation compounds for lithium batteries: layered LiMnO2.* Journal of Materials Chemistry, 1999. **9**(1): p. 193-198.

195. Shaju, K.M. and P.G. Bruce, *A stoichiometric nano-LiMn2O4 spinel electrode exhibiting high power and stable cycling.* Chemistry of Materials, 2008. **20**(17): p. 5557-5562.

196. Lanz, P., C. Villevieille, and P. Novák, *Electrochemical activation of Li 2 MnO 3 at elevated temperature investigated by in situ Raman microscopy.* Electrochimica Acta, 2013. **109**: p. 426-432.

197. Yabuuchi, N., et al., *Detailed studies of a high-capacity electrode material for rechargeable batteries, Li2MnO3− LiCo1/3Ni1/3Mn1/3O2.* Journal of the American Chemical Society, 2011. **133**(12): p. 4404-4419.

198. Kalyani, P., et al., *Lithium metal rechargeable cells using Li2MnO3 as the positive electrode.* Journal of Power Sources, 1999. **80**(1): p. 103-106.

199. Gao, Y., et al., *Improved electron/Li-ion transport and oxygen stability of Mo-doped Li 2 MnO 3.* Journal of Materials Chemistry A, 2014. **2**(13): p. 4811-4818.

200. Rana, J., et al., *Structural changes in Li2MnO3 cathode material for Li-Ion batteries.* Advanced Energy Materials, 2014. **4**(5).

201. Lee, E. and K.A. Persson, *Structural and chemical evolution of the layered Li-excess LixMnO3 as a function of Li content from first-principles calculations.* Advanced Energy Materials, 2014. **4**(15).

202. Ruprecht, B., et al., *Extremely slow Li ion dynamics in monoclinic Li2TiO3—probing macroscopic jump diffusion via 7 Li NMR stimulated echoes.* Physical Chemistry Chemical Physics, 2012. **14**(34): p. 11974-11980.

203. Fehr, T. and E. Schmidbauer, *Electrical conductivity of Li2TiO3 ceramics.* Solid state ionics, 2007. **178**(1): p. 35-41.

204. Abouimrane, A., et al., *Improved rate capability in a high-capacity layered cathode material via thermal reduction.* Electrochemical and Solid-State Letters, 2011. **14**(9): p. A126-A129.

205. Qiu, B., et al., *Enhanced electrochemical performance with surface coating by reactive magnetron sputtering on Lithium-rich layered oxide electrodes.* ACS Applied Materials & Interfaces, 2014. **6**(12): p. 9185-9193.

206. Jacob, C., et al., *Highly textured Li (Ni 0.5Mn0.3Co0.2) O 2 thin films on stainless steel as cathode for lithium-ion battery*. Journal of Power Sources, 2013. **241**: p. 410-414.

207. Jacob, C., et al., *A new approach to investigate Li2MnO3 and Li(Ni0.5Mn0.3Co02)O2 mixed phase cathode materials.* Journal of Materials Chemistry A, 2014. **2**(7): p. 2283-2289.

208. Hy, S., et al., *Direct In situ observation of Li2O evolution on Li-Rich high-capacity cathode material, Li [Ni x Li (1–2 x)/3Mn (2–x)/3] O2 (0≤ x≤ 0.5).* Journal of the American Chemical Society, 2014. **136**(3): p. 999-1007.

209. Ohzuku, T., et al., *High-capacity lithium insertion materials of lithium nickel manganese oxides for advanced lithium-ion batteries: toward rechargeable capacity*

more than 300 mA hg− 1. Journal of Materials Chemistry, 2011. **21**(27): p. 10179-10188.

210. Rossouw, M. and M. Thackeray, *Lithium manganese oxides from Li 2 MnO 3 for rechargeable lithium battery applications.* Materials research bulletin, 1991. **26**(6): p. 463-473.

211. Wu, X., et al., *Facile synthesis of Li 2 MnO 3 nanowires for lithium-ion battery cathodes.* New Journal of Chemistry, 2014. **38**(2): p. 584-587.

212. Amalraj, F., et al., *Studies of Li and Mn-Rich Lix [MnNiCo] O2 Electrodes: Electrochemical Performance, Structure, and the Effect of the Aluminum Fluoride Coating.* Journal of The Electrochemical Society, 2013. **160**(11): p. A2220-A2233.

213. Shao-Horn, Y., et al., *Morphology Modification and Delithiation Mechanisms of LiMn2 O 4 and Li2MnO3 by Acid Digestion.* Journal of The Electrochemical Society, 1998. **145**(1): p. 16-23.

214. Tompsett, D.A. and M.S. Islam, *Electrochemistry of hollandite α-MnO2: Li-ion and Na-ion insertion and Li2O incorporation.* Chemistry of Materials, 2013. **25**(12): p. 2515-2526.

215. Johnson, C., et al., *Stabilized alpha-MnO2 electrodes for rechargeable 3 V lithium batteries.* Journal of The Electrochemical Society, 1997. **144**(7): p. 2279-2283.

216. Johnson, C.S., et al., *Synthesis, characterization and electrochemistry of lithium battery electrodes: x Li2MnO3·(1− x) LiMn0. 333Ni0. 333Co0. 333O2 (0≤ x≤ 0.7).* Chemistry of Materials, 2008. **20**(19): p. 6095-6106.

217. Kim, J.S., C.S. Johnson, and M.M. Thackeray, *Layered xLiMO2 · (1 - x)Li2M'O3 electrodes for lithium batteries: A study of 0.95LiMn0.5Ni0.5O2 · 0.05Li2TiO3.* Electrochemistry Communications, 2002. **4**(3): p. 205-209.

218. Kim, J.S., et al., *Electrochemical and structural properties of xLi2M'O 3·(1-x)LiMn0.5Ni0.5O2 electrodes for lithium batteries (M' = Ti, Mn, Zr; O ≤ x ≤ 0.3).* Chemistry of Materials, 2004. **16**(10): p. 1996-2006.

219. Thackeray, M.M., et al., *Li2MnO3-stabilized LiMO2 (M = Mn, Ni, Co) electrodes for lithium-ion batteries.* Journal of Materials Chemistry, 2007. **17**(30): p. 3112-3125.

220. Croy, J.R., et al., *Li2MnO3-based composite cathodes for lithium batteries: A novel synthesis approach and new structures.* Electrochemistry Communications, 2011. **13**(10): p. 1063-1066.

221. Ito, A., et al., *Cyclic deterioration and its improvement for Li-rich layered cathode material Li[Ni0.17Li0.2Co0.07Mn0.56]O2.* Journal of Power Sources, 2010. **195**(2): p. 567-573.

222. Xiang, Y., et al., *Effects of synthesis conditions on the structural and electrochemical properties of the Li-rich material Li[Li0.2Ni0.17Co0.16Mn0.47]O2 via the solid-state method.* Electrochimica Acta, 2013. **91**(0): p. 214-218.

223. Yabuuchi, N., et al., *Detailed studies of a high-capacity electrode material for rechargeable batteries, Li2MnO3−LiCo1/3Ni1/3Mn1/3O2.* Journal of the American Chemical Society, 2011. **133**(12): p. 4404-4419.

224. Lim, J.-H., et al., *Electrochemical characterization of Li2MnO3–Li[Ni1/3Co1/3Mn1/3]O2–LiNiO2 cathode synthesized via co-precipitation for lithium secondary batteries.* Journal of Power Sources, 2009. **189**(1): p. 571-575.

225. Zhang, X., et al., *Self-adjusted oxygen-partial-pressure approach to the improved electrochemical performance of electrode Li [Li0. 14Mn0. 47Ni0. 25Co0. 14] O2 for lithium-ion batteries.* J. Mater. Chem. A, 2013.

226. Jiang, K.-C., et al., *Superior hybrid cathode material containing lithium-excess layered material and graphene for Lithium-Ion Batteries.* ACS Applied Materials & Interfaces, 2012. **4**(9): p. 4858-4863.

227. Shojan, J., et al., *Lithium-ion battery performance of layered 0.3Li2MnO3–0.7LiNi0.5Mn0.5O2 composite cathode prepared by co-precipitation and sol–gel methods.* Materials Letters, 2013. **104**(0): p. 57-60.

228. Bareño, J., et al., *Long-Range and local structure in the layered oxide Li1.2Co0.4Mn0.4O2.* Chemistry of Materials, 2011. **23**(8): p. 2039-2050.

229. Jarvis, K.A., et al., *Atomic structure of a lithium-rich layered oxide material for lithium-ion batteries: evidence of a solid solution.* Chemistry of Materials, 2011. **23**(16): p. 3614-3621.

230. Xiao, J., N.A. Chernova, and M.S. Whittingham, *Influence of manganese content on the performance of LiNi0.9−yMnyCo0.1O2 (0.45 ≤ y ≤ 0.60) as a cathode material for Li-Ion batteries†.* Chemistry of Materials, 2009. **22**(3): p. 1180-1185.

231. Park, S., et al., *Cycle mechanism and electrochemical properties of lithium manganese oxide prepared using different Mn sources.* Materials Chemistry and Physics, 2008. **112**(2): p. 696-701.

232. Denis, Y., et al., *Electrochemical activities in Li2MnO3.* Journal of The Electrochemical Society, 2009. **156**(6): p. A417-A424.

233. Amalraj, S.F., et al., *Study of the nanosized Li2MnO3: electrochemical behavior, structure, magnetic properties, and vibrational modes.* Electrochimica Acta, 2013. **97**(0): p. 259-270.

234. Wang, J., et al., *Electrochemical properties of 0.6Li[Li1/3Mn2/3]O2–0.4LiNixMnyCo1−x−yO2 cathode materials for lithium-ion batteries.* Journal of Power Sources, 2012. **218**(0): p. 128-133.

235. Zhang, X., et al., *Novel composites Li[LixNi0.34−xMn0.47Co0.19]O2 (0.18≤ x ≤ 0.21): Synthesis and application as high-voltage cathode with improved electrochemical performance for lithium ion batteries.* Electrochimica Acta, 2012. **81**(0): p. 233-238.

236. Jacob, C., et al., *Highly textured Li (Ni 0.5 Mn 0.3 Co 0.2) O 2 thin films on stainless steel as cathode for lithium-ion battery.* Journal of Power Sources, 2013.

237. Wang, H., et al., *Microstructure of SrTiO3 buffer layers and itseffects on superconducting properties of YBa2Cu3O7-δ coated conductors.* Journal of materials research, 2004. **19**(06): p. 1869-1875.

238. Roberge, G., et al., *Improving the growth of electron-doped Pr2− xCexCuO4+ δ thin films made by pulsed-laser deposition using excess CuO.* Journal of Crystal Growth, 2009. **311**(5): p. 1340-1345.

239. Yun, J.-G., et al., *Selective growth of pure magnetite thin films and/or nanowires grown in situ at a low temperature by pulsed laser deposition.* Journal of Materials Chemistry C, 2013. **1**(10): p. 1977-1982.

240. Zhou, Y., et al., *Microstructure and surface morphology evolution of pulsed laser deposited piezoelectric BaTiO3 films.* J. Mater. Chem. C, 2013.

241. Franklin, J., et al., *Optimised pulsed laser deposition of ZnO thin films on transparent conducting substrates.* Journal of Materials Chemistry, 2011. **21**(22): p. 8178-8182.

242. Iriyama, Y., et al., *Preparation of c-axis oriented thin films of LiCoO 2 by pulsed laser deposition and their electrochemical properties.* Journal of Power Sources, 2001. **94**(2): p. 175-182.

243. Xia, H., L. Lu, and G. Ceder, *Li diffusion in LiCoO 2 thin films prepared by pulsed laser deposition.* Journal of Power Sources, 2006. **159**(2): p. 1422-1427.

244. Iriyama, Y., et al., *Preparation of LiFePO4 thin films by pulsed laser deposition and their electrochemical properties.* Electrochemical and solid-state letters, 2004. **7**(10): p. A340-A342.

245. Song, S.-W., et al., *Electrochemical studies of the LiFePO4 thin films prepared with pulsed laser deposition.* Journal of The Electrochemical Society, 2006. **153**(1): p. A12-A19.

246. Matsumura, T., et al., *Electrochemical performances for preferred oriented PLD thin-film electrodes of LiNi 0.8 Co 0.2 O 2, LiFePO 4 and LiMn 2 O 4.* Solid state ionics, 2008. **179**(35): p. 2011-2015.

247. Zhang, X., et al., *Minimization of the cation mixing in Li1+x(NMC)1−xO2 as cathode material.* Journal of Power Sources, 2010. **195**(5): p. 1292-1301.

248. Nathan, M., et al., *Three-dimensional thin-film Li-ion microbatteries for autonomous MEMS.* Microelectromechanical Systems, Journal of, 2005. **14**(5): p. 879-885.

249. Lethien, C., et al., *Micro-patterning of LiPON and lithium iron phosphate material deposited onto silicon nanopillars array for lithium ion solid state 3D micro-battery.* Microelectronic engineering, 2011. **88**(10): p. 3172-3177.

250. Oudenhoven, J.F., L. Baggetto, and P.H. Notten, *All-solid-state lithium-ion microbatteries: A review of various three-dimensional concepts.* Advanced Energy Materials, 2011. **1**(1): p. 10-33.

251. Antaya, M., et al., *In situ growth of layered, spinel, and rock-salt LiCoO2 by laser ablation deposition.* Journal of Applied Physics, 1994. **76**(5): p. 2799-2806.

252. Rho, Y.H., K. Kanamura, and T. Umegaki, *LiCoO2 and LiMn2 O 4 Thin-film electrodes for rechargeable lithium batteries preparation using PVP Sol-Gel to produce excellent electrochemical properties.* Journal of The Electrochemical Society, 2003. **150**(1): p. A107-A111.

253. Tang, S., M. Lai, and L. Lu, *Li-ion diffusion in highly (003) oriented LiCoO 2 thin film cathode prepared by pulsed laser deposition.* Journal of Alloys and Compounds, 2008. **449**(1): p. 300-303.

254. Hwang, B.-J., et al., *Structure, Morphology, and electrochemical investigation of LiMn2O4 thin film cathodes deposited by radio frequency sputtering for lithium microbatteries.* The Journal of Physical Chemistry C, 2009. **113**(26): p. 11373-11380.

255. Zhu, X.-J., et al., *Preparation and characteristics of LiFePO4 thin film by radio frequency magnetron sputtering for lithium microbatteries.* The Journal of Physical Chemistry C, 2009. **113**(32): p. 14518-14522.

256. Rosaiah, P. and O. Hussain, *Microstructural and electrochemical properties of rf-sputtered LiFePO4 thin films.* Ionics, 2014. **20**(8): p. 1095-1101.

257. Yoon, Y., et al., *Lattice orientation control of lithium cobalt oxide cathode film for all-solid-state thin film batteries.* Journal of Power Sources, 2013. **226**: p. 186-190.

258. Cotte, S., et al., *Lithium-rich manganese oxide spinel thin films as 3V electrode for lithium batteries.* Electrochimica Acta, 2015. **180**: p. 528-534.

259. Cho, J., et al., *Zero-strain intercalation cathode for rechargeable Li-Ion cell.* Angewandte Chemie, 2001. **113**(18): p. 3471-3473.

260. Xia, H., L. Lu, and G. Ceder, *Substrate effect on the microstructure and electrochemical properties of LiCoO 2 thin films grown by PLD.* Journal of Alloys and Compounds, 2006. **417**(1): p. 304-310.

261. Kim, J.-B., B.-S. Jun, and S.-M. Lee, *Improvement of capacity and cyclability of Fe/Si multilayer thin film anodes for lithium rechargeable batteries.* Electrochimica Acta, 2005. **50**(16): p. 3390-3394.

262. Ito, A., et al., *Cyclic deterioration and its improvement for Li-rich layered cathode material Li [Ni 0.17 Li 0.2 Co 0.07 Mn 0.56] O 2.* Journal of Power Sources, 2010. **195**(2): p. 567-573.

263. Lim, J.-H., et al., *Electrochemical characterization of Li 2 MnO 3–Li [Ni 1/3 Co 1/3 Mn 1/3] O 2–LiNiO 2 cathode synthesized via co-precipitation for lithium secondary batteries.* Journal of Power Sources, 2009. **189**(1): p. 571-575.

264. Shojan, J., et al., *Lithium-ion battery performance of layered 0.3 Li 2 MnO 3–0.7 LiNi 0.5 Mn 0.5 O 2 composite cathode prepared by co-precipitation and sol–gel methods.* Materials Letters, 2013. **104**: p. 57-60.

265. Wu, F., et al., *Preparation and electrochemical performance of Li-rich layered cathode material, Li [Ni0. 2Li0. 2Mn0. 6] O2, for lithium-ion batteries.* Journal of Applied Electrochemistry, 2010. **40**(4): p. 783-789.

266. Yan, B., et al., *Li-rich thin film cathode prepared by pulsed laser deposition.* Scientific reports, 2013. **3**.

267. Kubota, K., et al., *Direct synthesis of oxygen-deficient Li 2 MnO 3− x for high capacity lithium battery electrodes.* Journal of Power Sources, 2012. **216**: p. 249-255.

268. Pasero, D., et al., *Oxygen nonstoichiometry in Li2MnO3: An alternative explanation for its anomalous electrochemical activity.* Chemistry of Materials, 2005. **17**(2): p. 345-348.

269. Rao, K.Y., et al., *Sputter deposited high capacity Li2-xMnO3-y films for thin film battery application.* Journal of The Electrochemical Society, 2014. **161**(1): p. A28-A32.

270. Arthur, T.S., et al., *Three-dimensional electrodes and battery architectures.* Mrs Bulletin, 2011. **36**(07): p. 523-531.

271. Wang, R., et al., *Atomic structure of Li2MnO3 after partial delithiation and re-lithiation.* Advanced Energy Materials, 2013. **3**(10): p. 1358-1367.

272. Cheng, M., et al., *Electrochemical properties of Li 2 MnO 3 nanocrystals synthesized using a hydrothermal method.* RSC Advances, 2015. **5**(87): p. 71088-71094.

273. Noh, J.-K., et al., *Mechanochemical synthesis of Li2MnO3 shell/LiMO2 (M= Ni, Co, Mn) core-structured nanocomposites for lithium-ion batteries.* Scientific reports, 2014. **4**.

274. Scrosati, B., J. Hassoun, and Y.K. Sun, *Lithium-ion batteries. A look into the future.* Energy and Environmental Science, 2011. **4**(9): p. 3287-3295.

275. Scrosati, B., *Challenge of portable power.* Nature, 1995. **373**(6515): p. 557-558.

276. Machida, N., *Development of materials for all-solid-state lithium batteries.* Funtai Oyobi Fummatsu Yakin/Journal of the Japan Society of Powder and Powder Metallurgy, 2005. **52**(8): p. 589-598.

277. Balkanski, M., *Solid-state microbatteries for electronics in the 21st century.* Solar energy materials and solar cells, 2000. **62**(1): p. 21-35.

278. Sridhara, S.R., et al., *Microwatt embedded processor platform for medical system-on-chip applications.* Solid-State Circuits, IEEE Journal of, 2011. **46**(4): p. 721-730.

279. West, W., et al., *Fabrication and testing of all solid-state microscale lithium batteries for microspacecraft applications.* Journal of Micromechanics and Microengineering, 2002. **12**(1): p. 58.

280. Owens, B.B., *Solid state electrolytes: overview of materials and applications during the last third of the twentieth century.* Journal of Power Sources, 2000. **90**(1): p. 2-8.

281. Bates, J.B., et al., *Electrical properties of amorphous lithium electrolyte thin films.* Solid state ionics, 1992. **53-56**(PART 1): p. 647-654.

282. Unuma, H., K. Komori, and S. Sakka, *Electrical conductivity and chemical durability in alkali-silicate oxynitride glasses.* Journal of Non-Crystalline Solids, 1987. **95**: p. 913-920.

283. Muñoz, F., et al., *Alkali and alkali–lead oxynitride phosphate glasses: a comparative structural study by NMR and XPS.* Comptes Rendus Chimie, 2002. **5**(11): p. 731-738.

284. Marchand, R., et al., *Characterization of nitrogen containing phosphate glasses by X-ray photoelectron spectroscopy.* Journal of Non-Crystalline Solids, 1988. **103**(1): p. 35-44.

285. Muñoz, F., et al., *Increased electrical conductivity of LiPON glasses produced by ammonolysis.* Solid state ionics, 2008. **179**(15): p. 574-579.

286. Unuma, H. and S. Sakka, *Electrical conductivity in Na-Si-ON oxynitride glasses.* Journal of materials science letters, 1987. **6**(9): p. 996-998.

287. Rabaâ, H. and R. Hoffmann, *Electronic and Structural Effects of Nitrogen Doping on the Ionic Conductivity of γ-Li 3 PO 4.* Journal of Solid State Chemistry, 1999. **145**(2): p. 619-628.

288. Nimisha, C., et al., *Sputter deposited LiPON thin films from powder target as electrolyte for thin film battery applications.* Thin Solid Films, 2011. **519**(10): p. 3401-3406.

289. Hamon, Y., et al., *Influence of sputtering conditions on ionic conductivity of LiPON thin films.* Solid state ionics, 2006. **177**(3): p. 257-261.

290. Zhao, S., Z. Fu, and Q. Qin, *A solid-state electrolyte lithium phosphorus oxynitride film prepared by pulsed laser deposition.* Thin Solid Films, 2002. **415**(1): p. 108-113.

291. Iriyama, Y., et al., *Reduction of charge transfer resistance at the lithium phosphorus oxynitride/lithium cobalt oxide interface by thermal treatment.* Journal of Power Sources, 2005. **146**(1): p. 745-748.

292. Reimers, J.N. and J. Dahn, *Electrochemical and in situ X-ray diffraction studies of lithium intercalation in Li x CoO2.* Journal of The Electrochemical Society, 1992. **139**(8): p. 2091-2097.

293. Levi, E., et al., *Electrochemical and in-situ XRD characterization of LiNiO 2 and LiCo 0.2 Ni 0.8 O 2 electrodes for rechargeable lithium cells.* Solid state ionics, 1999. **126**(1): p. 97-108.

294. Kozen, A.C., et al., *Atomic layer deposition of the solid electrolyte LiPON.* Chemistry of Materials, 2015. **27**(15): p. 5324-5331.

295. Chong, J., et al., *Li3PO4-Coated LiNi0. 5Mn1. 5O4: A stable high-voltage cathode material for lithium-ion batteries.* Chemistry-A European Journal, 2014. **20**(24): p. 7479-7485.

296. Chung, K.-i., et al., *Suppressive effect of lithium phosphorous oxynitride at carbon anode on solvent decomposition in liquid electrolyte.* Journal of Power Sources, 2002. **112**(2): p. 626-633.

297. Santosh, K., et al., *Electrode-electrolyte interface for solid state Li-ion batteries: point defects and mechanical strain.* Journal of The Electrochemical Society, 2014. **161**(11): p. F3104-F3110.

298. Choi, C., et al., *Radio-frequency magnetron sputtering power effect on the ionic conductivities of LiPON films.* Electrochemical and Solid-State Letters, 2002. **5**(1): p. A14-A17.

299. Birke, P. and W. Weppner, *Change of the oxidation state of phosphorus in sputtered Li3±xPO4±y and Li3±xPO4±yNz films.* Ionics, 1996. **2**(1): p. 75-79.

300. Jacke, S., et al., *Investigation of the solid-state electrolyte/cathode LiPON/LiCoO2 interface by photoelectron spectroscopy.* Ionics, 2010. **16**(9): p. 769-775.

301. Ramar, V. and P. Balaya, *Enhancing the electrochemical kinetics of high voltage olivine LiMnPO 4 by isovalent co-doping.* Physical Chemistry Chemical Physics, 2013. **15**(40): p. 17240-17249.

302. Yuan, L.F., et al. *Synthesis and electrochemical properties of Cu-doped LiMnPO4/C nanorods as cathode materials of lithium-ion batteries*. in *Journal of Nano Research*. 2013. Trans Tech Publ.

303. Gu, Y., et al., *Synthesis of 3D-hiearchical LiMPO 4 (M= Fe, Mn) microstructures as cathode materials for lithium-ion batteries.* CrystEngComm, 2013. **15**(24): p. 4865-4870.

304. Ferrari, S., et al., *Latest advances in the manufacturing of 3D rechargeable lithium microbatteries.* Journal of Power Sources, 2015. **286**: p. 25-46.

305. Vereecken, P., *Towards all solid-state 3D thin-film batteries for durable and fast storage.* Solid State Technology, 2014. **57**(3): p. 28-30.